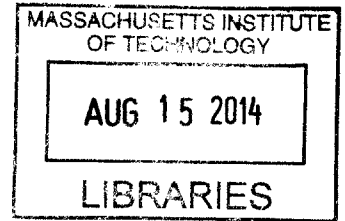


Computations and Modeling of Oil Transport between Piston Lands and Liner in Internal Combustion Engines

by

Tianshi Fang

Bachelor of Engineering in Mechanical Engineering
The University of Hong Kong, 2012



ARCHIVES

SUBMITTED TO THE DEPARTMENT OF MECHANICAL ENGINEERING IN
PARTIAL FULFILLMENT OF THE REQUIREMENTS FOR THE DEGREE OF

MASTER OF SCIENCE IN MECHANICAL ENGINEERING
AT THE
MASSACHUSETTS INSTITUTE OF TECHNOLOGY

June, 2014

© 2014 Massachusetts Institute of Technology. All rights reserved.

Signature redacted

Signature of Author: _____
Department of Mechanical Engineering

May 9, 2014

Certified by: _____
Signature redacted

Dr. Tian Tian

Principal Research Engineer, Department of Mechanical Engineering

Signature redacted Thesis Supervisor

Accepted by: _____
David E. Hardt

Professor of Mechanical Engineering
Chairman, Committee on Graduate Students

Computations and Modeling of Oil Transport between Piston Lands and Liner in Internal Combustion Engines

By

Tianshi Fang

Submitted to the Department of Mechanical Engineering
on May 9, 2014 in partial fulfillment of the requirements for the Degree of
Master of Science in Mechanical Engineering

Abstract

The consumption of lubricating oil in internal combustion engines is a continuous interest for engine developers and remains to be one of the least understood areas. A better understanding on oil transport is critical to an optimization of engine designs, and advanced analytical tools are essential to the achievement of reduced frictions without compromising oil consumption.

Oil transport from piston lands to a liner, hereafter called “bridging”, has been observed in engine tests. The additional oil transferred to the liner becomes a potential source of oil consumption through ring-liner interaction. Thus, it is important to develop more quantitative models to better analyze bridging. The objective of this work is to obtain a more in-depth understanding on the oil transport between piston lands and liner and provide quantitative models of the oil transport mechanisms. Multiphase Computational Fluid Dynamics (CFD) was employed together with analyses of experimental observations.

Three categories of bridging were identified: assisted bridging, self-sustained bridging, and reverse bridging. While assisted bridging involves an axial oil flow across an entire piston land, the other two phenomena are localized and become prominent at low engine speeds. The mechanisms of each phenomenon were analyzed in this work. Correlations and theoretical models were developed to associate the risk of bridging with geometrical designs of a piston and operating conditions of an engine. Particularly, the theoretical model of self-sustained bridging contributes to the optimization of geometrical designs of the third land of a piston ring pack.

This work constitutes a major step towards a further quantification of oil transport. Some findings and models presented in this work can readily contribute to providing optimal solutions to certain piston regions. Furthermore, the results of this work serve broader purposes in providing boundary conditions to other interactions in a piston ring pack.

Thesis Supervisor: Dr. Tian Tian
Title: Principal Research Engineer

Acknowledgements

The research area of oil transport and lubrication in automotive engines was introduced to me by my advisor, Dr. Tian Tian, without whom this work would by no means be possible. I consistently benefit from the discussions with him in the last two years. I highly appreciate his insightful suggestions all through this work and his valuable comments on a first manuscript of this report.

This work is sponsored by the consortium on lubrication in internal combustion engines with additional support by Argonne National Laboratory and the US Department of Energy. The current consortium members are Daimler, Mahle, PSA Peugeot Citroën, Renault, Shell, Toyota, Volkswagen, Volvo Cars, and Volvo Truck. I appreciate the useful feedbacks and constructive suggestions from their representatives.

I am grateful to my laboratory mates for their kind help and friendship. They are (in alphabetical order of surname): Camille Baelden, Kai Liao, Yang Liu, Mathieu Picard, Pasquale Pio Totaro, Zachary Westerfield, Eric Zanghi, and Qing Zhao. Special gratitude goes to Eric, whose experimental study provided supportive reference for my work. I appreciate my senior office mates Kai, Camille, Mathieu, and Yang for their generous help and useful discussions.

I would like to express my special gratitude to Yuan Wang, who worked in the consortium before I came to MIT. It was from him that I took over the modified multiphase OpenFOAM solver, interFoamPiston. It is the primary computational tool that I employed all through this work.

I appreciate all my friends at MIT for their help through my two years' stay, both academic and non-academic. I treasure the enjoyable times with them. And I value the friendship.

My sincere gratitude goes to my parents, who consistently offered unconditional supports through video chats from the other side of the earth.

Table of Contents

Abstract	3
Acknowledgements.....	5
Table of Contents.....	7
List of Figures.....	11
List of Tables.....	15
1 Introduction	17
1.1 The Piston Assembly	17
1.2 One Mechanism of Oil Transport from Piston Land to Liner: Bridging	20
1.3 Scope of This Work	24
1.3.1 Background	24
1.3.2 Motivation	24
1.3.3 Computational Simulations	24
1.3.4 Experiments.....	25
1.3.5 Structure of This Report.....	26
2 Bridging Caused by Axial Oil Flow on Piston Land	27
2.1 Introduction	27
2.1.1 Critical Quantity of Oil for TDC Bridging.....	27
2.1.2 Existing Study	27
2.1.3 Objectives.....	28
2.1.4 Structure of This Chapter	28
2.2 Simulation Setup	28
2.2.1 Variables to be Studied	28
2.2.2 Initial Settings of Simulations	29
2.3 Observations in Simulations	30
2.3.1 At a Low Engine Speed	30
2.3.2 At a High Engine Speed.....	33
2.3.3 Closure	35
2.4 Theoretical Analyses on a Few Sub-Processes	35
2.4.1 Early Rise Resulting from Surface Tension	35
2.4.2 Circular Residual Oil	37
2.4.3 Oil Junction between Piston Land and Lower Ring Flank	40
2.4.4 Axial Flow along Piston Land	43

2.5	Critical Oil Quantity	51
2.5.1	Critical Oil Quantity Based on Simulations	51
2.5.2	Discussions	54
2.6	Summary	55
3	Oil Trapping in Second Ring Hook and Self-Sustained Bridging	57
3.1	Introduction	57
3.1.1	Motivation	57
3.1.2	Observations in Experiments	57
3.1.3	Observations in Simulations	58
3.1.4	Bridging Mechanisms	61
3.1.5	Structure of This Chapter	63
3.2	Oil Trapping in Second Ring Hook	63
3.2.1	Physics behind Oil Trapping	63
3.2.2	A Theoretical Definition of Oil Trapping	65
3.2.3	A Heuristic Analysis	66
3.2.4	A Theoretical Model of Oil Trapping	71
3.2.5	More Potential Approaches to Decrease Critical Trapping Speed	84
3.2.6	Closure	86
3.3	Self-Sustained (SS) Bridging	86
3.3.1	Modeling Method	87
3.3.2	Results and Discussions	93
3.3.3	Sensitivity Analysis	96
3.3.4	Strategies for Elimination of SS Bridging	98
3.4	Comments on the Theoretical Models	99
3.4.1	Limitations of the Theoretical Models	99
3.4.2	Comparison with Experiments and Simulations	101
3.5	Summary	102
4	Reverse Bridging	105
4.1	Introduction	105
4.1.1	The Concept of Reverse Bridging	105
4.1.2	Observations in Experiments	105
4.1.3	Observations in Simulations	106
4.1.4	Fraction of Reverse Bridging	108
4.1.5	Structure of This Chapter	109

4.2	Simulation Setup	109
4.2.1	Sources of Scraped Oil.....	109
4.2.2	Computational Domain	110
4.2.3	Variables to be Studied	111
4.3	Simulation Results.....	111
4.3.1	An Example: Uniform Scraping by Non-Tapered OCR at 800rpm	112
4.3.2	Uniform Scraping by Non-Tapered OCR.....	116
4.3.3	Scraping of Bridging Oil by Non-Tapered OCR.....	119
4.3.4	Uniform Scraping by Tapered OCR	121
4.3.5	Scraping of Bridging Oil by Tapered OCR.....	125
4.4	Alternative Traces of Scraped Oil	127
4.4.1	Uniform Scraping: Viscous Dissipation in Corner	128
4.4.2	TDC Scraping: Viscous Dissipation on OCR Flank.....	128
4.4.3	Profile of Oil-Gas Interface	129
4.5	Summary	130
5	Conclusion.....	131
	Appendix	133
	Appendix 1: Numerical Scheme for Equation (2.49)	133
	References	135

List of Figures

Figure 1.1	Piston and rings (Left: piston; right: rings)	18
Figure 1.2	Schematic diagram of radial cross section of piston-ring pack (Not to scale).....	18
Figure 1.3	Schematic diagram of oil transport towards combustion chamber (Grey curves illustrate oil paths)	19
Figure 1.4	Variation of normalized body force field ($l = 158\text{mm}$; $r = 44\text{mm}$) ..	20
Figure 1.5	Schematic diagram of bridging mechanisms in radial cross section	21
Figure 1.6	Detriment of TDC bridging (Not to scale)	22
Figure 1.7	Schematic diagram of velocity profile in oil film on piston land	23
Figure 1.8	2D LIF experiment demonstrating oil distribution from piston skirt towards crown land. Brighter color indicates more oil (Courtesy of E. Senzor[8])	23
Figure 1.9	Directions of vision in simulations and experiments	25
Figure 2.1	Critical oil volume for bridging [6, p. 79].....	27
Figure 2.2	Geometry of computational domain.....	28
Figure 2.3	Initialization of simulation. Red color denotes oil and blue color denotes gas.....	30
Figure 2.4	Oil distribution with streamlines (left) and velocity field (right) before body force switches to upward direction, 800rpm	31
Figure 2.5	Complete evolution of TDC bridging, 800rpm	32
Figure 2.6	Pressure field, 800rpm (Gas pressure is almost uniform. It is set to be 100000Pa.).....	32
Figure 2.7	Streamlines (left) and velocity field (right) before body force switches to upward direction, 4500rpm.....	33
Figure 2.8	Complete evolution of TDC bridging, 4500rpm	34
Figure 2.9	Pressure field, 4500rpm (Gas pressure is almost uniform. It is set to be 100000Pa.)	35
Figure 2.10	Schematic diagram of oil-gas interface under variant body acceleration.	36
Figure 2.11	Schematic diagram of circular residual oil	37
Figure 2.12	Interface profile of circular residual oil, normalized by y_c	39
Figure 2.13	Height of circular residual oil along piston land ($\sigma = 0.02\text{N/n}$, $\rho = 800\text{kg/m}^3$, $r = 44\text{mm}$, $l = 158\text{mm}$).....	39
Figure 2.14	Schematic diagram of rounded oil junction.....	40
Figure 2.15	Interface profile of rounded oil junction, normalized by y_c	42
Figure 2.16	Span of rounded oil junction along lower second ring flank ($\sigma = 0.02\text{N/n}$, $\rho = 800\text{kg/m}^3$, $r = 44\text{mm}$, $l = 158\text{mm}$)	42
Figure 2.17	Division of oil along piston third land during oil rises	43
Figure 2.18	Schematic diagram of the model for region 2 (Not to scale).....	44
Figure 2.19	Schematic diagram of the model for region 1 (Not to scale).....	46
Figure 2.20	Schematic diagram of the model for region 3 (Not to scale).....	47
Figure 2.21	Results of oil rising model (Left: 800rpm; right: 4500rpm).....	50
Figure 2.22	Volume ratio of puddle tail (Left: 800rpm; right: 4500rpm).....	50
Figure 2.23	Critical oil quantity against engine speed. $d = 0.5\text{mm}$, with different v . (Left: normal scale; right: logarithmic scale).....	52

Figure 2.24	Critical oil quantity against engine speed. $v = 3.125 \times 10^{-6} \text{m}^2/\text{s}$, with different d . (Left: normal scale; right: logarithmic scale)	52
Figure 2.25	Critical oil quantity against oil viscosity. $d = 0.5 \text{mm}$, with different N . (Left: normal scale; right: logarithmic scale)	53
Figure 2.26	Critical oil quantity against clearance. $v = 3.125 \times 10^{-6} \text{m}^2/\text{s}$, with different N . (Left: normal scale; right: logarithmic scale)	54
Figure 2.27	TDC bridging with a second ring hook and a chamfer on top of piston third land	55
Figure 3.1	Bridging and oil trapping in second ring hook observed in experiment at 800rpm, 400mbar intake pressure. (Courtesy of E. Zanghi)	58
Figure 3.2	Computational domains for OpenFOAM simulations	59
Figure 3.3	Oil trapping in a rectangular hook with a piston chamfer (Red: oil; blue: gas)	59
Figure 3.4	Bridging in a rectangular hook with a piston chamfer (Red: oil; blue: gas)	60
Figure 3.5	Oil distribution in a rectangular hook without a piston chamfer (Red: oil; blue: gas)	61
Figure 3.6	Oil supply from piston third land to second ring hook (Red: oil; blue: gas)	62
Figure 3.7	Schematic diagram of TDC bridging with a second ring chamfer	63
Figure 3.8	Pressure fields in trapped oil. (Pressure in Pa. Gas pressure is 100000Pa.)	64
Figure 3.9	“Pinning” of oil contact line at the outer edge of piston chamfer	64
Figure 3.10	Schematic diagram of oil trapped in second ring hook (Left: low speed; Right: high speed)	65
Figure 3.11	Coordinate system and geometric parameters in the heuristic analysis (Not to scale)	66
Figure 3.12	Evolution of interface profile at the critical point	68
Figure 3.13	Geometry of tapered Napier ring hook (Left: positive angle; right: negative angle)	69
Figure 3.14	Oil-gas interface profiles in Napier ring hooks at different engine speeds (Left: $+15^\circ$ tapered angle; right: -10° tapered angle; legend: engine speed in rpm)	70
Figure 3.15	Conformation of piston chamfer to second ring hook	71
Figure 3.16	Pinning of oil contact line if piston chamfer is larger than second ring hook	71
Figure 3.17	Geometric parameters in the model for trapping	72
Figure 3.18	Boundary condition on top of interface	73
Figure 3.19	B as a function of ξ . ($\gamma = 15^\circ$, $\psi = 0^\circ$)	75
Figure 3.20	B_{\max} as a function of γ . ($\psi = 0^\circ$)	75
Figure 3.21	B_{\max} as a function of γ . ($\alpha = 90^\circ$)	76
Figure 3.22	Geometric indication of D and d_{eq}	76
Figure 3.23	Critical k value against tapered hook angle γ . (left: $w = 1 \text{mm}$, $c = 0.5 \text{mm}$, $d = 0.6887 \text{mm}$, see Figure 3.2 (a); right: $w = 1 \text{mm}$, $c = 0.5 \text{mm}$, $d = 0.4 \text{mm}$, see Figure 3.2 (b))	80

Figure 3.24	Critical speed against height of hook region d . ($w = 1\text{mm}$, $c = 0.5\text{mm}$, $\gamma = 10^\circ$).....	80
Figure 3.25	Critical engine speed for oil trapping in typical designs	81
Figure 3.26	A larger cut on top of piston third land	84
Figure 3.27	Double cuts on top of piston third land	85
Figure 3.28	Effect of rounded edge. (Left: contact line pinned at a sharp edge; right: contact line moves smoothly through a rounded edge.).....	85
Figure 3.29	Oil passage in the vicinity of outer edge of piston chamfer	86
Figure 3.30	Geometric parameters in the model for SS bridging.....	87
Figure 3.31	Breaking-up of oil-gas interface (Left: at the moment of breaking-up; right: separation at TDC).....	92
Figure 3.32	Oil-gas interface at TDC after it breaks-up	93
Figure 3.33	Modeling results for Design 1 ($R = 0.2\text{mm}$, $d = 0.69\text{mm}$, $w = 1\text{mm}$, $c = 0.5\text{mm}$, $s = 0.29\text{mm}$, $\theta = 30^\circ$) (Left: modeling by distance; right: modeling by volume).....	94
Figure 3.34	Ranges of engine speed in which a risk of SS bridging exists (Light colour: model by distance; dark colour: model by volume).....	95
Figure 3.35	Oil trapping and self-sustained bridging modeled by volume (light colour: trapping without self-sustained bridging; dark colour: trapping and self-sustained bridging)	95
Figure 3.36	Sensitivity of oil volume that is needed for SS bridging to advancing contact angle ϕ	96
Figure 3.37	Sensitivity of oil volume that is needed for SS bridging to receding contact angle χ	97
Figure 3.38	Sensitivity of critical speed to advancing contact angle ϕ ($\gamma = 15^\circ$).....	97
Figure 3.39	Oil trapping and SS bridging in a transient condition.....	98
Figure 3.40	Circumferential distribution of oil in second ring hook and piston chamfer	101
Figure 3.41	Dimensions of the test engine.....	101
Figure 4.1	Reverse bridging observed in experiments at 1500rpm, 600mbar intake pressure. (Courtesy of E. Zanghi).....	106
Figure 4.2	Reverse bridging in simulation, 800rpm, 0.4mm piston-liner clearance, 80 μm initial film.....	107
Figure 4.3	Reverse bridging in simulation, 4500rpm, 0.5mm piston-liner clearance, 30 μm initial film.....	107
Figure 4.4	Alternative traces of oil scraped by upper OCR flank	108
Figure 4.5	Computational domain of simulations of reverse bridging	110
Figure 4.6	Tapered angle ϕ of upper OCR flank (Not to scale).....	111
Figure 4.7	Uniform scraping and reverse bridging, non-tapered OCR, 800rpm, $V_{\text{scraped}} \approx 1500 \mu\text{m}^2$	112
Figure 4.8	Cusp in oil-gas interface near the corner bounded by upper OCR flank and liner	114
Figure 4.9	Effect of cusp (Grey: oil without cusp; dashed black curve: oil surface with cusp).....	114
Figure 4.10	Force balance on the control volume below cusp.....	114

Figure 4.11	Two regions of oil as oil accumulates	115
Figure 4.12	Uniform scraping and reverse bridging, non-tapered OCR, 4500rpm, $V_{\text{scraped}} \approx 1500 \mu\text{m}^2$	117
Figure 4.13	Fraction of reverse bridging γ against quantity of scraped oil, uniform scraping, non-tapered OCR flank	118
Figure 4.14	Fraction of reverse bridging γ against engine speed N, uniform scraping, non-tapered OCR flank.....	119
Figure 4.15	TDC scraping and reverse bridging, non-tapered OCR, 800rpm, $V_{\text{scraped}} \approx 1500 \mu\text{m}^2$	119
Figure 4.16	scraping and reverse bridging, non-tapered OCR, 4500rpm, V_{scraped} $\approx 1500 \mu\text{m}^2$	120
Figure 4.17	Fraction of reverse bridging γ against engine speed N, TDC scraping, non-tapered OCR flank.....	121
Figure 4.18	Components of body force. (a): downward body force; (b) upward body force	121
Figure 4.19	Uniform scraping and reverse bridging, 18° tapered OCR, 800rpm, $V_{\text{scraped}} \approx 1500 \mu\text{m}^2$	122
Figure 4.20	Uniform scraping and reverse bridging, 18° tapered OCR, 4500rpm, $V_{\text{scraped}} \approx 1500 \mu\text{m}^2$	124
Figure 4.21	Fraction of reverse bridging γ against engine speed N, uniform scraping, 18° tapered OCR flank	125
Figure 4.22	TDC scraping and reverse bridging, 18° tapered OCR, 800rpm, $V_{\text{scraped}} \approx 1500 \mu\text{m}^2$	126
Figure 4.23	TDC scraping and reverse bridging, 18° tapered OCR, 4500rpm, $V_{\text{scraped}} \approx 1500 \mu\text{m}^2$	126
Figure 4.24	Fraction of reverse bridging γ against engine speed N, TDC scraping, 18° tapered OCR flank	127
Figure 4.25	Possible flow patterns of scraped oil.....	127
Figure A.1	Figure of $I_2(\eta)$. (a): schematic diagram; (b) & (c): examples of computed results.....	134

List of Tables

Table 2.1	Index of power law between critical oil quantity and engine speed ..	52
Table 2.2	Index of power law between critical oil quantity and engine speed ..	53
Table 2.3	Index of power law between critical oil quantity and oil viscosity....	53
Table 3.1	Comparison of modeling results ($\varphi = 30^\circ$) with experiments and simulations.....	102

1 Introduction

Vehicle is one major contributor to the global energy consumption in modern society. In the past two decades, energy consumed by vehicles has been substantially increasing. The huge and increasing demand of energy necessitate comprehensive studies on the energy conversion system in vehicles – internal combustion engine. Any increase in the efficiency of automotive internal combustion engines will result in a considerable decrease in global fuel consumption, which in turn improves automotive economy, contributes to sustainable development, and reduces greenhouse gas (CO₂) emission.[1]

Among all types of internal combustion engines, piston engine is most widely applied in automobiles. Among the total energy consumed in automotive engines, roughly 15% is employed to overcome friction in piston assembly.[1] Thus, a decreased friction in piston assembly will considerably increase engine efficiency, and hence significantly reduce the global energy consumption. As a common practice to decrease friction, lubricating oil is supplied to piston assemblies. A systematical understanding of lubrication in piston assemblies is crucial to the achievement of a decreased friction.

1.1 The Piston Assembly

In a typical piston engine, fuel combusts in a cylindrical combustion chamber, which is mostly bounded by a cylinder head, a liner and a piston. While the first two are usually fixed in position in a vehicle except for vibrations and distortions, the piston reciprocates. The combustion of fuel in the combustion chamber results in an increase in pressure, which pushes the piston and exports mechanical energy. The crank shaft connected to pistons eventually converts reciprocating motion into rotational motion.

To maintain the proper functioning of a piston engine, the combustion chamber must be properly sealed to prevent gas leakage. It requires that the diameter of the piston should be roughly the same with the bore, which is the inner diameter of combustion chamber, cylinder, or liner. On the other hand, a tight contact between piston and liner will result in a considerable friction, which remarkably decreases engine efficiency.

The common practice to resolve this dilemma is described as follows. The diameter of piston is slightly smaller than the bore, leaving a clearance of roughly 200 μ m to 600 μ m between the piston and the liner. A few, typically three, circumferential grooves are cut on the piston surface, as demonstrated in Figure 1.1 left. In engine operations, three rings (Figure 1.1 right) are inserted in the grooves, one for each. The rings are in closer contact with the liner so that the combustion chamber can be better sealed despite the relatively large clearance between the piston and the liner. A schematic diagram of a radial cross section of a piston-ring pack is illustrated in Figure 1.2. The ring grooves divide the surface of piston into four parts. From combustion chamber (top in Figure 1.2) to crankcase (bottom in Figure 1.2), they are named crown land, second land, third land, and piston skirt. The three rings are usually named first ring (compression ring), second ring, and oil control ring (OCR).

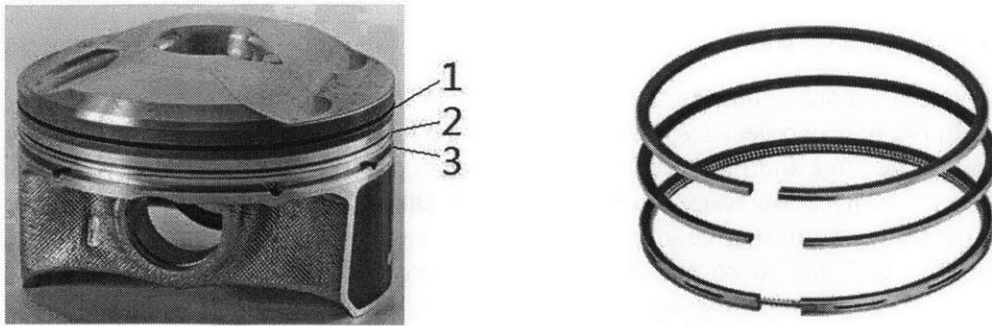


Figure 1.1¹ Piston and rings (Left: piston; right: rings)

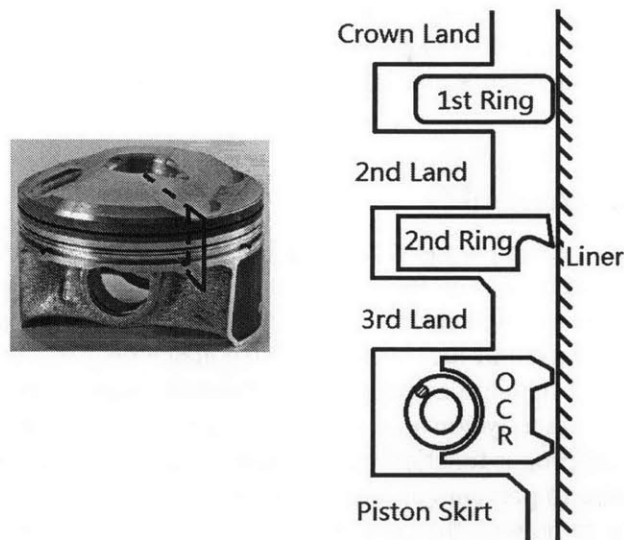


Figure 1.2 Schematic diagram of radial cross section of piston-ring pack (Not to scale)

For the purpose of mere lubrication, lubricating oil is expected on every rubbing surface in a piston-ring pack. A thin oil film is expected on the liner in order to lubricate the contacting surfaces of rings and liner. Lubricating oil may also be expected in the clearance between a ring flank and its groove because there will also be relative motions there. A desirable lubrication effectively reduces friction and enhances engine efficiency. It also alleviates wear on engine components and elongates life time of an engine.

On the other hand, the amount of oil that enters the combustion chamber must be strictly controlled. When lubricating oil enters the combustion chamber, it may be consumed by way of evaporation, carbonization, or combustion. The consumption of lubricating oil lessens engine economy and customer satisfaction. Moreover, some chemical elements in lubricating oils, for instance, phosphorous and sulfur, can poison

¹ Sources of pictures: left: <http://www.cleanmpg.com/forums/printthread.php?t=41627>
right: http://www.jitiigroup.com/detail_16.html

the catalysts in after treatment devices [1], which leads to undesirable emission of pollutants. Thus, one primary challenge in the design of piston-ring systems is the compromise between reduction of friction and suppression of oil consumption. The ultimate goal is to supply exactly irredundant amount of oil to each site, so that friction is satisfactorily reduced while oil consumption is minimized. To achieve this goal, an in-depth understanding of oil transport in every part of the piston-ring pack is necessary.

In a typical piston engine, lubricating oil is supplied from below the piston skirt, usually by splashing from the connecting rod. The oil supply is extremely redundant compared to that needed by a first ring. Thus, besides the sealing of combustion chamber, the rings also function to control oil leakage to the combustion chamber. Conventionally, it is deemed that a first ring primarily seals the combustion chamber, an OCR mostly controls oil supply to the upper piston-ring pack, and a second ring plays an auxiliary role in oil control.

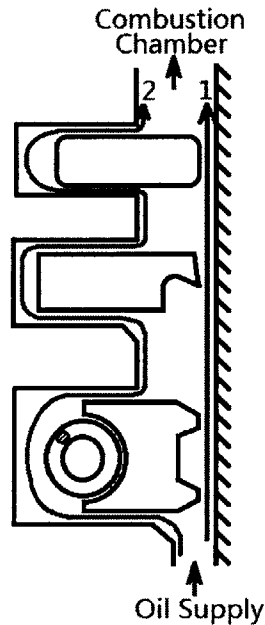


Figure 1.3 Schematic diagram of oil transport towards combustion chamber (Grey curves illustrate oil paths)

A thorough study on oil transport in a piston-ring pack has been conducted by Thirourd & Tian [2, 3]. They systematically identified oil transport mechanisms in different parts of the piston-ring pack. To briefly summarize their model, oil supplied from below the piston skirt leaks to the combustion chamber through two major paths: 1) through the clearances between rings and liner; 2) through clearances between ring flanks and grooves, behind grooves, and along piston lands. The two paths are illustrated in Figure 1.3. Sometimes oil can interchange between these two paths. One of such mechanisms is termed “bridging”, which will be explained in detail in the next section.

1.2 One Mechanism of Oil Transport from Piston Land to Liner: Bridging

In certain cases, oil on a piston land can spread along a ring flank and reach the liner. This process is termed “bridging”. The phrasing comes from the fact oil film on the liner connects, or bridges, to the oil on a piston land. A practical consequence of bridging is that additional oil is supplied to the liner, which contributes to friction reduction but possibly increases oil consumption. [4], [5]

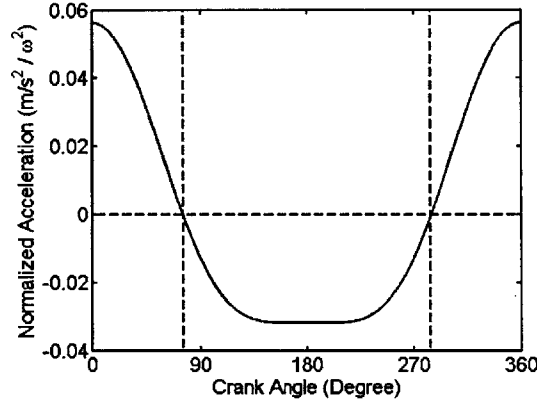


Figure 1.4 Variation of normalized body force field ($l = 158\text{mm}$; $r = 44\text{mm}$)

A typical scenario in which bridging occurs is described as follows. The description here is focused on the space bounded by a piston third land, the lower flank of a second ring, a liner and the upper flank of an OCR. If the piston is taken as the reference frame, there is a body force field associated with the acceleration of the piston. This body force field, or body acceleration, can be calculated with:

$$a = \omega^2 \cdot \left(r \cos \theta + \frac{r^2 \cos(2\theta)}{\sqrt{l^2 - r^2 \sin^2 \theta}} + \frac{r^4 \sin^2 \theta \cos^2 \theta}{(\sqrt{l^2 - r^2 \sin^2 \theta})^3} \right) \quad (1.1)$$

where a is body acceleration, ω is engine speed in radians per second, r is crank radius, l is connecting rod length, and θ is crank angle with 0° at top dead center (TDC) and 180° at bottom dead center (BDC). The positive direction is upwards, or towards the combustion chamber. A typical example of body acceleration normalized by ω^2 is plotted in Figure 1.4. At roughly 285° , most oil is accumulated at the bottom of the space near the upper flank of OCR because body force was downward before this moment. Then, the body force switches direction and oil will flow upwards along the piston third land. If the oil flows sufficiently fast to reach the lower flank of the second ring, and if the oil has sufficient time to spread along the lower second ring flank and reach the liner before TDC, then, oil will attach to and move with the downward moving liner. In this case, oil on the piston land connects to the liner, and bridging occurs. Such a bridging process has been reported in [4, 6]. An illustration of this mechanism is shown in Figure 1.5 (a).

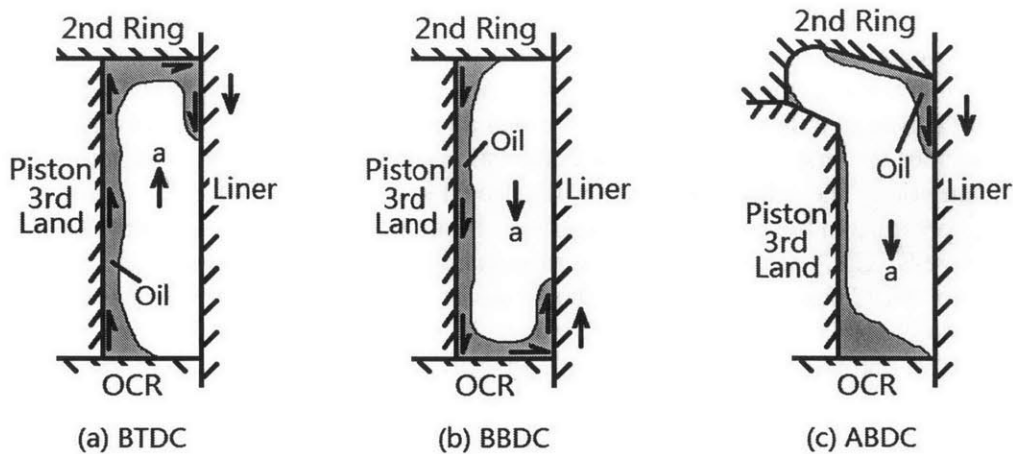


Figure 1.5 Schematic diagram of bridging mechanisms in radial cross section

Similar to BTDC bridging described in the last paragraph, bridging can also occur on the upper flank of the OCR before BDC. The only difference is that the oil flow and the body force driving it are in the opposite direction. BBDC bridging has been reported in [4]. An illustration of this mechanism is presented in Figure 1.5 (b).

As reported in [2, 7], bridging can also occur after BDC. As illustrated in Figure 1.5 (c), there is usually a tapered hook on the lower outer edge of a second ring. One reason behind such a design will be explained shortly. At BDC, although the body force is downward, some oil can still stay in the hook of the second ring, which will be explained in Chapter 3. Under the downward body force, a slight amount of oil can flow down along the upper surface of second ring hook and approach the liner. When an upstroke starts, this part of oil will attach to the liner, which is moving downward in this reference frame. This bridging mechanism is illustrated in Figure 1.5 (c).

While the first and the second scenarios are complementary, the complement of the third mechanism has not been found in literature. It is because there is no hook in an OCR. However, a phenomenon which appears similar to “ATDC bridging” has been discovered and will be described in Chapter 4.

Occurrence of bridging means that OCR partially loses control of oil film thickness on the liner, which is an undesirable situation in engine operations. Thus, bridging is an undesirable phenomenon to the reduction of oil consumption. As explained by Przesmitzki et al. [4], TDC bridging increases oil consumption, while BDC does not. This is explained as follows. Because of bore distortion, at the beginning of an intake stroke, the clearance between the second ring and the liner can be relatively large at some sites. If bridging occurs before TDC, the oil film on the liner is thickened as illustrated in Figure 1.6 (a). When the liner reverses direction after TDC, the additional oil on the liner can leak through the large clearance instead of being scraped by the second ring. It may even leak through the clearance between the first ring and the liner. The oil leakage is illustrated in Figure 1.6 (b). Then, the liner will come back to the TDC at the end of the successive compression stroke. Because of the combustion happening in combustion chamber, the gas pressure in it is high at this time. The high pressure can push the first ring downward, leaving a clearance between its upper flank and its groove. Thus, the

space behind the first ring is connected with the combustion chamber, and the pressure there is increased. The high pressure behind the first ring will push it towards the liner, resulting in a better conformation between the first ring and the distorted liner. Thus, only a little oil can escape through the ring-liner clearance. Much oil will be scraped by the upper flank of the first ring towards the combustion chamber, eventually contributing to oil consumption. The upward scraping is illustrated in Figure 1.6 (c). On the other hand, since the pressure in the combustion chamber will not be significantly different at two consecutive BDC's, there will not be a significant difference in ring-liner conformation. Resultantly, BDC bridging will less probably result in upward scraping towards the combustion chamber. Thus, TDC bridging is deemed more detrimental in terms of oil consumption, and the study of TDC bridging is therefore of more practical interest.

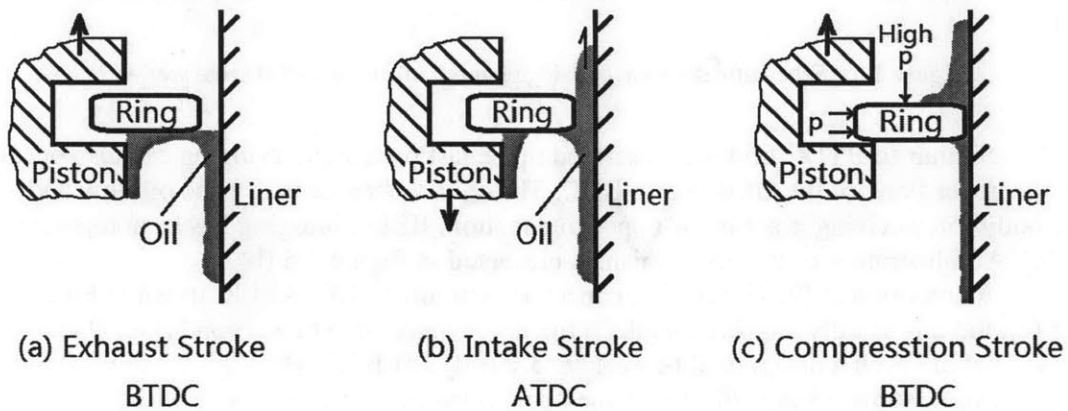


Figure 1.6 Detriment of TDC bridging (Not to scale)

As a common practice to avoid TDC bridging, a tapered hook is usually cut in the lower outer edge of a second ring. This type of rings is named "Napier rings". It is usually utilized in conjunction with a chamfer on the top of a third land. The hook, together with the chamfer, provides a buffer for oil when it reaches the top of piston third land under upward body force. It is expected that oil will reside in this hook instead of bridging to the liner or leaking through the second ring groove.

Bridging occurs only if oil flows sufficiently fast along a piston land. A detailed analysis on the oil flow will be presented in Section 2.4.4. Here, a final solution derived from lubrication theory is presented:

$$v = -\frac{a}{2\nu}(x^2 - 2hx) \quad (1.2)$$

where v is oil velocity along a piston land, a is body acceleration, ν is kinematic viscosity of oil, h is local oil thickness, and x is the coordinate perpendicular to the piston land. (See Figure 1.7.) Equation (1.2) indicates that oil flows faster if the oil layer on the piston land is thicker. When bridging occurs, oil on the piston land must flow sufficiently fast.

Thus, oil thickness on the piston land must be sufficiently large. In other words, oil supply to this space must be sufficient.

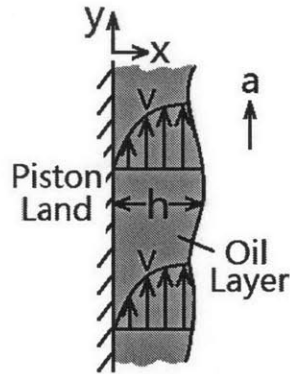


Figure 1.7 Schematic diagram of velocity profile in oil film on piston land

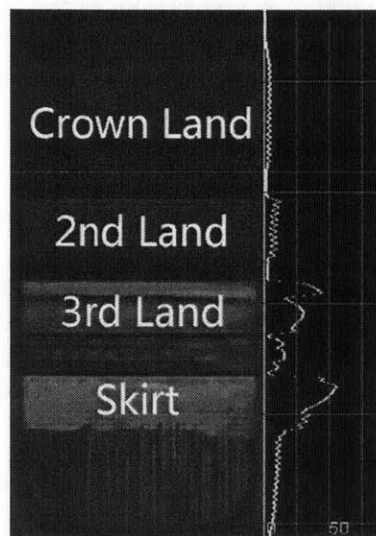


Figure 1.8 2D LIF experiment demonstrating oil distribution from piston skirt towards crown land. Brighter color indicates more oil (Courtesy of E. Senzor[8])

As demonstrated in Figure 1.8, the amount of oil decreases from piston skirt towards the crown land because of the oil control by each ring. Thus, TDC bridging is most probable in the vicinity of a piston skirt and a third land where oil supply is sufficient. It rarely occurs in the vicinity of a second land, though it has been reported in [9]. In the vicinity of piston skirt, oil supply is usually ample and it is almost impossible to avoid bridging in this region. However, since the spring behind OCR will result in a good ring-liner conformation, bridging below the OCR may not result in oil consumption. Thus, it is not that meaningful to suppress bridging in this region. Since there is no spring

behind a normal second ring, a study on TDC bridging in the vicinity of third land is of most practical interest.

1.3 Scope of This Work

1.3.1 Background

This work was originally motivated by a set of experiments conducted by Zanghi [10]. In the experiments, TDC bridging was observed at low engine speeds, which contradicted the existing theory [2], [4], [6] that is reviewed in Section 1.2. In order to figure out the reasons behind low speed bridging, computational simulations of oil flow near a piston third land were conducted.

In a preliminary examination of the simulation results, three mechanisms of oil transport from a piston land to a liner have been identified. Based on the natures of these mechanisms, the one that was described in Section 1.2 was named “assisted bridging”, and the two newly-discovered mechanisms were named “self-sustained bridging” and “reverse bridging”, respectively. The definition of “assisted bridging” and “self-sustained bridging” will be presented in Chapter 3, and that of “reverse bridging” in Chapter 4. The experiments conducted by Zanghi [10] indicated that the three mechanisms indeed occur in real engine operations.

1.3.2 Motivation

The primary objective of this work is to understand the three oil transport mechanisms in the vicinity of a piston third land, namely, the cavity bounded by a piston third land (including the chamfer on both ends), the lower flank (including the surface of a hook) of a second ring, a liner, and the upper flank of an OCR.

Since oil consumption at city driving speeds, for instance, from 600 to 1800 rpm, has been receiving increasing attention in the automotive industry, special attention will be paid to the oil transport at low engine speeds.

1.3.3 Computational Simulations

Computational simulations were conducted all through this work. They facilitated an observation of oil flow in a radial cross section as is shown in Figure 1.9. Because the focus of this work was oil flow in the axial direction driven by body force, all simulations were two-dimensional. Variations in the circumferential direction, including the effects of circumferential gas flow [2], [3] and instabilities on oil-gas interfaces, were beyond the focus of this work. Furthermore, the oil and gas leakage through the clearances between ring flanks and grooves and through the clearances between ring lands and a liner were neglected. That is, the cavity was assumed to be perfectly sealed. The dynamics of rings were also neglected. That is, the boundaries of the computational domains were stationary.

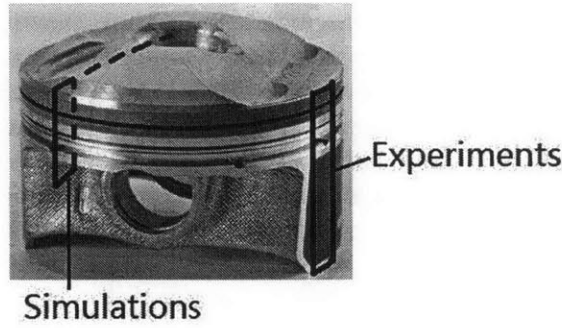


Figure 1.9² Directions of vision in simulations and experiments

The computational tool that is employed in this work was OpenFOAM, an open computational fluid dynamics (CFD) software. A standard multiphase solver, interFoam, was utilized in order to simulate both oil and gas flow in the cavity. The solver has been modified by Wang [6] to accommodate the time-variant body force field. It utilizes the volume of fraction (VOF) method to trace the interface of oil and gas. The governing equations in this solver are [6]:

$$\nabla \cdot \vec{U} = 0 \quad (1.3)$$

$$\frac{\partial(\rho\vec{U})}{\partial t} + \rho\vec{U} \cdot \nabla\vec{U} = -\nabla p_{\text{pah}} - (\vec{a} \cdot \vec{x})\nabla\rho + \nabla \cdot \vec{\tau} + \sigma\kappa\vec{n} \quad (1.4)$$

$$\frac{\partial\alpha}{\partial t} + \nabla \cdot (\alpha\vec{U}) = 0 \quad (1.5)$$

where \vec{U} is velocity vector, ρ is fluid density, t is time, p_{pah} is pressure minus hydrostatic pressure ($p_{\text{pah}} = p - \rho\vec{a} \cdot \vec{x}$), \vec{a} is body acceleration, \vec{x} is coordinate of a point, $\vec{\tau}$ is shear stress, σ is surface tension of oil and gas, κ is curvature of interface, \vec{n} is the normal vector of interface area, and α is fraction of oil in a computational cell. Equation (1.3) and Equation (1.4) are continuity equation and Navier-Stokes equation, which are the fundamental equations for all problems in fluid mechanics. The last term in Equation (1.4) addresses surface tension in a multiphase problem. Equation (1.5) is a unique equation for the VOF method. It calculates the fraction of oil (α) in a computational cell.

For simple rectangular computational domains, blockMesh, which is a simple meshing tool enclosed with OpenFOAM, was employed. For geometries containing fillets, tapered angles, ANSYS Meshing was employed.

1.3.4 Experiments

Results of 2D LIF experiments conducted by Zanghi [10] were taken as supportive verifications of the simulation results. Different from 2D simulations in a radial cross section, the experiments facilitated an observation of oil flow from outside

² Source of picture: <http://www.cleanmpg.com/forums/printthread.php?t=41627>

the piston. The difference in vision direction is illustrated in Figure 1.9. Details of the experimental set-up can be found in [7], [10].

Figure 1.8 is an example of pictures taken in experiments. Lubricating oil is mingled with fluorescent dye, and a laser source illuminates the oil. A camera is employed to receive the light reflected by the fluorescent dye. Regions with more oil are marked with a brighter color (white) in a picture, while regions with less oil are marked with a darker (black) color.

1.3.5 Structure of This Report

Chapter 1 is a brief introduction of this work. The concept of bridging has been introduced and the motivation of this work has been explained.

Chapter 2, 3, and 4 are the three major chapters of this report. Each chapter is focused on one mechanism of oil transport from a piston land to a liner. The physics behind oil transport processes will be explained based on simulation results, and theoretical analyses will be presented.

Chapter 2 will be focused on assisted bridging, of which the definition is presented later in Chapter 3. Simulations of oil re-distribution in the vicinity of a piston third land will be introduced, with a focus on TDC bridging caused by axial oil flow driven by body force. Some physics behind the complete process will be described and modeled.

In Chapter 3, self-sustained bridging will be introduced. It results from surface tension, and is more pronounced at low engine speeds. A quantitative model aiming at preventing this phenomenon by way of optimizing second ring design will be presented.

In Chapter 4, reverse bridging will be introduced. It appears similar to bridging and can be equally detrimental to TDC bridging. The physics behind reverse bridging will be explained based on simulations. It will be shown that this phenomenon is more detrimental at low engine speeds.

Chapter 5 will summarize this work. Future work will also be proposed in this chapter.

2 Bridging Caused by Axial Oil Flow on Piston Land

2.1 Introduction

2.1.1 Critical Quantity of Oil for TDC Bridging

As explained in Chapter 0, bridging occurs when axial oil flow on a piston third land is sufficiently fast. One essential condition of it is that sufficient oil exists in the vicinity of a piston third land. A critical quantity of oil can be expected at a certain engine speed. When the actual amount of oil in this cavity exceeds the critical value, bridging occurs. Otherwise, bridging will not occur. Given that circumferential variation is not to be considered in this work, the critical value in a two-dimensional simulation is measured by the cross sectional area of oil.

Equation (1.2) implies that oil velocity is proportional to body acceleration, which is proportional to the square of engine speed. On the other hand, the time interval allowed for axial oil flow is inverse proportional to engine speed. Oil velocity increases with engine speed at a more rapid rate than the time interval decreases. Thus, TDC bridging caused by axial oil flow on a piston land is more probable at a higher engine speed. It is expected that the critical volume decreases with engine speed.

2.1.2 Existing Study

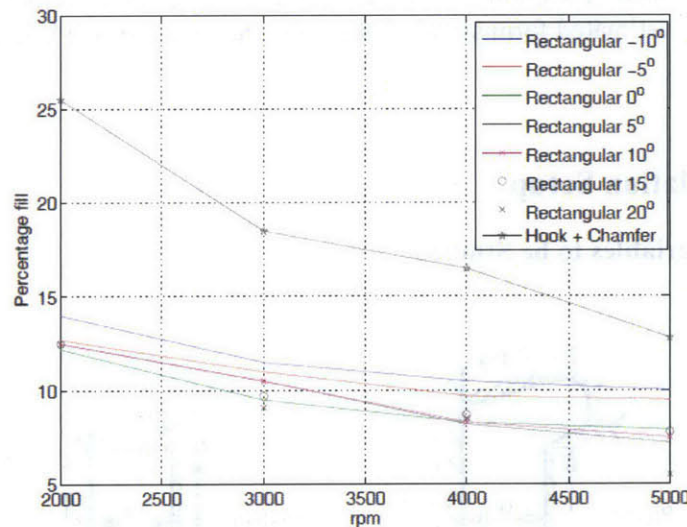


Figure 2.1 Critical oil volume for bridging [6, p. 79]

Wang [6] has conducted a numerical study on the correlation between the critical volume and engine speed. Two classes of designs were studied: 1) plain rectangular second rings with different twist angles; 2) a Napier ring together with a chamfer on top of piston third land. Figure 2.1 shows his results. The abscissa is engine speed in rpm, and the ordinate is the critical volume, measured by the percentage of space filled with oil.

As expected, the critical volume decreases with engine speed in all designs studied. The critical volume does not vary significantly with the twist angle of a plain second ring, while a hook together with a chamfer substantially increases the critical volume. It confirms the argument that a hook in a second ring can effectively suppress TDC bridging.

2.1.3 Objectives

Wang's [6] study primarily focused on the high speed range (above 2000rpm). However, as explained in Chapter 1, oil consumption at low speeds has been receiving increasing attention. Therefore, one objective of this study is to extend Wang's study to lower engine speeds.

Besides, a more in-depth understanding of the complete oil re-distribution process, especially the axial oil flow along a piston third land, is another objective of this study.

2.1.4 Structure of This Chapter

This chapter will mainly introduce a computational study on TDC bridging resulting from axial oil flow near a piston third land. In Section 2.2, background information of the computational simulations will be briefly described. Then, observations in the simulations will be explained in Section 2.3. Based on the observations, a few theoretical models on different phenomena have been developed. They will be presented in Section 2.4. Section 2.5 is focused on the critical oil quantity for TDC bridging estimated from simulation results. Section 2.6 will briefly summarize this chapter.

2.2 Simulation Setup

2.2.1 Variables to be Studied

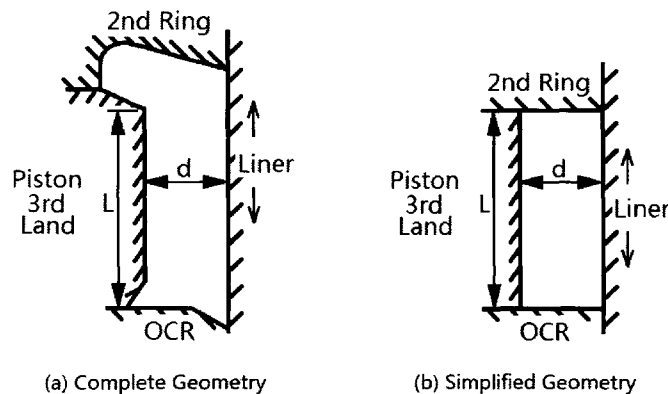


Figure 2.2 Geometry of computational domain

A complete re-distribution process is dependent of six categories of parameters:

1. Oil properties including density and viscosity.
2. Gas properties including density and viscosity;
3. Surface tension in an oil-gas interface;
4. Engine configuration including crank radius and connecting rod length;
5. Engine speed;
6. Geometric parameters including clearance between piston land and liner (d), axial height of piston land (L), dimensions of chamfers on piston and OCR, and all the geometric parameters of second ring hook. (See Figure 2.2 (a).)

The large number of relevant parameters will substantially complicate this study and prevent one from identifying the effect of each individual parameter. Thus, for simplicity, only a few of them will be studied in this work.

First, because the density and viscosity of gas are small compared to those of oil, the effects of gas are to be neglected. Second, since oil flow along a piston land is regarded the most significant sub-process, the hook and all the chamfers are to be neglected. That is, the computational domain is simplified to a rectangular cavity as shown in Figure 2.2 (b). Third, in this work, only the characteristics within the rectangular cavity will be focused on. For simplicity, the effects of engine configuration are not to be studied, though it will determine the body acceleration, which is the driving force of oil flow.

Then, six parameters are within the focus of this work: oil density, oil viscosity, surface tension, engine speed, piston-liner clearance and height of piston land. If one applies dimensional analysis, only three of them need to be varied in a computational simulation. In this work, kinematic viscosity of oil (ν), engine speed (N), and piston-liner clearance (d) are selected as the variables to be studied.

In this study, simulations were conducted at five engine speeds: 800, 1500, 2500, 3600, and 4500rpm. Four kinematic viscosities of oil were attempted: 1×10^{-6} , 3.125×10^{-6} (datum), 1×10^{-5} , and 5×10^{-5} m²/s. Three clearances were attempted: 0.5 (datum), 0.4, and 0.3mm. Oil density was kept constant at 800kg/m³, surface tension was fixed at 0.02N/m, and height of piston third land was kept at 2.5mm.

2.2.2 Initial Settings of Simulations

The simulations were conducted in the following steps.

First, all the variables were fixed. An oil film with a uniform thickness was laid on the piston land, as shown in Figure 2.3. A simulation started from TDC and lasted for three revolutions. In all simulations, the oil flow pattern had reached a realistic periodical flow pattern within two revolutions. Thus, the result in the third revolution is considered reliable.

If TDC bridging was observed in one simulation, the initial film thickness would be decreased by 10 μ m and a new simulation was to be conducted with the same parameters; if not, the initial film thickness would be increased by 10 μ m. This was repeated until the smallest oil thickness with which TDC bridging occurs and the largest thickness with which TDC bridging does not occur were found. The critical volume lies

within this range of $10\mu\text{m}$. Estimation was made based on the severity of TDC bridging in simulations.

Then, one parameter was changed, and another set of simulations were conducted.



Figure 2.3 Initialization of simulation. Red color denotes oil and blue color denotes gas.

2.3 Observations in Simulations

In this section, observations in computational simulations will be explained. Simulations with $d = 0.5\text{mm}$ and $\nu = 3.125 \times 10^{-6} \text{m}^2/\text{s}$ are to be presented as examples. The crank radius is 44mm and the connecting rod length is 158mm . With this engine configuration, body force switches direction at roughly 285° crank angle. Simulation results from 270° to 360° crank angle will be presented to demonstrate the complete process of TDC bridging.

Simulations at 800rpm and 4500rpm will be shown as examples to reveal the oil re-distribution at a low engine speed and a high engine speed, respectively. Figure 2.4 to Figure 2.6 show simulation results at 800rpm with an $80\mu\text{m}$ initial oil film, which is the thinnest with which TDC bridging occurs at 800rpm . Figure 2.7 to Figure 2.9 show simulation results at 4500rpm with a $30\mu\text{m}$ initial oil film, which is the thinnest with which TDC bridging occurs at 4500rpm . In these figures demonstrating oil distribution, red color denotes oil and blue color denotes gas.

2.3.1 At a Low Engine Speed

Figure 2.4 shows the streamlines and velocity field at 270° crank angle, 800rpm . The arrows in the right figure signify only the direction of velocity, while its magnitude is indicated by color. There are two primary vortices, one in the gas and one in the oil accumulated at the bottom. The vortex in the gas is in the clockwise direction in Figure 2.4. It results from a lid driven cavity flow. The vortex in the oil is in the counter-

clockwise direction in Figure 2.4. At this moment, body force is still downward. Therefore, the oil close to the piston land flows downward. However, because of the gas flow, oil on the interface flows upwards and towards the piston land. The difference in the velocity direction results in the vortex in oil. It is interesting to note that oil close to the interface starts to rise even when the body force is still downward. Another reason behind the early rise is surface tension, which adjusts the oil-gas interface profile to varying body force. The effect of surface tension will be discussed in Section 2.4.1.

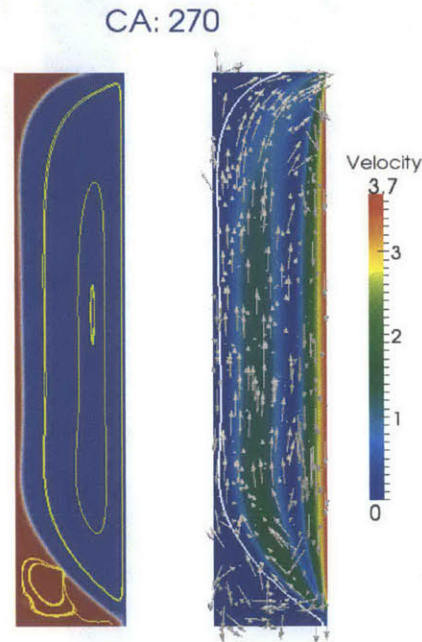


Figure 2.4 Oil distribution with streamlines (left) and velocity field (right) before body force switches to upward direction, 800rpm

Early rise also occurs in the thin base layer on piston land. Since the interface profile is almost flat there, it is caused dominantly by gas flow. Upward velocity first occurs in the layer at 277° crank angle, when the body force is still downward.

Figure 2.5 shows the complete oil re-distribution process before TDC bridging occurs. The body force switches to the upward direction at roughly 285° crank angle. However, by comparing the oil-gas interface at 276° and 285° crank angle, it can be found that the oil accumulated at the bottom has already crawled upward slightly when the body force is still downward. As will be explained in Section 2.4.1, this is caused by surface tension. After 285° crank angle, the oil cluster continues to adjust its shape under the effect upward body force and surface tension. Such adjustment continues until a thin film flow initializes on the piston land at 315° crank angle.

Then, oil rises along piston land in the form of a slender puddle. Details about this process will be explained in Section 2.4.4.

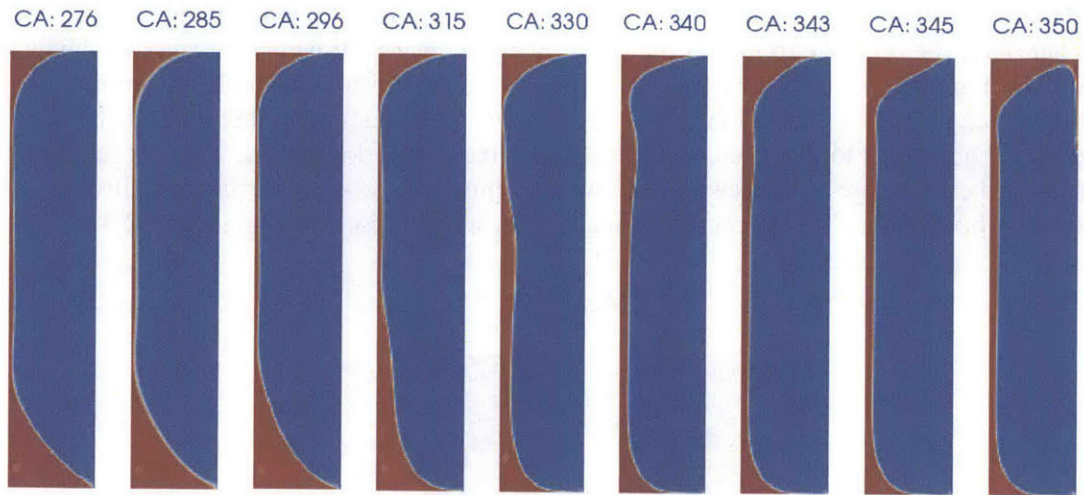


Figure 2.5 Complete evolution of TDC bridging, 800rpm

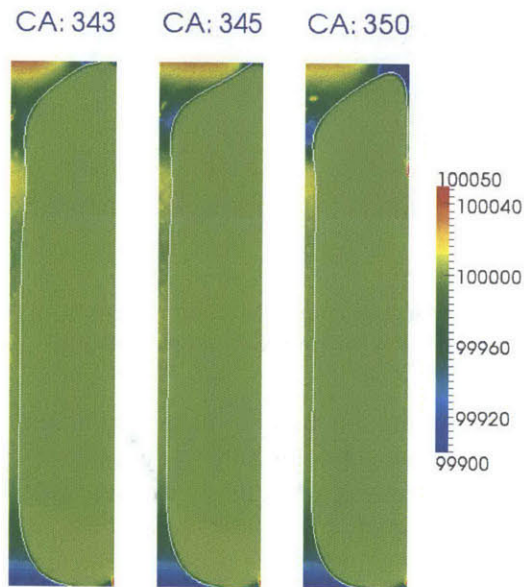


Figure 2.6 Pressure field, 800rpm (Gas pressure is almost uniform. It is set to be 100000Pa.)

After the puddle head reaches the lower flank of the second ring (340° crank angle), the oil will spread along the ring flank (343° and 345° crank angle). The pressure field during the spreading process is shown in Figure 2.6. The impact of oil generates a high pressure in the top left corner. The high pressure diverts the upcoming oil and drives the spreading oil. When the oil front reaches the liner, bridging occurs (350° crank angle). As shown in Figure 2.6, the pressure in the corner formed by second ring flank and liner

is low because of surface tension. Resultantly, an inverse pressure force exists in the oil layer on the liner, which prevents bridging. Thus, the bridging process is governed by the competition between viscous force caused by the liner motion and Laplace pressure associated with surface tension.

As can be observed in Figure 2.5 (after 330° crank angle), as the oil puddle rises along the piston land, there is always some oil left in the corner bounded by the upper OCR flank and the piston third land. The upward body force fails to drive it. The interface of this residual oil is in a circular shape. Actually, in the leftmost figure of Figure 2.5, there is a circular-shaped oil in the corner bounded by the lower second ring flank and the piston third land. This is the residual oil that the previous downward body force failed to drive. In real engine operations, the lower residual oil can possibly be drained through the clearance between an upper OCR flank and the OCR groove, which contributes to reduce oil consumption. However, the upper residual oil can possibly leak through a second ring clearance, which potentially increases oil consumption. A quantitative model on the circular residual oil will be presented in Section 2.4.2.

2.3.2 At a High Engine Speed

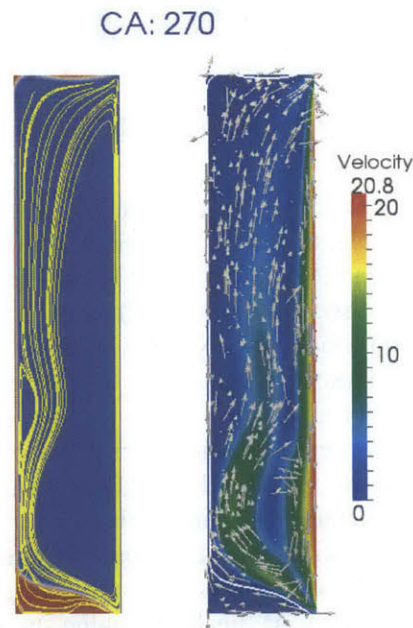


Figure 2.7 Streamlines (left) and velocity field (right) before body force switches to upward direction, 4500rpm

Figure 2.7 shows the velocity field at 270° crank angle, 4500rpm. While the vortex in gas is still present, vortex occupying the bulk of oil is not observed. Instead, the majority of oil is flowing upwards and towards the piston land. Since the quantity of oil is

smaller than that at 800rpm, a larger portion of oil is affected by the drag force of gas. Furthermore, body force varies more rapidly at higher engine speed, which results in a more rapid interface evolution. It indicates that the early rise is a more pronounced phenomenon at higher engine speeds.

Early rise in the base layer, which is dominated by gas flow, initiates at roughly 277° crank angle.

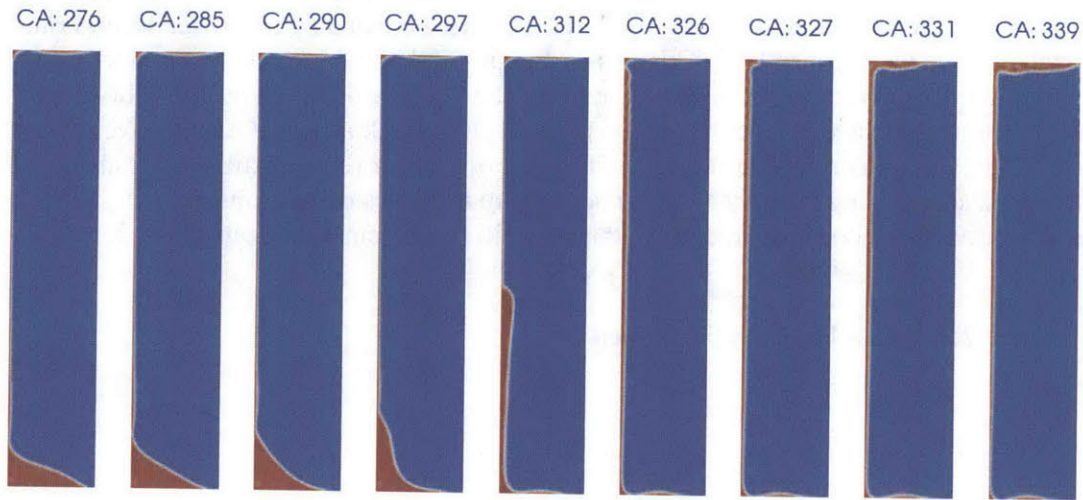


Figure 2.8 Complete evolution of TDC bridging, 4500rpm

Figure 2.8 shows the complete oil re-distribution process before TDC bridging occurs. It is qualitatively similar to that at a low speed (800rpm). The initialization of thin film flow takes less time, though the quantity of oil is smaller. Unlike the low speed case, oil spreads on the lower flank of second ring in the form of a thin film flow. This is because the radius of oil-gas interface in the vicinity of the top left corner is small compared to the piston-liner clearance. This will be explained in Section 2.4.3. The pressure field is demonstrated in Figure 2.9.

A circular residual oil also exists in the lower left corner. However, the quantity is remarkably smaller than that in the low speed case. Besides, there is also a small quantity of oil residing on the upper OCR flank. As can be observed in Figure 2.8 (297° crank angle), when a thin film flow initializes on the piston land, there is also a thin film flow on the upper OCR flank. The latter one is driven by pressure gradient, which is considerably weaker than body force. At this high engine speed, body acceleration is large, and therefore oil rises rapidly along the piston liner. The oil film on the OCR flank, driven by a weaker force, is not able to follow the rapid bulk flow on the piston land. As a result, a bottleneck between these two films forms on the OCR flank, as shown in Figure 2.8 (312° crank angle). The thin film on the OCR flank is eventually isolated by the bottleneck. After that, the shape of the residual oil layer is determined by the balance between surface tension and body force.

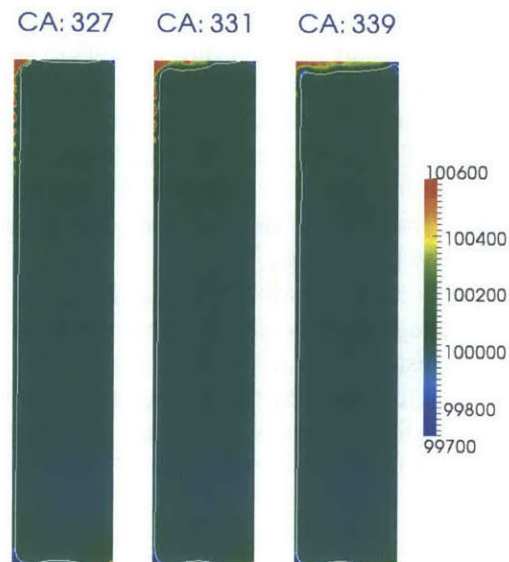


Figure 2.9 Pressure field, 4500rpm (Gas pressure is almost uniform. It is set to be 100000Pa.)

2.3.3 Closure

Based on the simulation results, descriptions of the oil re-distribution process a piston third land have been presented. The simulations results indicate that a complete re-distribution can be divided into a few sub-processes, including: an early rise of oil, initialization of a thin film flow on a piston land, oil rising on a piston land, formation of a circular residual oil, formation of a residual oil layer on a ring flank, oil spreading on a ring flank, and bridging.

2.4 Theoretical Analyses on a Few Sub-Processes

In Section 2.4.1, early rise caused by surface tension will be analyzed from a theoretical perspective. In Section 2.4.2, a theoretical model on circular residual oil will be presented. In Section 2.4.3, a theoretical model related to oil spreading will be presented. It will explain why a thin film flow on a lower ring flank occurs at high engines speeds only. In Section 2.4.4, oil rising along a piston land, which is considered the most important sub-process, will be modeled.

2.4.1 Early Rise Resulting from Surface Tension

Since the surface tension of oil and gas is relatively small (roughly 0.02N/s), it was assumed that oil fully wets the solid surfaces. That is, the contact angle is 0° in the simulations. Thus, when the body force is still downward, the oil accumulated on an upper OCR flank tends to spread to the farthest possible location, which is a liner. Because of the downward motion of the liner, the contact line is not able to climb up

along the liner.³ Thus, a practical assumption is that the lower edge of the oil-gas interface is fixed at the intersection of the liner and the upper OCR flank. It is approximately the case in the simulations. (See Figure 2.5 and Figure 2.8.)

As can be observed in the leftmost figure in Figure 2.5 and Figure 2.8, a thin base layer exists on the piston land. The interface of the oil cluster at the bottom must connect smoothly with the interface of the film. Since the thickness of base layer is negligible compared to the piston-liner clearance, it can be assumed that the upper edge of the oil-gas interface is tangential to the piston land.

In order to qualitatively explain how the oil-gas interface evolves under a variant body acceleration, a quasi-steady analysis is to be presented below. Given that oil velocity in the accumulated cluster is small, dynamic forces are negligible. Therefore, the interface profile is primarily determined by the balance between surface tension and instant body force. Surface tension generates a pressure difference across the oil-gas interface, which satisfies the Young-Laplace equation:

$$p_{oil} - p_{gas} = -\frac{\sigma}{R} \quad (2.1)$$

where p_{oil} is oil pressure, p_{gas} is gas pressure, σ is surface tension, and R is local radius of interface from gas side. According to this equation, pressure in the oil cluster is smaller than gas pressure, which is approximately uniform except for the vicinity of singularity. If R varies gradually along the interface, a hydrostatic pressure field can be generated in the oil to balance the body force.

Figure 2.10 (a) is a schematic diagram of an oil-gas interface under a certain downward body force. It will be taken as the reference in this analysis. It will be assumed that an equilibrium state has been reached at every instant, that is, the interface evolves in a quasi-static manner. The oil pressure increases in the downward direction. Thus, according to Equation (2.1), local radius of oil surface must increase in the same direction.

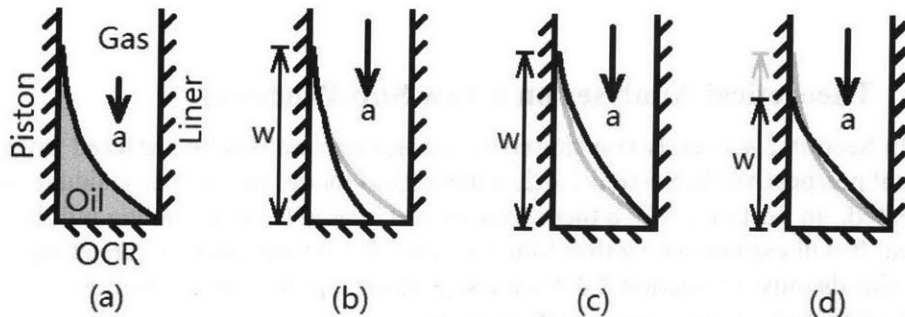


Figure 2.10 Schematic diagram of oil-gas interface under variant body acceleration.

³ When surface tension is increased to 0.2N/m, which is an unrealistic value, simulations showed that the contact line can climb onto the liner. However, it has not been observed in all existing simulations with a 0.02N/m surface tension.

Figure 2.10 (b) shows a possible interface profile under a larger downward body force. The upper edge of the interface is retained at the same location. If the local radius does not change at the upper end, the oil pressure there does not vary from the reference state. As a result of the larger body acceleration, the oil pressure at the bottom must increase from the reference state, indicating an increase in local interface radius. Thus, the interface will vary from the reference state (grey curve in Figure 2.10 (b)) to a new state (black curve in Figure 2.10 (b)). In this case, the lower edge of the interface cannot stretch to the liner.

Thus, if the upper edge of interface does not move, the local interface radius there must decrease so that the lower edge can reach to the liner. Figure 2.10 (c) schematically illustrates such an interface. However, the volume of the oil cluster increases. Since the computational domain is assumed to be perfectly sealed, oil quantity is conserved. At a crank angle of roughly 270° , downward body force has been in effect for about half a revolution and most oil in the cavity are accumulated at the bottom. Thus, the volume of the oil cluster is approximately constant. The interface in black color shown in Figure 2.10 (c) contradicts with this assumption.

Thus, the upper edge of the oil-gas interface cannot remain at the same location under an increased body acceleration. If the lower edge is to be fixed at the intersection between the liner and the OCR flank, and simultaneously the oil volume is to be conserved, the upper edge must move downward, as shown in Figure 2.10 (d). That is, the height of the oil cluster, w , decreases with downward body acceleration.

The analysis above explains why the oil accumulated on the upper OCR flank crawls upwards before the body force switches direction at 285° crank angle. As the downward body force decreases, the upper edge of the interface moves upwards. In a real engine operation, steady state may not be reached. However, the same trend can be expected.

2.4.2 Circular Residual Oil

In this section, the shape of a circular residual oil will be modeled theoretically. The model can also predict the quantity of oil within a circular residual oil, which provides more information on how much oil can potentially leak into a ring groove.

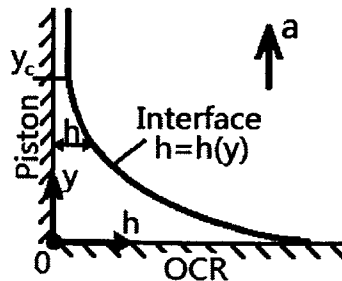


Figure 2.11 Schematic diagram of circular residual oil

Figure 2.11 shows the coordinate system in the model. The oil-gas interface is regarded as a function of y , where y is the coordinate along piston land, and h is the local oil thickness.

Since the oil velocity in the residual oil is small, dynamic effects and viscous effects are to be neglected. It is assumed that the gas pressure is uniformly zero. A quasi-static balance between body force and surface tension gives:

$$p = \sigma \frac{-\frac{d^2h}{dy^2}}{\left[1 + \left(\frac{dh}{dy}\right)^2\right]^{\frac{3}{2}}} = -\rho a(y_c - y) \quad (2.2)$$

where σ is surface tension of oil and gas, ρ is oil density, a is body acceleration, and y_c is the location where the circular residual oil connects with oil film on piston land. The interface of the oil film on piston land is approximately flat. Thus, the oil pressure there is approximately zero. A continuity of pressure indicates that oil pressure at y_c is zero.

Since oil is assumed fully wetting, the receding contact angle on OCR flanks is zero. That is:

$$\left.\frac{dh}{dy}\right|_{y=0} \rightarrow -\infty \quad (2.3)$$

Integrating Equation (2.2) with the boundary condition (2.3), we get:

$$\frac{\frac{dh}{dy}}{\left[1 + \left(\frac{dh}{dy}\right)^2\right]^{\frac{1}{2}}} = \frac{\rho a}{\sigma} \left(y_c y - \frac{y^2}{2}\right) - 1 \quad (2.4)$$

Another boundary condition is:

$$\left.\frac{dh}{dy}\right|_{y=y_c} = 0 \quad (2.5)$$

Equation (2.4) and (2.5) gives:

$$y_c = \sqrt{\frac{2\sigma}{\rho a}} \quad (2.6)$$

After some algebra, Equation (2.4) becomes:

$$\frac{dh}{dy} = -\sqrt{\frac{(\eta - 1)^4}{1 - (\eta - 1)^4}} \quad (2.7)$$

where

$$\eta = \frac{y}{y_c} \quad (2.8)$$

Then, the interface profile can be obtained by integrate Equation (2.7):

$$\frac{h}{y_c} = \int_1^\eta -\sqrt{\frac{(\eta - 1)^4}{1 - (\eta - 1)^4}} d\eta \quad (2.9)$$

Equation (2.9) is evaluated numerically with Simpson's Rule. 20000 grids were employed. The result is plotted in Figure 2.12. The width of residual oil on OCR flank is roughly 0.6 times y_c .

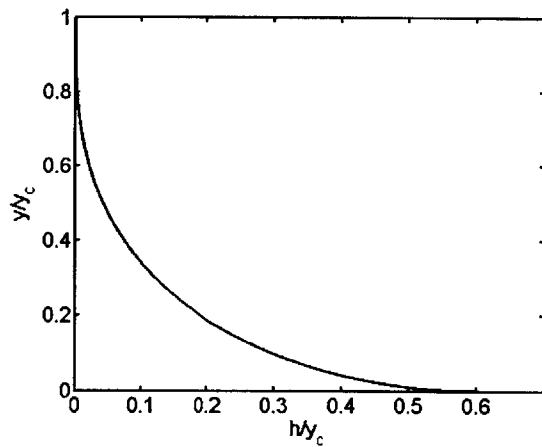


Figure 2.12 Interface profile of circular residual oil, normalized by y_c .

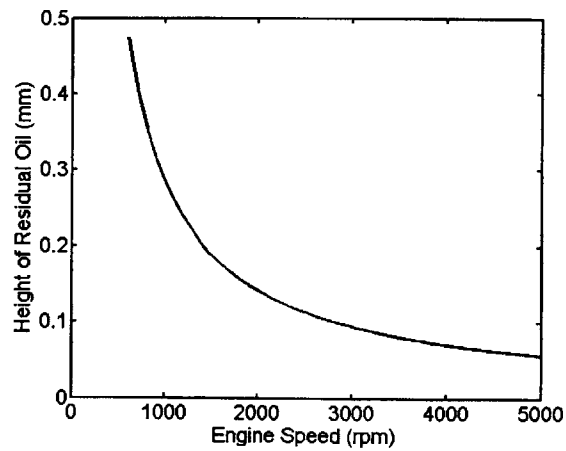


Figure 2.13 Height of circular residual oil along piston land ($\sigma = 0.02\text{N/n}$, $\rho = 800\text{kg/m}^3$, $r = 44\text{mm}$, $l = 158\text{mm}$)

By replacing a in Equation (2.6) with the maximum upward body acceleration, the value of y_c can be calculated at a given engine speed. It is plotted against engine speed in Figure 2.13. The results coincide with simulations. The dimension of the upper residual oil can be calculated by plugging in the maximum downward body acceleration.

Equation (2.6) implies that the dimension of circular residual oil decreases substantially with body acceleration. However, in the simulations, it almost remains constant with time. After the majority of oil has rose along the piston land, the oil film on the piston land is thin. Equation (1.2) implies that oil velocity in the thin base layer is small. Thus, residual oil enters the base layer at a very limited rate, and therefore its volume hardly varies. Although this dynamic effect has not been considered in the model, the coincidence between modeling and simulation suggests that the formation of circular residual oil indeed results from the balance between surface tension and body force. Strictly speaking, because body acceleration varies with time, only a scaling rule can be drawn from this analysis. However, the coefficient of scaling predicted by maximum body acceleration fortunately coincides with simulation results. Thus, it will be taken as the final solution.

The volume of circular residual oil per unit width (V_{cir}) can be obtained by numerically integrating h . The result is:

$$V_{cir} = 0.08 \cdot \frac{\sigma}{\rho a} \quad (2.10)$$

It implies how much oil may potentially leak through the clearance between a ring flank and the ring groove. However, in order to determine how much oil indeed leaks, a more detailed analysis on the oil flow in the clearance is in need. The pressure distribution in the circular residual oil constitutes a boundary condition of it. However, the effect of ring-groove clearance is beyond the scope of this work.

2.4.3 Oil Junction between Piston Land and Lower Ring Flank

As described in Section 2.3.2 and Figure 2.8, after oil on piston land reaches the lower second ring flank, the oil layers on the piston land and on the lower second ring flank are connected through a rounded interface. This section presents a theoretical model on this rounded oil junction. The modeling results will explain why a thin film flow on the lower second ring flank occurs at high engine speeds only.

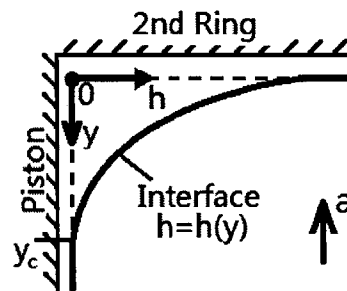


Figure 2.14 Schematic diagram of rounded oil junction

Figure 2.14 shows the coordinate system in this model. The modeling method resembles that for a circular residual oil, as presented in Section 2.4.2. The governing equation is:

$$p = \sigma \frac{-\frac{d^2h}{dy^2}}{\left[1 + \left(\frac{dh}{dy}\right)^2\right]^{\frac{3}{2}}} = -\rho ay \quad (2.11)$$

where σ is surface tension of oil and gas, ρ is oil density, a is body acceleration, y and h are the coordinates shown in Figure 2.14. Here, the oil pressure at $y = 0$ is zero because it is connected with an approximately flat film there. It is noted that the oil pressure at $y = y_c$, which is location where the rounded junction connects with oil layer on a piston land, is not zero. This is demonstrated in Figure 2.6 and less observable in Figure 2.9. It can also be shown that the boundary condition $p(y = y_c) = 0$ will not provide a physically valid result.

Integrating Equation (2.11) with the boundary condition

$$\left.\frac{dh}{dy}\right|_{y=0} \rightarrow -\infty \quad (2.12)$$

we get:

$$\frac{\frac{dh}{dy}}{\left[1 + \left(\frac{dh}{dy}\right)^2\right]^{\frac{1}{2}}} = \frac{\rho a}{2\sigma} y^2 - 1 \quad (2.13)$$

The location of y_c is determined by:

$$\left.\frac{dh}{dy}\right|_{y=y_c} = 0 \quad (2.14)$$

which gives:

$$y_c = \sqrt{\frac{2\sigma}{\rho a}} \quad (2.15)$$

It is noted that the height of a oil junction is the same as the height of a circular residual oil under the same body acceleration.

Equation (2.13) gives an equation for $\frac{dh}{dy}$, which can be then numerically integrated to obtain $h(y)$. The result is shown in Figure 2.15.

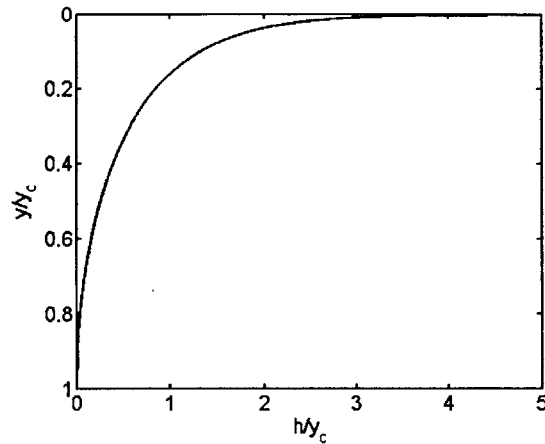


Figure 2.15 Interface profile of rounded oil junction, normalized by y_c

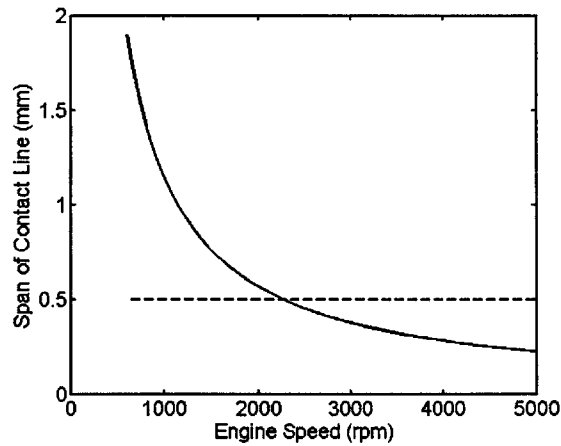


Figure 2.16 Span of rounded oil junction along lower second ring flank ($\sigma = 0.02N/n$, $\rho = 800kg/m^3$, $r = 44mm$, $l = 158mm$)

The span of the rounded oil junction along a lower second ring flank is roughly 4 times y_c , which is much larger than the width of circular residual oil. The span under the maximum upward body force at a certain engine speed is shown in Figure 2.16. At low speeds, the span exceeds the clearance between piston third land and liner, which is indicated by the dashed line in Figure 2.16. This is why a thin film flow on lower second ring flank was not observed at 800rpm. At high speeds, the span is smaller than the clearance, and a thin film flow can be observed on the lower second ring flank.

2.4.4 Axial Flow along Piston Land

A theoretical model of axial oil rising along piston third land will be shown in this section.

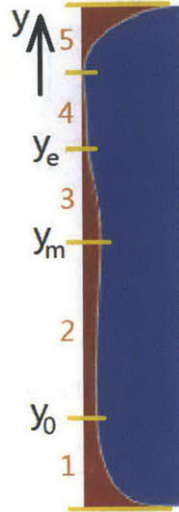


Figure 2.17 Division of oil along piston third land during oil rises

As can be observed in Figure 2.5 and Figure 2.8, before the front edge of oil reaches the second ring flank, the oil can be mostly divided into five regions (See Figure 2.17): 1) a circular-shaped oil cluster on the upper OCR flank; 2) an oil film with relatively flat interface on the piston land; 3) an oil puddle head with relatively abrupt interface profile on the piston land; 4) a base layer on the piston land; 5) the circular residual oil on the lower second ring flank. The volume of every region adds up to the total oil volume, which is a constant in every simulation. The volume of the base layer (region 4) is small compared to the total volume. It will be neglected. The volume of the upper residual oil (region 5) can be calculated with Equation (2.10) by plugging in the maximum downward body acceleration. The oil volumes in the first three regions remain to be analyzed. The common idea is to obtain the profile of the oil-gas interface in each region, and then integrate the profile to obtain the oil volume per unit width.

2.4.4.1 Region 2: Tail of Oil Puddle

Region 2 can be modeled with lubrication theory. The governing equation is:

$$\frac{\partial v}{\partial t} = -\frac{1}{\rho} \frac{\partial p}{\partial y} + \nu \frac{\partial^2 v}{\partial x^2} + a \quad (2.16)$$

where v is the velocity component along y direction, t is time, ρ is oil density, p is oil pressure, x and y are coordinates shown in Figure 2.18, ν is kinematic viscosity of oil, and a is body acceleration. A rough scaling implies that the transient term can be neglected. Furthermore, since the oil interface is approximately flat in region 2, oil

pressure will be approximately equal to the gas pressure, which is almost constant. Thus, the pressure gradient will be neglected. Then:

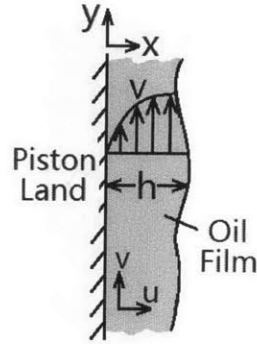


Figure 2.18 Schematic diagram of the model for region 2 (Not to scale)

$$0 \approx \nu \frac{\partial^2 v}{\partial x^2} + a = \nu \frac{\partial^2 v}{\partial x^2} - a_p \quad (2.17)$$

where a_p is the acceleration of a piston. The boundary conditions for Equation (2.17) are:

$$v(x = 0) = 0 \quad (2.18)$$

$$\left. \frac{\partial v}{\partial x} \right|_{x=h} \approx 0 \quad (2.19)$$

Integrating Equation (2.17) twice, we get:

$$v = \frac{a_p}{2\nu} (x^2 - 2hx) \quad (2.20)$$

By integrating Equation (2.20), the volume flux of oil per unit width (q) is obtained:

$$q = \int_0^h v dx = -\frac{a_p h^3}{3\nu} \quad (2.21)$$

Mass conservation requires that:

$$\frac{\partial h}{\partial t} + \frac{\partial q}{\partial y} = \frac{\partial h}{\partial t} - \frac{a_p}{\nu} h^2 \frac{\partial h}{\partial y} = 0 \quad (2.22)$$

Here, the modeling method of Thirouard [7, p. 96] is followed. By dividing a_p , Equation (2.22) becomes:

$$\frac{\partial h}{\partial V_p} - \frac{1}{\nu} h^2 \frac{\partial h}{\partial y} = 0 \quad (2.23)$$

where V_p is the piston velocity. Equation (2.23) is a quasi-linear equation. The solution is:

$$h = \sqrt{\frac{v}{V_{\max} - V_p} (y - y_0)} \approx \sqrt{\frac{v}{V_{\max} - V_p} y} \quad (2.24)$$

where V_{\max} is the piston velocity when $a = 0$, y_0 is the initial position of oil particles. The approximation in Equation (2.24) is valid when the dimension of the accumulated oil is small compared to the axial height of the piston land, and/or at a late stage of oil flow when $y \gg y_0$.

For simplicity, denote:

$$D = \frac{v}{V_{\max} - V_p} \quad (2.25)$$

where D is a function of time or crank angle. It can be calculated with the piston motion equation:

$$V_p = \omega \cdot \left(-r \sin \theta - \frac{r^2 \sin(2\theta)}{2\sqrt{l^2 - r^2 \sin^2 \theta}} \right) \quad (2.26)$$

where ω is engine speed in radians per second, r is crank radius, l is connecting rod length, and θ is crank angle with 0° at TDC and 180° at BDC.

A dimensionless variable is introduced:

$$\eta = \frac{y}{D} \quad (2.27)$$

Then:

$$h = \sqrt{Dy} = D\sqrt{\eta} \quad (2.28)$$

$$\frac{\partial h}{\partial y} = \frac{1}{2} \sqrt{\frac{D}{y}} = \frac{1}{2} \sqrt{\frac{1}{\eta}} \quad (2.29)$$

Thus, the oil volume per unit width in region 2 is:

$$V_2 = \int_{y_0}^{y_m} h dy = \frac{2}{3} \sqrt{D} \left(y_m^{\frac{3}{2}} - y_0^{\frac{3}{2}} \right) \quad (2.30)$$

2.4.4.2 Region 1: Circular Oil Cluster

The oil-gas interface profile in Region 1 is dominantly determined by the balance between surface tension and body force. Following the method presented in Section 2.4.2, the following equation for the oil interface can be obtained:

$$\frac{h_y}{(1 + h_y^2)^{\frac{1}{2}}} = F(\gamma) = -\gamma^2 + 2\gamma_0\gamma - 1 \quad (2.31)$$

where subscript y denotes the derivative with respect to y , y_0 is where region 1 connects with region 2 (See Figure 2.19), and γ is a dimensionless variable defined as:

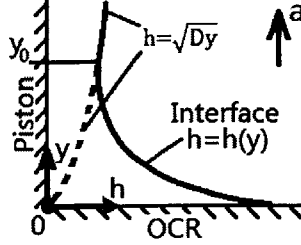


Figure 2.19 Schematic diagram of the model for region 1 (Not to scale)

$$\gamma = y \sqrt{\frac{\rho a}{2\sigma}} \quad (2.32)$$

One underlying assumption is that Laplace pressure in region 2 is negligible. Therefore, $p(y = y_0) = 0$.

Continuity of slope requires that:

$$h_y(y = y_0) = h_y(\gamma = \gamma_0) = \frac{1}{2} \sqrt{\frac{\alpha}{\gamma}} \quad (2.33)$$

where α is an dimensionless parameter dependent of time or crank angle:

$$\alpha = D \sqrt{\frac{\rho a}{2\sigma}} \quad (2.34)$$

Plug Equation (2.33) into Equation (2.31), we get:

$$\gamma_0^2 - 1 = \frac{1}{\left(\frac{4\gamma_0}{\alpha} + 1\right)^{\frac{1}{2}}} \quad (2.35)$$

Equation (2.35) is the equation for γ_0 . At a given crank angle, α can be simply calculated with Equation (1.1), (2.25), and (2.26). γ_0 is numerically solved at every time step with the secant method, and the value of γ_0 is plugged into Equation (2.31) to obtain $F(\gamma)$. Then, the interface profile can be evaluated by integrating h_y :

$$h = h_0 + \int_{y_0}^y h_y dy = \sqrt{\frac{2\sigma}{\rho a}} \left(\sqrt{\alpha \gamma_0} + \int_{\gamma_0}^{\gamma} \frac{F}{\sqrt{1 - F^2}} d\gamma \right) \quad (2.36)$$

Oil volume per unit width in region 1 is calculated by integrating Equation (2.36):

$$V_1 = \frac{2\sigma}{\rho a} \left(\sqrt{\alpha \gamma_0^3} + \int_0^{\gamma_0} \int_{\gamma_0}^{\gamma} \frac{F}{\sqrt{1-F^2}} dy' dy \right) \quad (2.37)$$

2.4.4.3 Region 3: Head of Oil Puddle

In the head of the oil puddle, surface tension comes into effect to modify the interface profile. As illustrated by the grey curves in Figure 2.20, oil rolls over toward the piston land and is prevented from detaching from the solid surface. Thus, oil flow in this region is two-dimensional and lubrication theory cannot be applied.

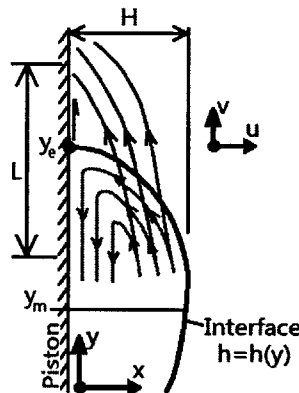


Figure 2.20 Schematic diagram of the model for region 3 (Not to scale)

The grey curves in Figure 2.20 sketches the streamlines in a reference frame moving with the contact line y_e . If the piston land is taken as the reference frame, the streamlines would intersect with the oil interface. (See the black curves in Figure 2.20.) Thus, as long as the contact line is moving at a reasonable speed, the length scale for velocity in y direction (L) is larger than the length scale of oil interface in y direction. As can be observed in Figure 2.5, at a low speed, the length scale of oil interface in y direction is larger than that in x direction. On the other hand, Figure 2.8 implies that, at high engine speeds, the length scales of oil interface are comparable in both x and y directions. However, the speed of contact line is larger at higher engine speeds. Thus, it is not inappropriate to assume that:

$$\epsilon = \frac{H}{L} \ll 1 \quad (2.38)$$

where H is the length scale in x direction as shown in Figure 2.20. It roughly scales with the maximum thickness of oil film on piston land.

If the relevant variables are non-dimensionalized as follows:

$$\tilde{x} = \frac{x}{H} \quad \tilde{y} = \frac{y}{L} \quad \tilde{v} = \frac{v}{V} \quad \tilde{u} = \frac{u}{\epsilon V} \quad \tilde{t} = \frac{t}{L/V} \quad \tilde{p} = \frac{p}{p_c} = p \cdot \frac{H^2}{\sigma L} \quad (2.39)$$

the Navier Stokes Equations become:

$$\epsilon \text{Fr} \left(\frac{\partial \tilde{v}}{\partial \tilde{t}} + \tilde{u} \frac{\partial \tilde{v}}{\partial \tilde{x}} + \tilde{v} \frac{\partial \tilde{v}}{\partial \tilde{y}} \right) = -\frac{1}{\text{Bo}} \frac{\partial \tilde{p}}{\partial \tilde{y}} + \frac{\text{Ca}}{\text{Bo}} \left(\frac{\partial^2 \tilde{v}}{\partial \tilde{x}^2} + \epsilon^2 \frac{\partial^2 \tilde{v}}{\partial \tilde{y}^2} \right) + 1 \quad (2.40)$$

$$\epsilon^2 \text{Fr} \left(\frac{\partial \tilde{u}}{\partial \tilde{t}} + \tilde{u} \frac{\partial \tilde{u}}{\partial \tilde{x}} + \tilde{v} \frac{\partial \tilde{u}}{\partial \tilde{y}} \right) = -\frac{1}{\epsilon \text{Bo}} \frac{\partial \tilde{p}}{\partial \tilde{x}} + \frac{\text{Ca}}{\text{Bo}} \left(\frac{\partial^2 \tilde{u}}{\partial \tilde{x}^2} + \epsilon^2 \frac{\partial^2 \tilde{u}}{\partial \tilde{y}^2} \right) \quad (2.41)$$

where Fr is the Froude number, Ca is the capillary number, and Bo is the Bond number:

$$\text{Fr} = \frac{V^2}{aH} \quad \text{Ca} = \frac{\mu V}{\sigma} \quad \text{Bo} = \frac{\rho a H^2}{\sigma} \quad (2.42)$$

It should be noted that the length scale for pressure in y direction is H instead of L. It is because that pressure is associated with the interface profile, which is approximately circular. Thus:

$$\frac{\partial p}{\partial x} \sim \frac{\sigma}{H^2} \sim \frac{p_c}{L} \quad \Rightarrow \quad p_c = \frac{\sigma L}{H^2} \quad (2.43)$$

This is how the characteristic pressure in Equation (2.39) is determined.

During the oil rising process, the capillary number (Ca) is roughly 0.0375 at 800rpm and 0.375 at 4500rpm. It is much smaller than 1 especially at low engine speeds. Thus, the viscous term is negligible compared to the pressure term. This assumption is more valid at low engine speeds. Moreover, if the first-order and second-order terms of ϵ are neglected, Equation (2.40) and (2.41) becomes:

$$\frac{\partial p}{\partial y} \approx \rho a \quad (2.44)$$

$$\frac{\partial p}{\partial x} \approx 0 \quad (2.45)$$

which indicates that the primary force balance in the puddle head is between body force and pressure force. The latter one results from surface tension. Thus, the oil interface can be modeled with exactly the same method as that for region 1. Continuity of oil pressure and interface profile, and smoothness of interface profile (continuity of first order derivative) provide boundary conditions. One can eventually get:

$$V_3 = \frac{2\sigma}{\rho a} \left(\alpha \beta_e \sqrt{\eta_m} + \int_0^{\beta_e} \int_0^{\beta} \frac{G}{\sqrt{1-G^2}} d\beta' d\beta \right) \quad (2.46)$$

where

$$G = -\beta^2 + \frac{1}{\sqrt{4\eta_m + 1}} \quad (2.47)$$

$$\beta = (y - y_m) \sqrt{\frac{\rho a}{2\sigma}} \quad (2.48)$$

where y_m is the location where region 2 and 3 connects (See Figure 2.17 and Figure 2.20.), and β_e is specified by:

$$\alpha\sqrt{\eta_m} + \int_0^{\beta_e} \frac{G}{\sqrt{1-G^2}} d\beta = 0 \quad (2.49)$$

Equation (2.49) is first solved numerically with the secant method to obtain β_e as a function of η_m . More details about the solution procedure will be described in Appendix 1. Then, V_3 (Equation (2.46)) becomes a function of η_m only.

2.4.4.4 Summing Up Oil Volume

In order to solve for y_m or y_e , mass conservation equation needs to be solved:

$$V_1 + V_2 + V_3 = V_{\text{total}} - V_5 \quad (2.50)$$

where V_{total} is the total amount of oil that is initially added into the computational domain, V_5 is the amount of residual oil in region 5. In one single simulation, the right hand side of Equation (2.50) is a constant and can be calculated. Among the three terms on the left, V_1 can be calculated at each time step directly from Equation (2.37). It is because the unknown variable γ_0 can be determined from Equation (2.35). The remaining two terms cannot be pre-determined because they are dependent of η_m , which is to be solved from Equation (2.50). Plugging Equation (2.30), (2.37), and (2.46) into (2.50), we get:

$$\begin{aligned} & \frac{2}{3}\alpha^2\eta_m^{\frac{3}{2}} + \alpha\eta_m^{\frac{1}{2}}\beta_e + \int_0^{\beta_e} \int_0^{\beta} \frac{G}{\sqrt{1-G^2}} d\beta' d\beta \\ & = (V_{\text{total}} - V_5) \cdot \frac{\rho a}{2\sigma} + \frac{2}{3}\alpha^{\frac{1}{2}}\gamma_0^{\frac{3}{2}} - \sqrt{\alpha\gamma_0^3} - \int_0^{\gamma_0} \int_{\gamma_0}^{\gamma} \frac{F}{\sqrt{1-F^2}} d\gamma' d\gamma \end{aligned} \quad (2.51)$$

At each time step, α and a are constant and known. Thus, Equation (2.51) can be solved at each time step to obtain η_m , and then y_m and y_e (See Figure 2.17.). The results are demonstrated in Figure 2.21. The solid blue curves show the location of y_m , the green curves show the location of y_e , and the red curves show the length of oil puddle head ($y_e - y_m$). The length of the puddle head decreases in time. It also decreases with engine speed, which coincides with the simulation results shown in Figure 2.5 and Figure 2.8.

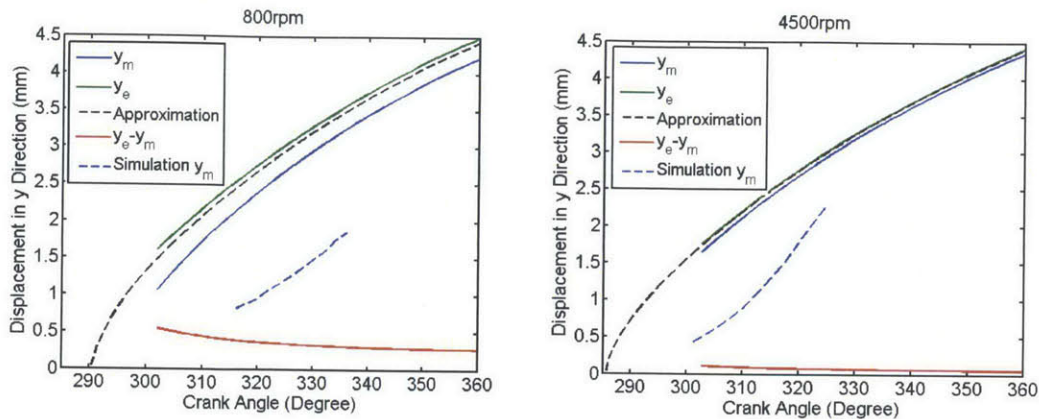


Figure 2.21 Results of oil rising model (Left: 800rpm; right: 4500rpm)

One approach to simplify Equation (2.51) is to neglect the puddle head (Region 3). That is, the last two terms on the left is to be neglected. In this case, η_m can be very simply solved. The solutions are shown by the dashed black curves in Figure 2.21. It satisfactorily approximates the exact solution at high speeds. However, at low speeds, the discrepancy between the approximate solution and the exact solution is noticeable. This is because the size of the puddle head is less negligible at a lower speed. Figure 2.22 shows the volume ratio of the tail of the puddle, which is the ratio between the first term on the left of Equation (2.51) and its right hand side. It indicates that this ratio is closer to 1 at a higher speed, which justifies the fact that the approximate solution is closer to the exactly solution. The ratio approaches 1 as time elapses, which implies that the approximate solution is more accurate at a later time. Given that the interface profile of the tail is hardly affected by surface tension, while the head is to a larger extent, it is deemed that surface tension has a more pronounced effect on the puddle rising process at a lower engine speed and/or a earlier stage of oil rising.

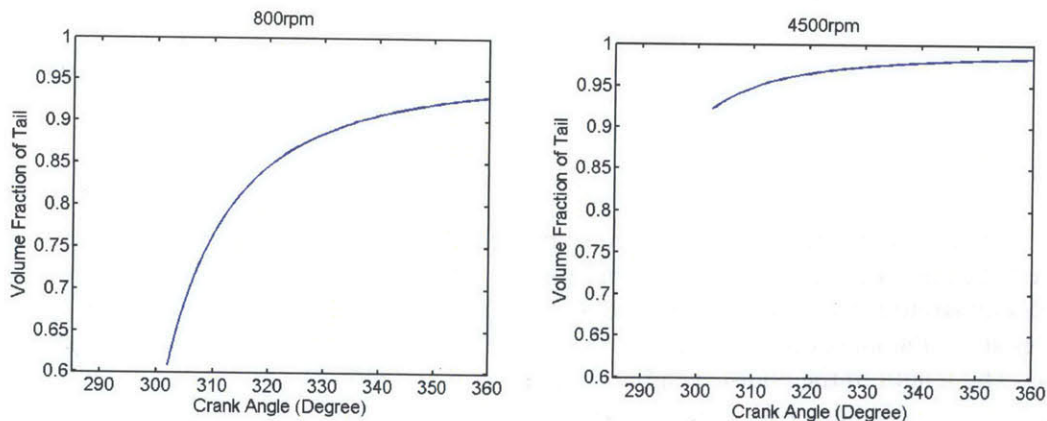


Figure 2.22 Volume ratio of puddle tail (Left: 800rpm; right: 4500rpm)

The discussion presented above implies that the modeling method by Thirouard [7], in which the puddle head is treated as a shock and surface tension is not explicitly incorporated, is proper at a high engine speed and/or at a late stage of oil flow. The effect of surface tension makes his model less valid at lower speeds.

The dashed blue curves in Figure 2.21 show the location of y_m in simulations. The model predicts a remarkably more rapid rising than the simulations. It is deemed that the discrepancy primarily results from the approximation made in Equation (2.24). That is, y_0 cannot be justifiably neglected. The axial length of the piston land is not significantly larger than the dimension of the oil cluster accumulated on the upper OCR flank. That is, $y \gg y_0$ is not a valid assumption. The fact that the discrepancy tends to decrease⁴ with time supports this argument.

The discrepancy indicates that a proper initial condition is crucial to an accurate model. However, it should be noted that y_0 should not be determined by the interface profile at 285° crank angle. Before the thin film flow is initialized, oil flow is dominantly governed by surface tension. The three-region modeling is not valid during the initialization process. Thus, the oil interface profile at the end of the initialization process should be taken as the initial condition (y_0). The fact that Equation (2.51) does not have a solution at a small time also implies that another modeling approach is required for the initial stage. The discussions above imply that the accuracy of the model presented in this report, as well as Thirouard's [7] model, is largely limited by the lack of a proper initial condition. It is suggested that attention should be paid to the initialization process in future research.

2.5 Critical Oil Quantity

This section is focused on the critical oil quantity for TDC bridging in a rectangular cavity. In Section 2.5.1, the critical quantity based on simulation results will be presented. In the results to be shown, oil density is 800kg/m^3 , surface tension is 0.02N/m , and axial height of piston third land is 2.5mm . The effects of engine speed, oil viscosity, and piston-liner clearance will be explained. In Section 2.5.2, a scaling analysis will be presented to justify the simulation results.

2.5.1 Critical Oil Quantity Based on Simulations

Figure 2.23 demonstrates how the critical oil quantity varies with engine speed. As expected, it decreases with engine speed. The critical quantity increases with oil viscosity because viscous force prevents the axial oil flow. (See Equation (1.2)) The curves are plotted in both a normal scale and a logarithmic scale. In a logarithmic scale, the curves are approximately straight lines, implying a possible power law. That is:

⁴ This trend is not clearly shown in Figure 2.21 left because the dashed blue curve terminates when the puddle head reaches the second ring. However, this trend is evident at all the other engine speeds simulated. For coherence, not all the results are presented here.

$$V_{\text{critical}} \propto N^{\beta} \quad (2.52)$$

where V_{critical} is the critical oil quantity measured in cross sectional area, N is engine speed.

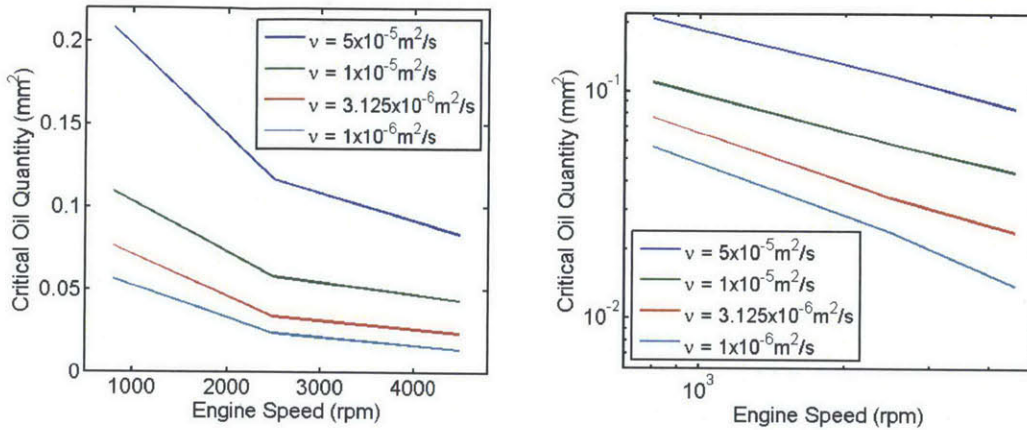


Figure 2.23 Critical oil quantity against engine speed. $d = 0.5\text{mm}$, with different ν . (Left: normal scale; right: logarithmic scale)

The value of β at each oil viscosity is shown in Table 2.1. It increases and converges to -0.5 as oil viscosity increases. This result will be discussed in Section 2.5.2.

Table 2.1 Index of power law between critical oil quantity and engine speed

ν (m^2/s)	1×10^{-6}	3.125×10^{-6}	1×10^{-5}	5×10^{-5}
B	-0.8056	-0.6807	-0.5337	-0.5237

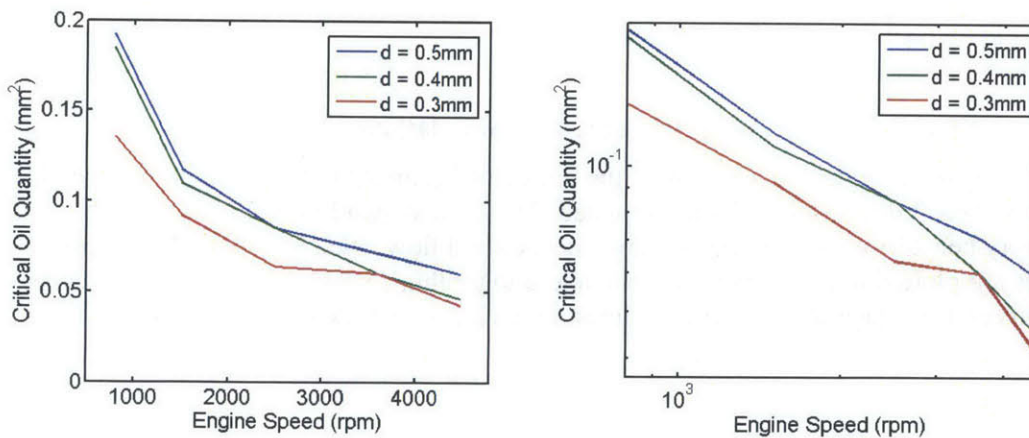


Figure 2.24 Critical oil quantity against engine speed. $\nu = 3.125 \times 10^{-6} \text{m}^2/\text{s}$, with different d . (Left: normal scale; right: logarithmic scale)

Figure 2.24 shows how the critical oil quantity varies with engine speed when the piston-liner clearance varies. The values of β are listed in Table 2.2. It does not vary in an obvious manner with piston-liner clearance.

Table 2.2 Index of power law between critical oil quantity and engine speed

d (mm)	0.3	0.4	0.5
β	-0.6256	-0.7687	-0.6595

Figure 2.25 shows how the critical oil quantity varies with kinematic viscosity of oil. It increases with oil viscosity and decreases with engine speed, which coincides with foregoing analyses. The curves in a logarithmic scale are approximately straight lines, implying a possible power law:

$$V_{\text{critical}} \propto \nu^\gamma \quad (2.53)$$

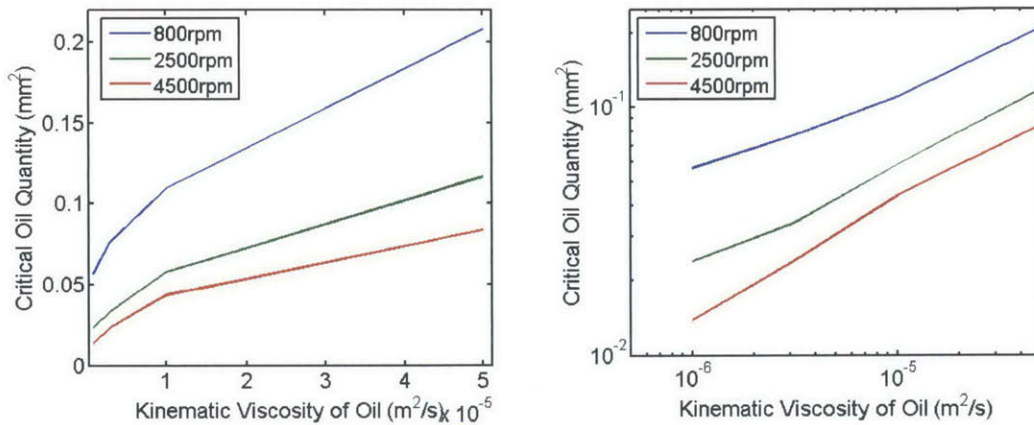


Figure 2.25 Critical oil quantity against oil viscosity. d = 0.5mm, with different N. (Left: normal scale; right: logarithmic scale)

The values of γ are listed in Table 2.3. It increases with engine speed and approaches to 0.5 at high speeds. This result will also be discussed in Section 2.5.2.

Table 2.3 Index of power law between critical oil quantity and oil viscosity

N (rpm)	800	2500	4500
γ	0.3321	0.4121	0.4616

Figure 2.26 demonstrates the effect of piston-liner clearance on critical oil quantity. Critical oil quantity increases with the clearance because oil spreading on a lower second ring flank takes a longer time in a larger clearance, making bridging less probable. Unfortunately, no quantitative correlations have been obtained.

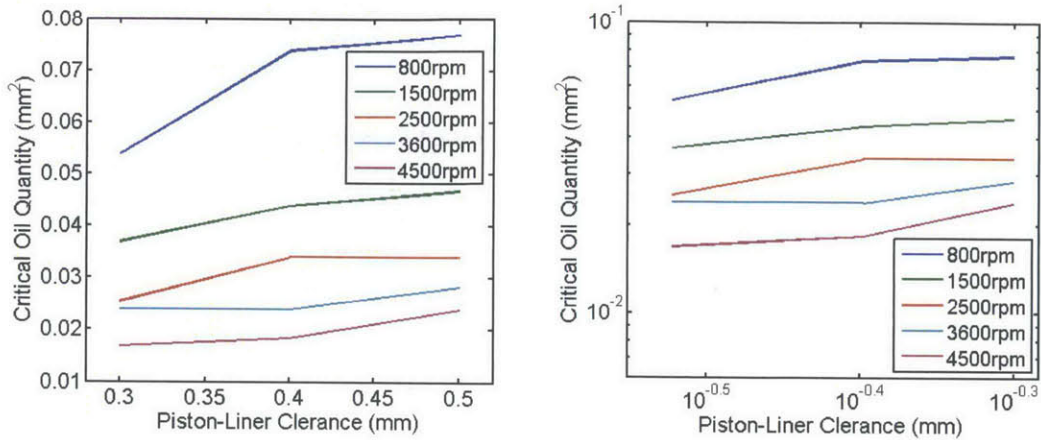


Figure 2.26 Critical oil quantity against clearance. $\nu = 3.125 \times 10^{-6} \text{ m}^2/\text{s}$, with different N . (Left: normal scale; right: logarithmic scale)

2.5.2 Discussions

This section presents an evaluation on the critical oil quantity predicted by computational simulations.

Since the piston-liner clearance is small compared to the axial height of piston third land, the effect of the spreading process is neglected. That is, it is assumed that the critical oil quantity is primarily determined by the oil rising process.

At a high engine speed, as discussed, the dimension of a puddle head is negligible. Thus, the rising process is dominantly governed by Equation (2.16), in which the transient term can be neglected:

$$-\frac{1}{\rho} \frac{\partial p}{\partial y} + \nu \frac{\partial^2 v}{\partial x^2} + a \approx 0 \quad (2.54)$$

The first term results from surface tension. It can be neglected at a high engine speed when both a and ν are large. It can also be neglected when oil viscosity is large. Thus, Equation (2.17) is more valid at a higher speed or with a higher oil viscosity.

Equation (2.17) gives the following scaling:

$$\nu \cdot \frac{V}{H^2} \sim a \propto N^2 \quad (2.55)$$

where V is the characteristic velocity, H is a rough scaling of oil film thickness, and N is engine speed. In a scenario when TDC bridging occurs:

$$V \sim \frac{L}{t_c} \propto LN \quad (2.56)$$

where L is the axial height of a piston third land, and t_c is the characteristic time. Combining (2.55) and (2.56), we get:

$$V_{\text{critical}} \sim HL \propto \sqrt{\frac{\nu L}{N}} \quad (2.57)$$

which basically indicates that the critical oil quantity is proportional to the square root of ν , and inverse proportional to the square root of N . This scaling is expected to be valid at a high engine speed or with a high oil viscosity. Given that axial piston height L is fixed in the simulations, this scaling analysis coincides with Table 2.1 and Table 2.3.

Specifically, Table 2.1 indicates that V_{critical} is asymptotically inverse proportional to the square root of N with a large ν , and Table 2.3 indicates that V_{critical} is asymptotically proportional to the square root of ν at a large N .

Up to this point, the simulation results have been justified.

2.6 Summary

In order to study the oil re-distribution process in a rectangular cavity near a piston third land, computational simulations in a radial cross section were conducted with OpenFOAM. The simulation results generally coincided with the experimental observations reported in [2], [4], [7], [11], which implied the validity of the computational results.

Simulations indicate that a re-distribution process can be divided into a few sub-processes. The complete process of a TDC bridging is described as follows. At the moment when the body acceleration switches direction from downwards to upwards, most oil is accumulated on an upper OCR flank. As the upward body acceleration increases, oil will first adjust its shape before a thin film flow is initialized on a piston third land. Then, oil rises along the piston land in the form of a slender puddle. After it reaches a lower second ring flank, it spreads along the lower second ring flank. If oil can reach a liner after spreading, it will be dragged by the liner and bridging occurs. As oil rises, a slight fraction of oil will keep residing on the upper OCR flank. There are two types of residual oil: circular residual oil and residual oil layer.

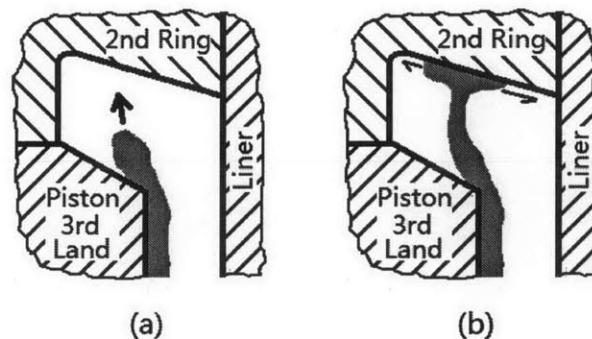


Figure 2.27 TDC bridging with a second ring hook and a chamfer on top of piston third land

Theoretical models on circular residual oil and oil spreading have been developed. The results coincide with simulations. A theoretical model on oil rising has shown discrepancies with simulations, which implies that a model on the initialization process is necessary.

A limitation of this study is that the effects of a Napier ring hook are not considered. When there is a hook in the second ring, the manner in which oil spreads on the lower second ring flank will be different. As will be explained in Chapter 3, in a high speed range where TDC bridging caused by an axial oil flow most probably occurs, oil will detach from a piston surface and “fly” towards the upper surface of a second ring hook. This is illustrated in Figure 2.27 (a). Then, oil will impact the upper surface of the hook and spread to all directions as illustrated in Figure 2.27 (b). In this case, the tapered angle of the hook is a critical design parameter. It determines the fraction of oil that spreads towards the liner. It also determines whether a component of body acceleration facilitates or resists TDC bridging.

The critical oil quantity, which is the least amount of oil with which TDC bridging occurs, has been estimated from the simulation results. Power laws with engine speed and oil viscosity have been found. The asymptotic power index of engine speed is -0.5 and that of oil viscosity is 0.5 . This has been justified by a scaling analysis.

Additional to the existing work on oil transport and bridging [7], [12], the effects of surface tension are explicitly considered in this work. It benefits from the multiphase solver which incorporates surface tension into computations. Both simulations and modeling results indicate that surface tension has more pronounced effects at lower engine speeds, when body acceleration is smaller. Although a few phenomena relevant to surface tension have been identified and understood, the initialization of a thin film flow, which is primarily governed by body acceleration and surface tension, remains to be modeled. It is a suggested topic for future research.

3 Oil Trapping in Second Ring Hook and Self-Sustained Bridging

In this chapter, a newly-discovered TDC bridging mechanism will be introduced. Based on the nature of this mechanism, it will be named “self-sustained bridging”. It is entirely distinct from the mechanism introduced in the forgoing chapters. Different from the bridging caused by an axial oil flow driven by a body force, self-sustained bridging more probably occurs at lower engine speeds.

A physical understanding of self-sustained bridging has been obtained from experiments and simulations. A theoretical model for low load conditions has been developed. A major objective of the modeling work is to prevent self-sustained bridging by optimizing the geometric design of a second ring hook and a piston chamfer.

3.1 Introduction

3.1.1 Motivation

In recent experiments conducted by Zanghi [10], a Napier ring together with a chamfer on top of piston third land were used. Contrary to the conclusion in Chapter 2 that TDC bridging caused by an axial oil flow more probably occurs at higher engine speeds, in these experiments, TDC bridging has been observed at 800rpm and 1500rpm, but not at higher speeds. If one extends the curve for “Hook + Chamfer” in Figure 2.1 [4], the critical oil quantity at 800rpm is roughly 35%. The fact that TDC bridging hardly occurs at higher speeds implies a proper functioning of the OCR. Thus, it is deemed improbable that oil supply to the vicinity of the piston third land exceeds the critical quantity at 800rpm or 1500rpm. As will be described shortly, experiments indicated that oil supply to the piston third land is indeed below the critical quantity. Thus, the reason why TDC bridging occurs at a low engine speed remains to be explained.

3.1.2 Observations in Experiments

Figure 3.1 shows two pictures taken from an experiment at 800rpm, 400mbar intake pressure. As explained, brighter parts indicate more oil. The light intensity in the picture can be read from the curves on the right.

Figure 3.1 (a) is a picture taken at 27° crank angle before TDC in a compression stroke. The vertical bright stripes enclosed by the white rectangle evidences bridging. On the boundary of the piston third land and the second ring, there is a horizontal bright stripe, which is labeled with “1”. It implies that a remarkable amount of oil exists in the second ring hook. There is a dark region labeled with “2” on the upper part of the piston third land, while the lower part appears brighter. It implies that the oil puddle on the piston land fails to reach the upper end. In other words, oil supply is below the critical quantity for bridging at 800rpm. Thus, the oil in the second ring hook is not supplied from the piston land, nor is the bridging oil. The experiment suggests that the oil accumulated in the second ring hook is the most probable source of bridging oil.

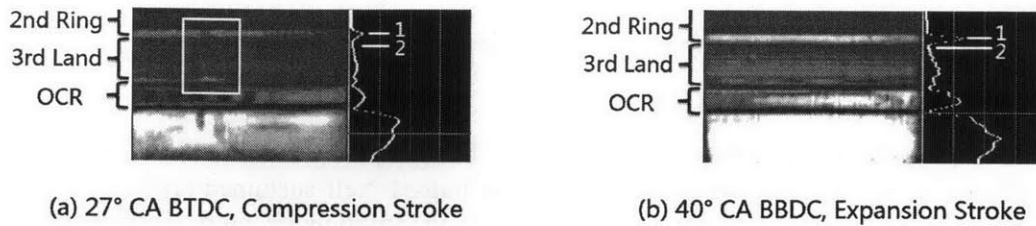


Figure 3.1 Bridging and oil trapping in second ring hook observed in experiment at 800rpm, 400mbar intake pressure. (Courtesy of E. Zanghi)

Figure 3.1 (b) shows the oil distribution at 40° crank angle before BDC in an expansion stroke. At this time, the body force is downward. However, the bright strike labeled with “1” and the dark region labeled with “2” implies that the oil stored in the second ring hook fails to flow downwards to the piston land. The oil in the second ring hook appears isolated from oil on the piston third land.

The experiments indicate that oil can be trapped in the second ring hook at a low engine speed. The quantity of trapped oil is remarkable. Given that it is not supplied from the piston third land, and that the second ring groove is not likely to supply this much oil, the trapped oil probably comes from the OCR gap. The oil leaking through an OCR gap will be scraped by a second ring and spread in the second ring hook. Because of the spreading of oil and the effect of blow-by [2], it is expected that the quantity of trapped oil varies in the circumferential direction. When the body force is upward, the trapped oil can flow upwards and bridge to the liner. This bridging mechanism is entirely different from that described in previous chapters. Oil does not circulate between the two ends of a piston third land. Instead, bridging oil flows in a smaller space near the liner and the second ring hook.

3.1.3 Observations in Simulations

In order to understand the physics behind bridging at low engine speeds, multi-phase simulations involving gas and oil flows were conducted. A second ring hook was included in the computational domain in order to study oil trapping in it. For the ease of meshing, a rectangular hook was studied. Two sets of simulations were conducted, one with a piston chamfer, one without it. The dimensions of the computational domains are shown in Figure 3.2. Still, simulations were conducted in a radial cross section. The piston is taken as the reference frame and the liner is moving. Since the computational domain is assumed perfectly sealed, the flow field is not affected by the pressure of blow-by gas. Thus, the simulations can only imply the oil transport at low load conditions, where gas pressure in the vicinity of a piston third land is almost uniform.

Each simulation started at TDC with a uniform oil layer along the piston land, and lasted for three revolutions. At each engine speed, the amount of oil doubles the critical quantity shown in Figure 2.23 to Figure 2.26. In all simulations, the oil distribution reached a realistic and periodical pattern within two revolutions. The results in the third revolution will be shown.

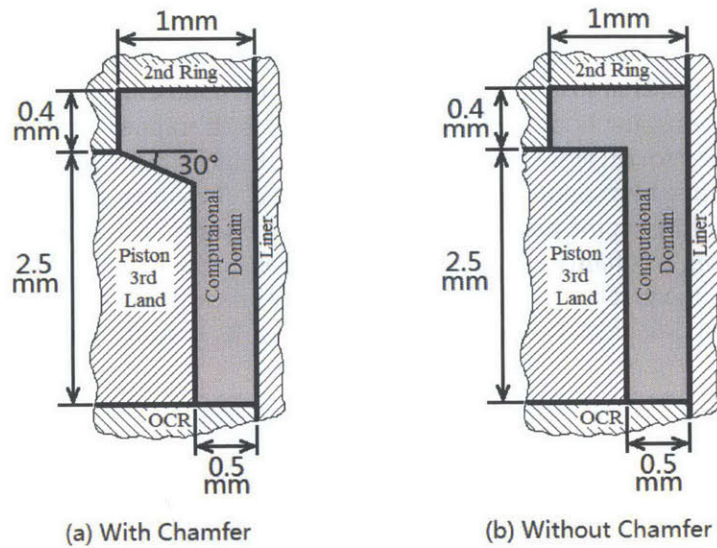


Figure 3.2 Computational domains for OpenFOAM simulations

Figure 3.3 demonstrates the oil distribution at 159.2° crank angle ATDC, when the downward body acceleration reaches a maximum. At 800rpm, a considerable amount of oil is trapped in the second ring hook and piston chamfer. As engine speed increases, the quantity of oil that stays in the hook significantly decreases. At above 1500 rpm, oil can only stay in the second ring hook in the form of residual oil, including circular residual oil in corners and residual oil layer on the upper surface of the second ring hook.

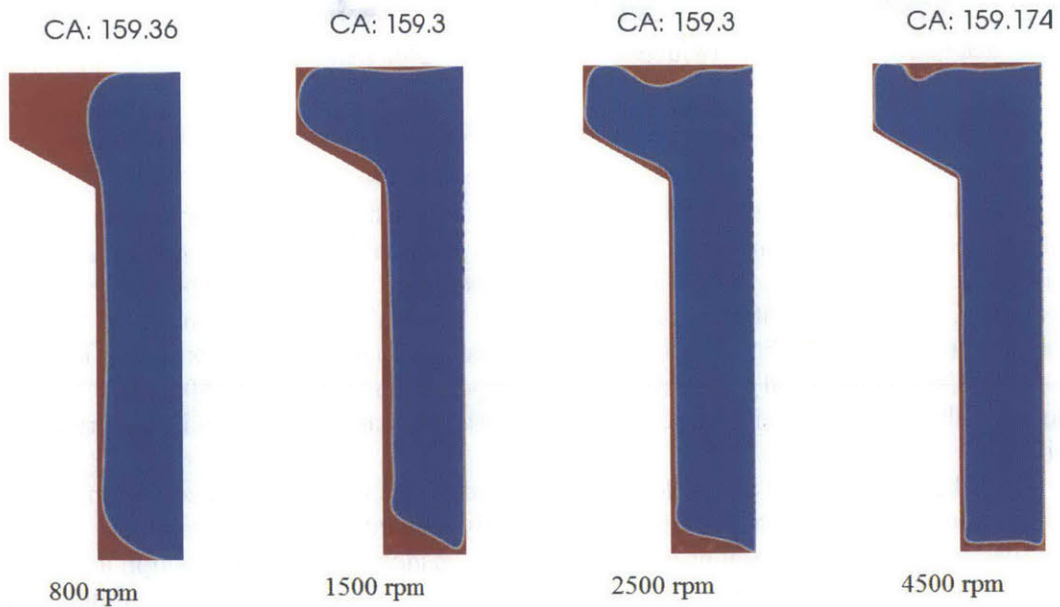


Figure 3.3 Oil trapping in a rectangular hook with a piston chamfer (Red: oil; blue: gas)

Bridging occurs in all the four simulations shown in Figure 3.3. As shown in Figure 3.4 leftmost, when bridging occurs at 800rpm, the upper leading edge of the oil puddle on the piston land just arrived at the top. The oil puddle has not connected to the trapped oil yet. Thus, the bridging oil entirely comes from trapped oil, which flows upward upon body force. However, above 1500rpm, trapped oil is not sufficient to trigger bridging and oil must be supplied from the piston land. As shown in Figure 3.4, at over 1500rpm, the oil film on the piston connects to the trapped oil when bridging occurs. While the bridging mechanism observed at high speeds is identical with that described in Chapter 1 and 2, the mechanism at a low speed is entirely different. However, the low speed mechanism coincides with the experimental results described in Section 3.1.2.

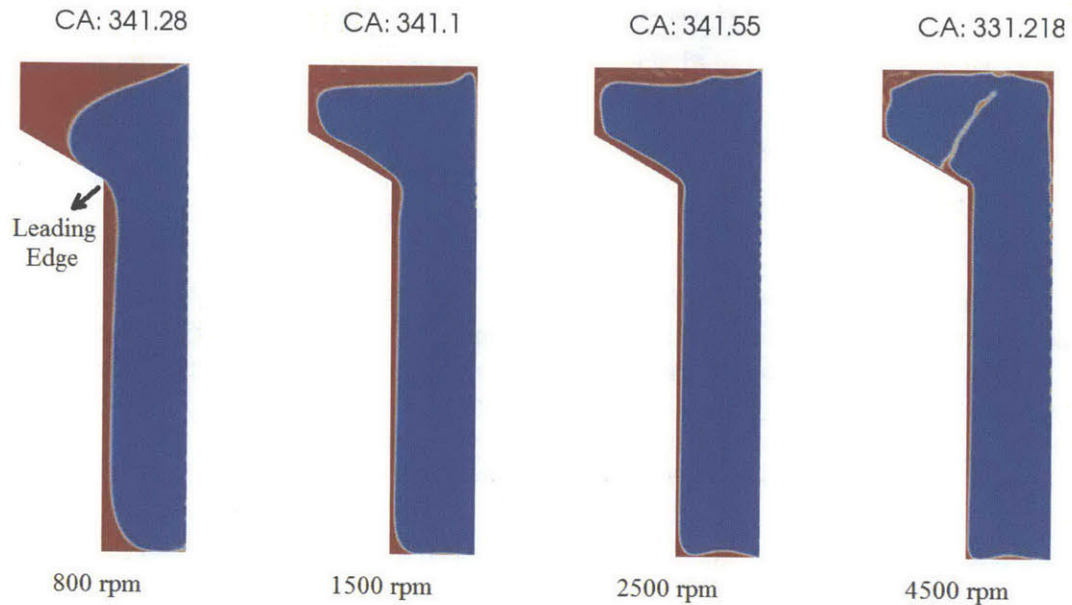


Figure 3.4 Bridging in a rectangular hook with a piston chamfer (Red: oil; blue: gas)

Figure 3.5 shows the oil distribution without a piston chamfer. At 800rpm, oil is trapped but trapped oil cannot arouse bridging. Additional oil must be supplied from the piston third land. It indicates that trapped oil does not necessarily cause bridging. However, because of the trapped oil, oil from the piston third land need not flow through the detour as shown in Figure 3.6 left. It only floats through a shortcut as shown in Figure 3.5 left. Thus, trapped oil also facilitates bridging in this scenario. At 1500rpm, considerable amount of oil can be trapped and bridging can be sustained by the trapped oil.

The simulation results at low engine speeds coincide with the observations in experiments. Although trapped oil can be partially drained to the piston land in simulations, the fundamental bridging mechanism is identical: oil is trapped in a second ring hook and trapped oil bridges to a liner. When the quantity of oil in the computational domain decreases, trapped oil can be isolated with oil on the piston third land. This is entirely identical to the experimental results. The difference between two sets of

simulations indicates that the geometric design of the hook and the chamfer can make a difference.

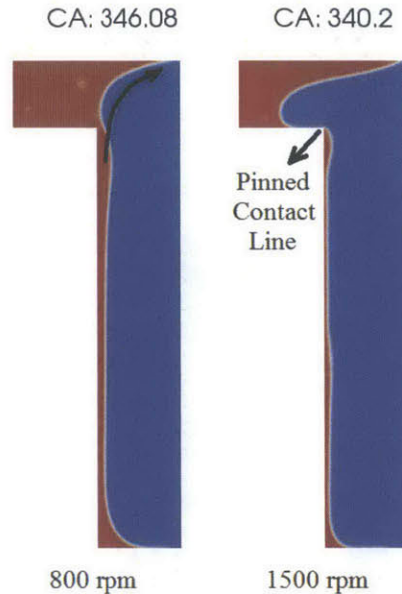


Figure 3.5 Oil distribution in a rectangular hook without a piston chamfer (Red: oil; blue: gas)

3.1.4 Bridging Mechanisms

In this section, a few bridging mechanisms will be summarized. They are probable in different speed ranges because of the different physics behind.

Both experiments and simulations demonstrated that TDC bridging at low engine speeds results from oil trapped in the second ring hook. Based on the fact that trapped oil can sustain bridging without additional oil supply from a piston land, this mechanism is named “self-sustained bridging”. For simplicity, it will be called SS bridging in the remaining of this report.

In the simulations, the bridging mechanism described in Chapter 1 and 2 have also been observed. Based on the fact that oil on a piston land must reach a hook to assist the bridging process, it is named “assisted bridging”.

Experiments and simulations indicate that SS bridging is probable at low engine speeds. Previous studies [2], [4], [6] have shown that assisted bridging is probable at high engine speeds. However, these two mechanisms are not exclusive. Though not probable, they may occur in a same condition. For instance, in some simulations, oil on the piston land rises so fast that assisted bridging occurs before SS bridging could possibly occur. Though trapped oil is able to arouse SS bridging, it cannot be observed. However, this scenario occurs only when a redundant amount of oil exists on a third land, which is not probable in real engine operations.

The simulations shown in Section 3.1.3 also demonstrate how oil enters a second ring hook when assisted bridging occurs.

When the engine speed is low and/or the oil thickness on a piston land is small, the manner in which oil enters a second ring hook depends on whether the rising oil can connect with the trapped oil. If so, the supplied oil will float on the free surface of the trapped oil before bridging. This is illustrated in Figure 3.5 left; if not, the leading contact line would be “pinned” at the top edge of the piston land and rising oil cannot proceed into the hook. This is illustrated in Figure 3.5 right. The contact line is “pinned” because inertial force and body force fail to overcome surface tension.

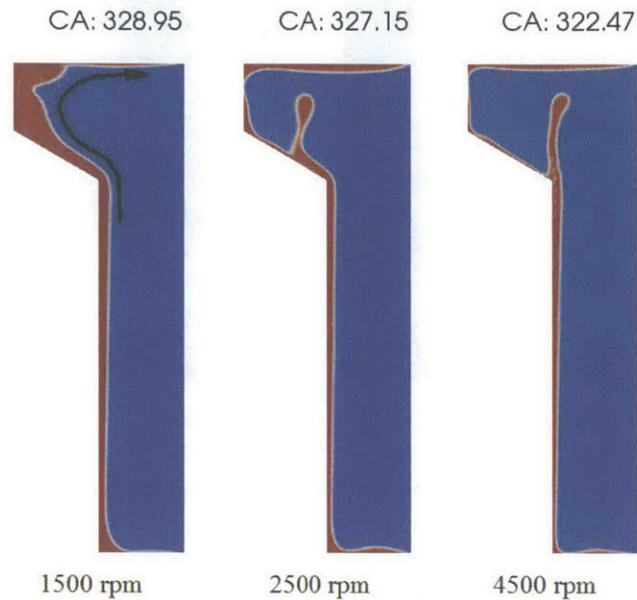


Figure 3.6 Oil supply from piston third land to second ring hook (Red: oil; blue: gas)

At medium speeds, only a little oil is trapped. Thus, rising oil cannot float in the manner shown in Figure 3.5 left. Inertial force and body force are large enough to overcome the “pinning” effect. Thus, oil can enter a hook if it can reach the top of a piston third land. Under the effect of surface tension, oil sticks to the solid boundary and crawls through a detour before bridging. This detour is illustrated in Figure 3.6 left. It is deemed that bridging is the least probable in this condition.

When the engine speed is high and/or the oil thickness on a piston land is large, inertial force and body force overwhelms surface tension and oil can “fly” away from the solid boundary. At 2500rpm (Figure 3.6 middle), oil flies away halfway in the detour. At 4500 (Figure 3.6 right), oil can fly away immediately after it reaches the top of a piston land. The flying oil hits the upper surface of a hook and spreads out before bridging.

The TDC bridging mechanisms are summarized schematically in Figure 3.7.

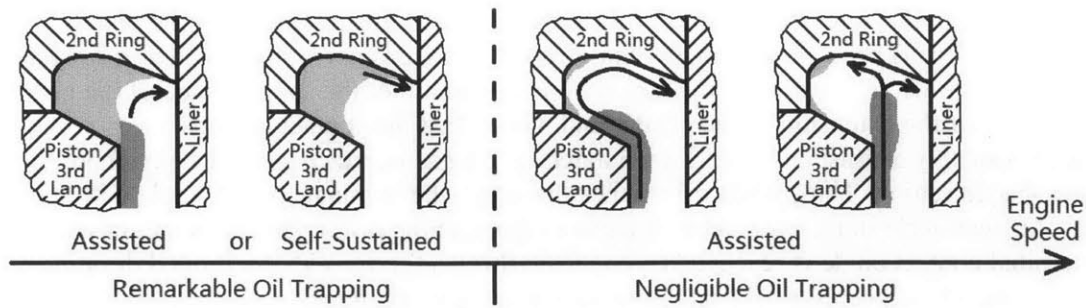


Figure 3.7 Schematic diagram of TDC bridging with a second ring chamfer

3.1.5 Structure of This Chapter

This chapter is focused on SS bridging. The interaction between trapped oil and oil film on a piston land will not be considered in this chapter. That is, bridging is sustained entirely by trapped oil.

In Section 3.2, oil trapping, which is a prerequisite of SS bridging, will be introduced. The physics behind it will be explained and a theoretical model will be described. In Section 3.3, a theoretical model of SS bridging will be described. Strategies for avoiding SS bridging will be discussed based on modeling results. In Section 3.4, the accuracy of the modeling results will be discussed. A brief summary of this Chapter will be presented in Section 3.5.

3.2 Oil Trapping in Second Ring Hook

In terms of oil consumption, oil trapping is deemed a detrimental phenomenon. As introduced, trapped oil can cause TDC bridging, which can potentially increase oil consumption. Besides, it also constitutes an oil reservoir for the second ring groove, which also potentially contributes to oil consumption. Thus, it is of significance to understand when oil trapping occurs, and how much oil can be trapped.

In this section, the physics behind oil trapping will first be explained. Then, a heuristic analysis will be presented to explain why it occurs at low engine speeds. Finally, a theoretical model will be introduced and modeling results will be presented.

3.2.1 Physics behind Oil Trapping

Figure 3.8 demonstrates the oil distribution and pressure field at 159.3° crank angle. The white curve signifies the oil-gas interface, and the colors signify pressure. The pressure in the gas is roughly 100000Pa. As can be observed, the thickness of oil film is small at the upper edge of the piston third land. As explained in Chapter 2, oil velocity is small in a thin oil film. Thus, oil in the second ring hook can hardly be drained to the third land, which results in oil trapping. On the other hand, if there is less oil in this space, oil in the second ring may not be connected with the oil on the piston land. In this case,

the lower contact line of the trapped oil can be pinned at the outer edge of the piston chamfer. This is because the tangent line of solid surface is not well defined at the sharp edge. As shown in Figure 3.9, the tangent line can be either the solid surface of the piston chamfer, or the extension of the piston land. Given that the contact angle is approximately a constant value β , the tangent of oil-gas interface can exist anywhere in the shaded region. Thus, when oil reaches this edge, the nominal contact angle with the piston chamfer will increase. The oil cannot escape to the piston land until the maximum nominal contact angle is reached. To conclude this paragraph, either a limited draining or a pinning effect prevents oil from escaping the second ring hook.

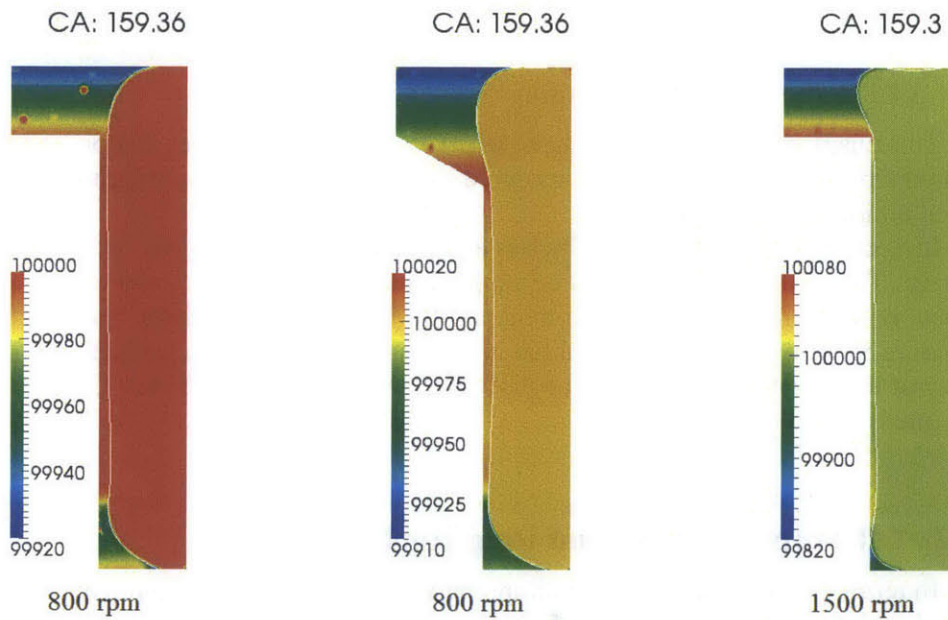


Figure 3.8 Pressure fields in trapped oil. (Pressure in Pa. Gas pressure is 100000Pa.)

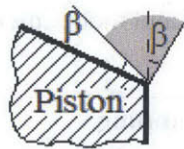


Figure 3.9 “Pinning” of oil contact line at the outer edge of piston chamfer

If oil can be trapped in a second ring hook when body force is downward, there must be an upward force to balance the body force. As demonstrated in Figure 3.8, simulations indicate that the pressure field in the trapped oil is approximately hydrostatic.

(The spots in Figure 3.8 result from entrained gas bubbles) The pressure difference across the trapped oil approximately equals to $\rho a(\Delta d)$, where Δd is height of the trapped oil. It indicates that the upward pressure force is the dominant force that balances the downward body force. Apart from body force, three forces are in effect: inertial force, viscous force, and surface tension. Since the velocity in the trapped oil is small, it is not probable that the former two could have a remarkable effect. Thus, the surface tension is the primary cause of such a pressure gradient. By adjusting the profile of the oil-gas interface, Laplace pressure can result in a balancing pressure field.

Up to this point, it has been explained why oil can be trapped in a second ring hook. First, oil in a hook is prevented from escaping near the outer edge of a piston chamfer. Second, surface tension can generate a pressure field that balances a downward body force.

3.2.2 A Theoretical Definition of Oil Trapping

Figure 3.3 indicates that oil can be trapped in a second ring hook at all engine speeds. It is only a matter of quantity. At low engine speeds, the interface connects the upper surface of the hook and the piston chamfer, as illustrated in Figure 3.10 left. At high engine speeds, oil can only be trapped in the form of residual oil, as illustrated in Figure 3.10 right. In the latter case, the quantity of trapped oil is very small and may not be sufficient to support SS bridging. Hence, in the model to be presented, only the former scenario will be considered.

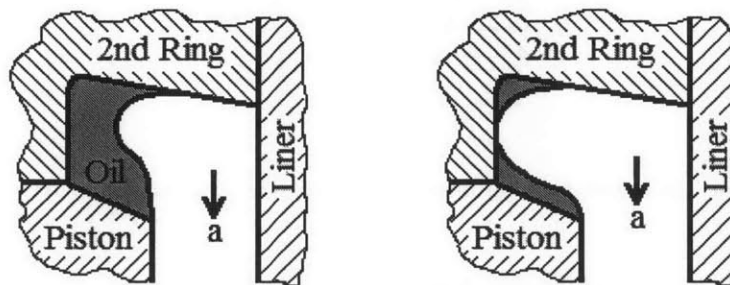


Figure 3.10 Schematic diagram of oil trapped in second ring hook (Left: low speed; Right: high speed)

That is to say, the definition of “oil trapping” in this work is: a continuous oil-gas interface connecting a piston chamfer and the upper surface of a second ring hook can be maintained under the maximum downward acceleration at a certain engine speed.

Based on this definition, a critical engine speed, as labeled by the dashed line in Figure 3.7, can be expected. Above the critical speed, oil trapping does not occur; below the critical speed, oil trapping occurs. This critical speed is of significant interest. If it is below the idle speed of an engine, oil trapping, as well as self-sustained bridging, can be entirely avoided in engine operations. As explained in Section 3.1.3, this critical speed

essentially depends on the geometric design of a hook region, including a second ring hook and a piston chamfer. Thus, it is of great significance to study the effects of different design features of typical hook regions.

3.2.3 A Heuristic Analysis

In this section, a mathematical analysis on a simplistic design will be presented. The objective is to obtain a physical understanding on oil trapping and explain why it occurs at low engine speeds.

In this heuristic analysis, a rectangular hook with a conforming piston chamfer will be considered. The dynamic effects will be neglected. This means: 1) inertial forces and viscous forces will be neglected; 2) the oil-gas interface profile will respond to a body force field in a negligible duration of time. Thus, the oil-gas interface profile is determined by the quasi-static balance between surface tension and body force. As explained in Section 3.2.1, this is the primary force balance in trapped oil. In all the following analysis, the gas pressure is assumed uniformly zero. The coordinate system and geometric parameters are shown in Figure 3.11.

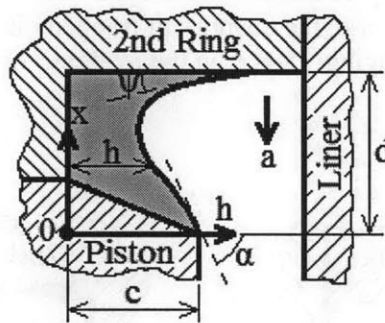


Figure 3.11 Coordinate system and geometric parameters in the heuristic analysis (Not to scale)

3.2.3.1 Critical Engine Speed

According to Section 3.2.2, when oil trapping occurs, a continuous oil-gas interface must exist all through the hook region. Thus, the profile of oil-gas interface must be analyzed in order to understand oil trapping. The conditions in which a continuous interface can exist determine when oil trapping can possibly occur.

This analysis on oil-gas interface is similar to that presented in Section 2.4.2. By equating hydrostatic pressure and Laplace pressure, we get an equation for the profile of the oil-gas interface:

$$p_0 - \rho ax = \sigma \cdot \frac{-h_{xx}}{(1 + h_x^2)^{2/3}} \quad (3.1)$$

where p_0 is oil pressure at $x = 0$, ρ is oil density, x is the vertical coordinate shown in Figure 3.11, σ is surface tension of oil and gas, and h is oil thickness as shown in Figure

3.11. Subscript x denotes the derivative with respect to x . a is the maximum downward body acceleration which can be calculated with Equation (1.1). Equation (3.1) is a second-order ordinary differential equation with one unknown parameter. Three constraints, including two boundary conditions and one additional limiting condition, are needed to solve it. However, the contact angles on the upper and the lower solid surfaces provide only two constraints:

$$h_x(x = 0) = -\cot \alpha \quad (3.2)$$

$$h_x(x = d) = \cot \psi \quad (3.3)$$

where α is the limiting angle of the lower contact line, and ψ is the contact angle on the upper solid surface (Figure 3.11). Thus, the interface profile is not unique at a same engine speed. It also depends on the amount of oil that is trapped in the hook. However, to determine the oil supply to a hook region can be complicated. It can involve an analysis on several other components, which is beyond the scope of this work. For simplicity, in this work, the maximum amount of oil that can be trapped at a certain engine speed is of the most significant interest. It measures the trapping capability of a second ring hook. Thus, it is assumed that the lower contact line of the interface is located at the outer edge of a piston chamfer. That is:

$$h(x = 0) = c \quad (3.4)$$

where c is the depth of second ring hook as shown in Figure 3.11. Equation (3.4) constitutes a third constraining condition for Equation (3.1).

Integrating Equation (3.1) once with constraining condition (3.2), we get:

$$\frac{-h_x}{(1 + h_x^2)^{1/2}} = -\frac{\rho a}{2\sigma} x^2 + \frac{p_0}{\sigma} x + \cos \alpha \quad (3.5)$$

Plug Equation (3.3) into (3.5), we get:

$$p_0 = \frac{\rho a}{2} \cdot d - \frac{\sigma(\cos \psi + \cos \alpha)}{d} \quad (3.6)$$

where d is the height of a hook region, including a hook and a chamfer. Here, ψ is a receding contact angle, which may not be a constant. The limiting angle α can vary in a larger range as explained in Section 3.2.1. Fortunately, as will be shown later, neither of them significantly affects the modeling result. Thus, ψ and α are assumed constant in the following analysis.

Equation (3.6) indicates that p_0 increases with d and engine speed. A more straightforward description is as follows. The pressure difference all across a hook region, including a hook and a chamfer, is $p_0 - p_d = \rho a d$, where p_0 denotes the oil pressure at $x = 0$, and p_d denotes the oil pressure at $x = d$. The pressure difference increases with d and engine speed. Thus, with a larger d or at a higher engine speed, p_0 must increase to facilitate the larger pressure difference. Similarly, p_d should decrease with d and engine speed, which is generally true, though not always.

However, the left hand side of Equation (3.5) must fall between -1 and 1. Thus, the right hand side must not exceed 1 when $0 \leq x \leq d$. This requires:

$$p_0 \leq \sqrt{2\rho a \sigma (1 - \cos \alpha)} \quad (3.7)$$

That is, p_0 cannot increase indefinitely. Physically, the point at which $h_x = -\infty$ is a critical point, if it exists. The pressure at this critical point, p_c , must be non-negative when oil is trapped. Otherwise, according to the Young-Laplace Equation:

$$p_{oil} - p_{pas} = p_{oil} = \frac{\sigma}{R} \quad (3.8)$$

the local radius of oil-gas interface at the critical point must be positive and the interface must curve back toward the piston chamfer, as illustrated with the solid curve in Figure 3.12. Thus, the interface fails to connect the upper surface of a second ring hook, and oil trapping defined in Section 3.2.2 is not possible.

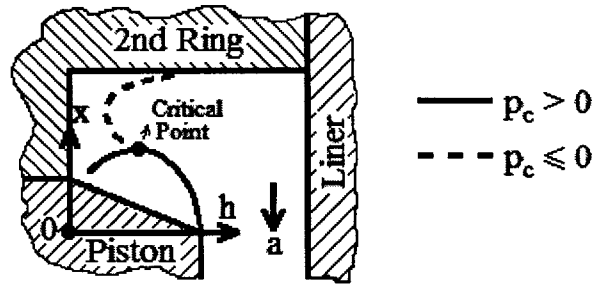


Figure 3.12 Evolution of interface profile at the critical point

According to the Young-Laplace Equation, a large p_0 requires a small radius R_0 in the interface. Since $p_c \sim p_0 - \rho a R_0$, p_c increases with p_0 . Then, because p_c cannot be greater than 0, p_0 cannot be greater than a critical value. This explains Inequality (3.7) from a physical perspective.

Since p_0 increases with engine speed, the engine speed cannot exceed a critical value, either. This explains why oil trapping occurs at low engine speeds only. Equation (3.6) and Inequality (3.7) gives:

$$a \leq \frac{2}{\rho d} \left(\frac{\sigma(\cos \psi + \cos \alpha)}{d} + \sqrt{2\rho a \sigma (1 - \cos \alpha)} \right) \quad (3.9)$$

For a given design, the right hand side of (3.9) can give the critical speed for oil trapping. The critical speed decreases with d . Given that the design objective is to decrease the critical speed to below the idle speed, increasing d constitutes an effective approach to preventing oil trapping.

The heuristic analysis indicates that there are physical constraints on p_0 , which is the oil pressure on the bottom of trapped oil. The constraints on p_0 determine whether the governing equation for oil-gas interface, which is Equation (3.5) in this analysis, has a solution that satisfies the definition in Section 3.2.2. The constraints on p_0 are also directly associated with the critical engine speed for oil trapping.

3.2.3.2 Trapping Capability

By continuing the analysis on the oil-gas interface profile, the variation of trapping capability with engine speed can be understood.

The first derivative of h with respect to x can be obtained from Equation (3.5). By integrating h_x with constraining condition (3.4), we get:

$$h(x) = c - \int_0^x \frac{F}{\sqrt{1-F^2}} dx \quad (3.10)$$

where:

$$F = -\frac{\rho a}{2\sigma} x^2 + \left(\frac{\rho a}{2\sigma} \cdot d - \frac{\cos \psi + \cos \alpha}{d} \right) x + \cos \alpha \quad (3.11)$$

It can be shown that:

$$\frac{\partial h}{\partial a} = \frac{\rho}{2\sigma} \int_0^x \frac{1}{(1-F^2)^{\frac{3}{2}}} \cdot x(x-d) dx < 0 \quad (3.12)$$

That is, in a given design, oil thickness h decreases with engine speed. Hence, the volume of oil that can be trapped decreases with engine speed. This also explains why oil trapping is more pronounced at lower engine speeds.

As engine speed increases, h decreases. That is, the oil-gas interface approaches the inner solid boundary. When it touches the inner boundary, it cannot connect the upper solid boundary and the lower solid boundary with a continuous profile. Thus, oil trapping is suppressed. The suppression occurs at a lower engine speed if c (as defined in Figure 3.11) is smaller. Therefore, decreasing c is an auxiliary approach to avoiding oil trapping. However, this approach may sacrifice the functioning of a second ring hook at a high engine speed, since the hook provides a smaller buffer for oil supplied from a third land.

3.2.3.3 Effect of Tapered Napier Ring Hook

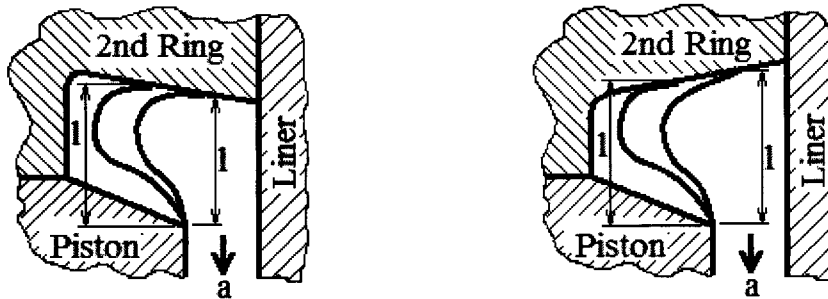


Figure 3.13 Geometry of tapered Napier ring hook (Left: positive angle; right: negative angle)

If a second ring hook is tapered with a positive angle as illustrated in Figure 3.13 left, the height of an oil interface (l) is not constant. When engine speed increases, p_0 increases and the oil interface approaches to the inner boundary. Because of the tapered angle, l effectively increases. Since $p_0 - p_1 = \rho a l$, the pressure difference further increases with engine speed, and p_0 must increase further to facilitate the larger difference. Thus, p_0 increases more rapidly with engine speed. As a result, the critical speed decreases with a positive tapered angle.

However, it is noted that p_0 may also decrease with engine speed with a positive tapered angle. If p_0 decreases, h will increase, which leads to a smaller l . The maximum pressure difference $p_0 - p_1 = \rho a l$ can possibly decrease, which requires a decreased p_0 . Thus, it is not contradictory if p_0 decreases with engine speed. As demonstrated in Figure 3.14, the oil-gas interface can indeed vary in this manner when the engine speed is close to the critical value. However, for most engine speeds below the critical speed, the interface approaches to the inner boundary as engine speed increases.

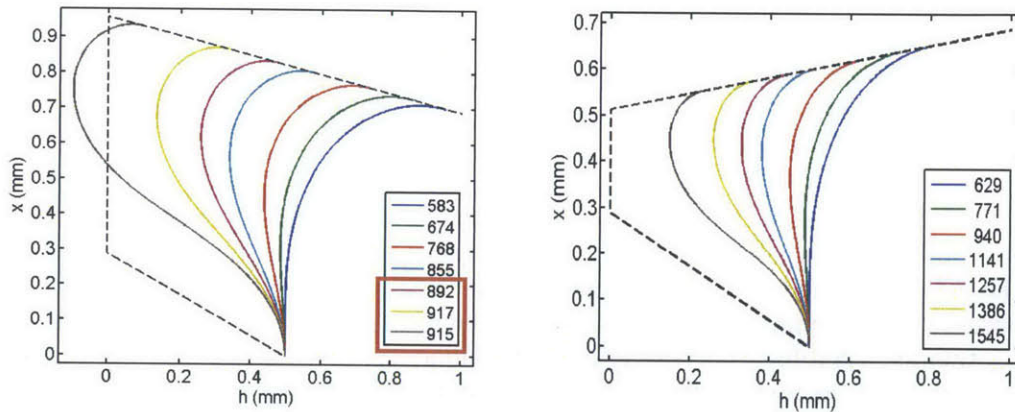


Figure 3.14 Oil-gas interface profiles in Napier ring hooks at different engine speeds (Left: $+15^\circ$ tapered angle; right: -10° tapered angle; legend: engine speed in rpm)

In a hook tapered with a negative angle as illustrated in Figure 3.13 right, when engine speed increases, p_0 increases and h decreases. The decrease in h is accompanied by a decrease in l . Although $p_0 - p_1 = \rho a l$ can still increase, it increases more slowly with engine speed, so does p_0 . Thus, p_0 will reach its critical value at a larger engine speed, and the critical engine speed for trapping increases. It can be shown that the oil-gas interface cannot vary in the opposite manner with a negative tapered angle.

The analysis in this Section indicates that the critical engine speed for oil trapping decreases with a tapered angle. A positive angle suppresses oil trapping and a negative angle favors oil trapping. Thus, an effective approach to decrease the critical speed is to increase the tapered angle in a Napier ring hook

3.2.4 A Theoretical Model of Oil Trapping

In this Section, the analysis presented in Section 3.2.3 will be conducted in a more quantitative manner. Based on the quantitative analysis, a theoretical model has been developed. With a geometric design given, the model can predict the critical engine speed for oil trapping and trapping capability at a given engine speed.

3.2.4.1 Geometry of Second Ring Hook and Piston Chamfer

In fact, a piston chamfer can conform to a hook (Figure 3.15 left), be smaller than a hook (Figure 3.15 right), or be larger than a hook (Figure 3.15 right). The last design is not considered as a good design because the grey wedge constitutes an oil reservoir for the second ring groove, which potentially increases oil consumption. Thus, in this work, only the first two cases will be considered.

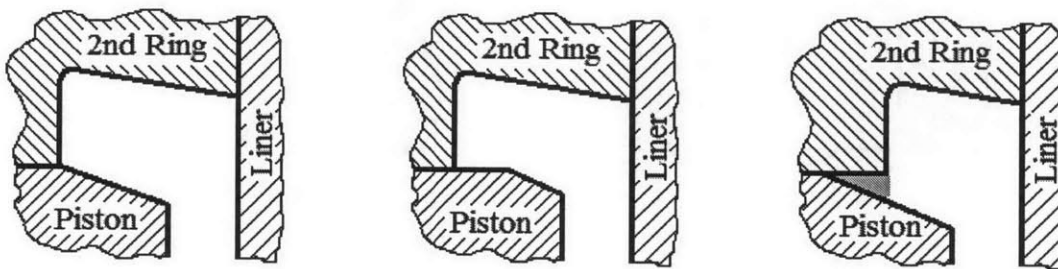


Figure 3.15 Conformation of piston chamfer to second ring hook

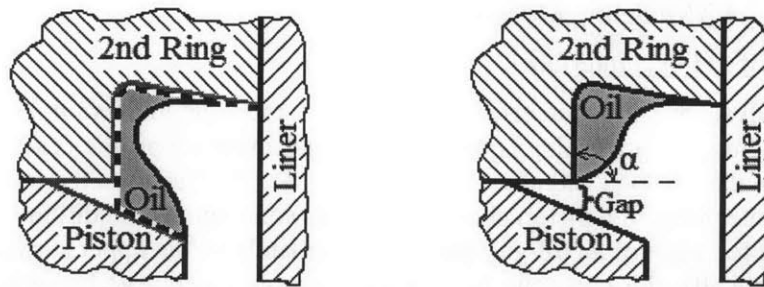


Figure 3.16 Pinning of oil contact line if piston chamfer is larger than second ring hook

Actually, the modeling method in this work can be directly applied to the last design. In this geometry, the lower contact line can be pinned at either the outer edge of the piston chamfer (Figure 3.16 left), or the lower edge of the second ring hook (Figure 3.16 right). The former scenario can be analyzed by neglecting the wedge, as shown by the dashed line in Figure 3.16 left. The latter scenario can be analyzed by applying different constraining conditions to the same governing equation. However, such a

geometry will not be specially considered in this work. Actually, it can be shown that the critical trapping speed for the second trapping mode (Figure 3.16 right) is higher with a same second ring hook. It constitutes another reason why a large piston chamfer is an undesirable design.

Two classes of geometric parameters are incorporated in the model: 1) geometry of the second ring hook and the piston chamfer, as shown in Figure 3.17 left. The parameters include: height of hook region d , tapered angle of hook γ , width of hook w , radius of hook fillet R , depth of hook region c , height of chamfer s , and chamfer angle θ ; 2) contact angles as shown in Figure 3.17 right. Two contact angles are relevant: the receding contact angle on the upper hook surface, and the limiting angle on the outer edge of the piston chamfer.

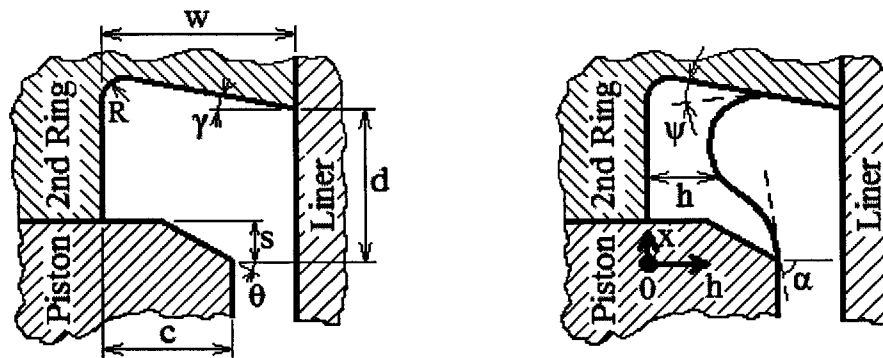


Figure 3.17 Geometric parameters in the model for trapping

3.2.4.2 Modeling Method

Profile of Oil-Gas Interface

The analysis on oil-gas interface follows the same logic in Section 3.2.3. For a tapered Napier ring, the governing equation for oil-gas interface profile is still Equation (3.5), and Inequality (3.7) is still a constraint on p_0 . The lower edge of the interface is still pinned at the outer edge of a piston chamfer. That is, constraining condition (3.4) is still applicable. The top edge of an oil-gas interface must land on the upper surface of the hook. Mathematically, this constraining condition is more complicated than Equation (3.3). It will be shown that this constraining condition actually links the constraints on p_0 to the critical engine speed for oil trapping.

If the tapered hook angle γ is greater than the receding contact angle ψ , h is a multi-valued function of x . The hydrostatic pressure field implies a symmetric interface profile about a vertical line through the apex of an interface (Figure 3.18 left). Only the left half of the interface is to be functionalized. Here, x_e is the location of the interface apex, and x_s is the location of the contact line. They are specified by:

$$h_x|_{x=x_s} = \cot(\gamma - \psi) \quad (3.13)$$

$$h_x|_{x=x_e} \rightarrow +\infty \quad (3.14)$$

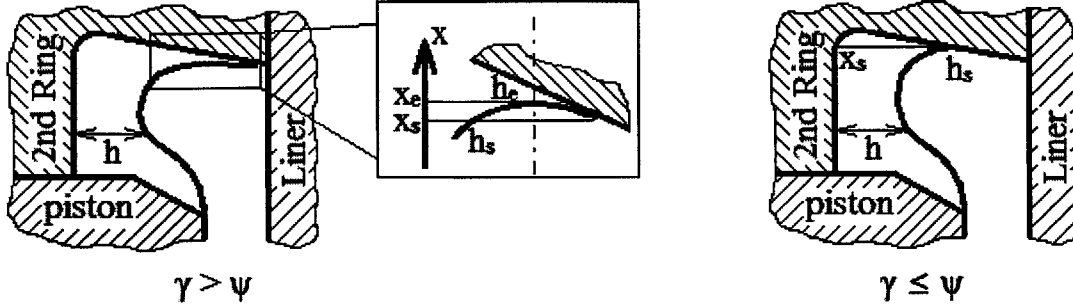


Figure 3.18 Boundary condition on top of interface

Plugging (3.13) and (3.14) into (3.5), we get:

$$x_s = \frac{p_0 + \sqrt{p_0^2 + 2\rho a \sigma (\cos \alpha + \cos(\gamma - \psi))}}{\rho a} \quad (3.15)$$

$$x_e = \frac{p_0 + \sqrt{p_0^2 + 2\rho a \sigma (\cos \alpha + 1)}}{\rho a} \quad (3.16)$$

The upper edge of the interface coincides with the solid boundary. Hence:

$$h_e + (h_e - h_s) = w - (x_s - d) \cdot \cot \gamma \quad (3.17)$$

where w and d are defined in Figure 3.17, and:

$$h_s = c + \int_0^{x_s} h_x dx = c - \int_0^{x_s} \frac{F}{\sqrt{1 - F^2}} dx \quad (3.18)$$

$$h_e = c + \int_0^{x_e} h_x dx = c - \int_0^{x_e} \frac{F}{\sqrt{1 - F^2}} dx \quad (3.19)$$

where F is the right hand side of Equation (3.5). It must be noted that F cannot be obtained by Equation (3.11) for a tapered ring hook. When $\gamma > \psi$, Equation (3.17) is the constraining condition on the top edge of an oil-gas interface.

If $\gamma \leq \psi$, h is a single-valued function of x all along an interface. As defined in Figure 3.18 right, the location of the contact line x_s is specified by:

$$h_x|_{x=x_s} = \cot(\psi - \gamma) \quad (3.20)$$

Plugging Equation (3.20) into Equation (3.5), we get an identical equation with (3.15) because cosine function is even.

When $\gamma \leq \psi$, the constraining condition on the top of an oil-gas interface is:

$$h_s = w - (x_s - d) \cdot \cot \gamma \quad (3.21)$$

where h_s is given by Equation (3.18), and x_s is given by Equation (3.15).

For simplicity, three dimensionless groups are introduced:

$$\eta = x \cdot \sqrt{\frac{\rho a}{2\sigma}} \quad (3.22)$$

$$\xi = p_0 \cdot \sqrt{\frac{2}{\rho a \sigma}} \quad (3.23)$$

$$k = d \cdot \sqrt{\frac{\rho a}{\sigma}} \quad (3.24)$$

Then, Equation (3.15) and (3.16) become:

$$\eta_s = \frac{1}{2} \left(\xi + \sqrt{\xi^2 + 4(\cos \alpha + \cos(\gamma - \psi))} \right) \quad (3.25)$$

$$\eta_e = \frac{1}{2} \left(\xi + \sqrt{\xi^2 + 4(\cos \alpha + 1)} \right) \quad (3.26)$$

Combining constraining conditions (3.17) and (3.21), after some algebra, we get:

$$\frac{1}{\sqrt{2}} \cdot k \cdot \frac{D}{d} = B(\xi, \gamma, \alpha, |\gamma - \psi|) \quad (3.27)$$

where

$$B = \begin{cases} -2 \int_0^{\eta_e} \frac{F}{\sqrt{1-F^2}} d\eta + \int_0^{\eta_s} \frac{F}{\sqrt{1-F^2}} d\eta + \eta_s \cdot \cot \gamma & (\gamma > \psi) \\ - \int_0^{\eta_s} \frac{F}{\sqrt{1-F^2}} d\eta + \eta_s \cdot \cot \gamma & (\gamma \leq \psi) \end{cases} \quad (3.28)$$

$$F(\eta) = \frac{-h_x}{(1 + h_x^2)^{1/2}} = -\eta^2 + \xi\eta + \cos \alpha \quad (3.29)$$

and:

$$D = w - c + d \cdot \cot \gamma \quad (3.30)$$

The next step is to establish a correlation between the constraints on p_0 and the critical engine speed for oil trapping. One constraint on p_0 is Inequality (3.7). It requires:

$$\xi \leq 2\sqrt{1 - \cos \alpha} \quad (3.31)$$

Simulations indicate that the local radius of an interface at $x = 0$ is positive. Thus, the Young-Laplace Equation gives that $p_0 > 0$ and $\xi > 0$. Figure 3.19 shows the figure of B as a function of ξ in the domain $(0, 2\sqrt{1 - \cos \alpha})$. It is evaluated numerically with Simpson's Rule with 2001 grids. For each value of α , B has a maximum value B_{\max} . The maximum value is a function of γ , α , and $|\gamma - \psi|$. Thus, Equation (3.27) requires that:

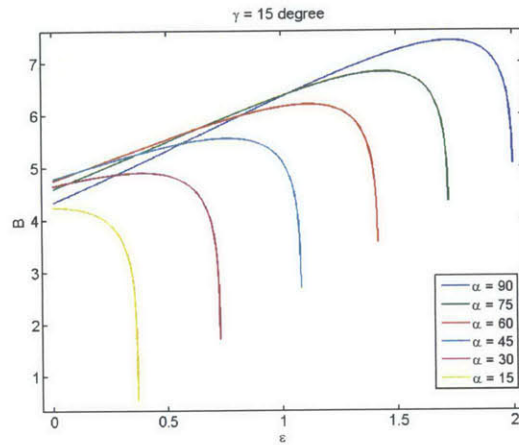


Figure 3.19 B as a function of ξ . ($\gamma = 15^\circ$, $\psi = 0^\circ$)

$$\frac{1}{\sqrt{2}} \cdot k \cdot \frac{D}{d} \leq B_{\max}(\gamma, \alpha, |\gamma - \psi|) \quad (3.32)$$

Inequality (3.32) gives a maximum k value. Since k is a normalized body acceleration, Equation (3.32) essentially gives the maximum body acceleration, and thus the critical engine speed for trapping. Up to this point, a critical engine speed for trapping has been obtained based on the constraints on p_0 .

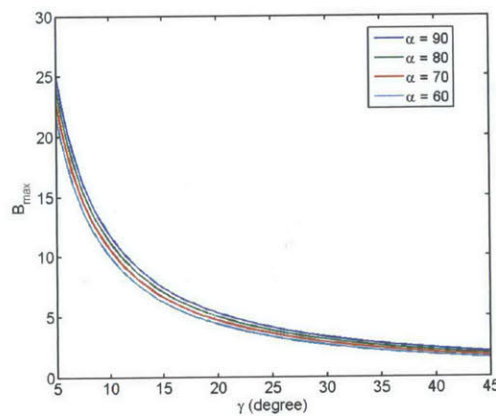


Figure 3.20 B_{\max} as a function of γ . ($\psi = 0^\circ$)

However, this critical speed is a function of D , γ , α , and $|\gamma - \psi|$. While the first two parameters are well defined in a given design, the last two may not be pre-determined.

Figure 3.20 plots B_{\max} as a function of γ with different α . It demonstrates that B_{\max} does not vary significantly with α . Figure 3.21 plots B_{\max} as a function of γ with different ψ . It indicates that B_{\max} is very insensitive with ψ . Therefore, α and ψ will not significantly alter the critical speed predicted by this model. Thus, they are assumed to be two constant inputs to the model. Then, the critical engine speed for trapping depends on γ and D only.

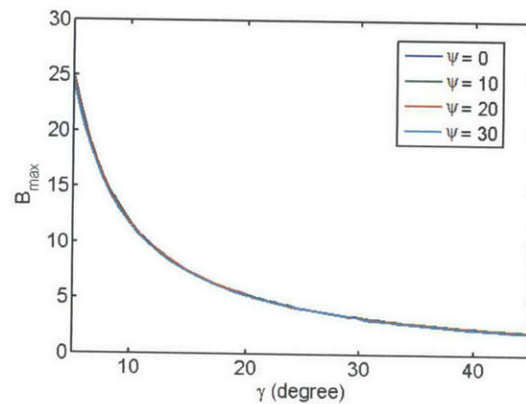


Figure 3.21 B_{\max} as a function of γ . ($\alpha = 90^\circ$)

Actually, D (See Equation (3.30).) has a geometric indication as illustrated in Figure 3.22. As Equation (3.27) indicates, when oil density, surface tension, and engine speed are fixed, only two design parameters determine the oil-gas interface: γ and D . Another interpretation is that only γ and d_{eq} determines the oil-gas interface profile, where $d_{eq} = D \cdot \tan \gamma$ as shown in Figure 3.22.

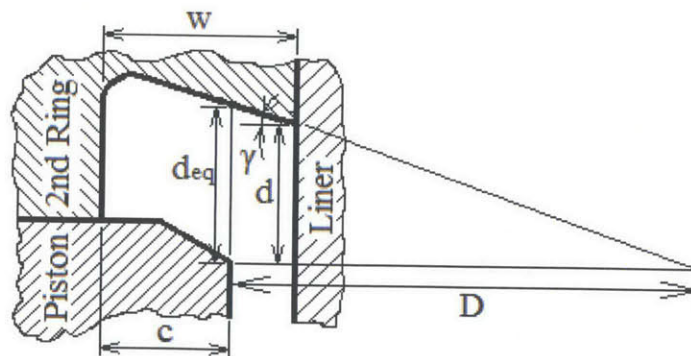


Figure 3.22 Geometric indication of D and d_{eq}

As explained in Section 3.2.3, in a rectangular hook, the design parameters that determine the oil-gas interface profile are γ and d . However, in a Napier ring, the height of the hook region varies along the radial direction. Thus, a proper definition of height of the hook region is required. The discussion in the last paragraph indicates that the proper definition should be d_{eq} , which is the height of a hook region measured along the extension of the piston land.

However, d_{eq} can be a clumsy parameter for engine designers because it depends on the piston-liner clearance. The parameter d may be more simply used because it depends on the dimensions of the hook and the piston chamfer only. Thus, for simple application, d is used in this model instead of d_{eq} . However, one should bear in mind that d_{eq} is the actual determining parameter.

Up to this point, the critical engine speed for oil trapping has been correlated to two design parameters, γ and D . It is shown in Equation (3.32).

However, it still remains to be checked whether the oil-gas interface touches the inner solid boundary. That is, θ , s , c , and R (as defined in Figure 3.17) may further decrease the critical speed. To determine this effect, Equation (3.27) is numerically solved for ξ at a fixed engine speed. The interface profile can then be obtained with Equation (3.22), (3.26), and (3.29). In the following paragraphs, it will be explained how to check whether the oil-gas interface intersects with the inner solid boundary.

Effect of Chamfer Angle, θ

If an oil-gas interface intersects with the solid surface of a piston chamfer, θ will have an effect on the critical trapping speed. The conditions in which this happens can be obtained as follows.

Define x_t as follows:

$$h_x|_{x=x_t} = -\cot \theta \quad (3.33)$$

where x_t is the location where the tangent of oil-gas interface is parallel to the piston chamfer. Plugging Equation (3.33) into (3.29), we get:

$$\eta_t = \frac{1}{2} \left(\xi - \sqrt{\xi^2 - 4(\cos \theta - \cos \alpha)} \right) \quad (3.34)$$

If an interface does not intersect with the piston chamfer, the oil thickness at x_t must be greater than the location of the solid boundary. That is:

$$h_t = c - \int_0^{x_t} \frac{F}{\sqrt{1-F^2}} dx > c - x_t \cdot \cot \theta \quad (3.35)$$

After some algebra, (3.35) becomes:

$$\int_0^{\eta_t} \frac{F}{\sqrt{1-F^2}} d\eta - \eta_t \cdot \cot \theta < 0 \quad (3.36)$$

However, Inequality (3.36) is meaningful only if a real solution for η_t exists. Thus:

$$\xi \geq 2\sqrt{\cos \theta} \quad (3.37)$$

Furthermore, the oil interface should intersect with the inner solid boundary on the piston chamfer, but not the inner hook surface. That is:

$$x_t \leq s \quad \sqrt{2} \cdot \frac{\eta_t}{k} \leq \frac{s}{d} \quad (3.38)$$

If either inequality (3.37) or (3.38) is not satisfied, θ will not have any effect on the critical speed. If both of them are satisfied, inequality (3.36) will give a maximum k , and thus a critical speed that is specified by θ only.

Effect of Hook Depth, c

An oil-gas interface should not intersect with the inner surface of a hook. Otherwise c will affect the critical trapping speed. To satisfy this condition, the minimum h must be greater than zero if oil can be trapped. The location of the minimum point on an oil-gas interface, x_m , is given by:

$$h_x|_{x=x_m} = 0 \quad (3.39)$$

Plugging Equation (3.39) into (3.29), we get:

$$\eta_m = \frac{1}{2} \left(\xi + \sqrt{\xi^2 + 4 \cos \alpha} \right) \quad (3.40)$$

Then, the criterion $h_m > 0$ gives:

$$\frac{\sqrt{2}}{k} \int_0^{\eta_m} \frac{F}{\sqrt{1-F^2}} d\eta < \frac{c}{d} \quad (3.41)$$

On the other hand, if it is c that modifies the critical speed, the oil interface must intersect with the inner surface of the hook rather than the piston chamfer. Thus:

$$x_m > s \quad \sqrt{2} \cdot \frac{\eta_m}{k} > \frac{s}{d} \quad (3.42)$$

If (3.42) does not apply, c has no effect on the critical speed; if (3.42) applies, (3.41) will give a maximum k , and thus a critical speed specified by hook depth c only.

Effect of Fillet Radius in Hook, R

If an oil-gas interface runs into the fillet of a hook, the parameter R will affect the critical speed for trapping. The effect of R can be modeled as follows.

The center of the solid arc is located at (x_c, h_c) , where:

$$x_c = d + w \cdot \tan \gamma - R \cdot \frac{1 + \sin \gamma}{\cos \gamma} \quad (3.43)$$

$$h_c = R \quad (3.44)$$

The oil interface may intersect the solid arc only in the range:

$$x - x_c \geq 0 \quad h_c - h \geq 0 \quad (3.45)$$

or

$$x - x_c \geq 0 \quad h_c - h < 0 \quad \frac{h - h_c}{x - x_c} \leq \tan \gamma \quad (3.46)$$

Here, the interface profile to the right of the symmetric axis (See Figure 3.18) must be considered. Therefore, when $\gamma > \psi$, h is regarded as a multi-valued function of x . The criterion that an oil-gas interface does not intersect with the solid boundary is:

$$(x - x_c)^2 + (h - h_c)^2 \leq R^2 \quad (3.47)$$

in the range specified by (3.45) and (3.46). After some algebra, (3.47) becomes:

$$\left[\left(\eta - \frac{k_{eq}}{\sqrt{2}} \cdot \frac{x_c}{d} \right)^2 + \left(\tilde{h} - \sqrt{2} k_{eq} \cdot \frac{x_c}{d} \right) \cdot \tilde{h} \right]_{\max} \leq 0 \quad (3.48)$$

where \tilde{h} to the left of the symmetric axis is given by:

$$\tilde{h} = \frac{k}{\sqrt{2}} \cdot \frac{c}{d} - \int_0^\eta \frac{F}{(1 - F^2)^{\frac{1}{2}}} d\eta \quad (3.49)$$

and to the right of the symmetric axis:

$$\tilde{h} = \frac{k_{eq}}{\sqrt{2}} \cdot \frac{c}{d} - 2 \int_0^{\eta_e} \frac{F}{(1 - F^2)^{\frac{1}{2}}} d\eta + \int_0^\eta \frac{F}{(1 - F^2)^{\frac{1}{2}}} d\eta \quad (3.50)$$

(3.48) gives a maximum k value, and hence a critical speed specified by R only.

Effect of Total Hook Width, w

Strictly speaking, w may also specify a critical speed when the upper edge of an oil-gas interface runs beyond the liner, that is:

$$h_e + (h_e - h_s) > w \quad (3.51)$$

In this case, simulations demonstrate that oil can still be trapped. The interface profile will adjust to the high gas pressure in the corner bounded by the upper surface of the second ring hook and the liner. However, Figure 3.14 suggests that Inequality (3.51) applies only at very low engine speeds, which is below the critical speed. Thus, w will not affect the critical speed. The only effect of w is the minimum engine speed at which the model provides a valid solution for the oil-gas interface profile.

3.2.4.3 Critical Speed Predicted by the Model

Section 3.2.4.2 indicates that, for a given design, there can be as many as four critical speeds. They are specified by γ (and D), θ , c , and R respectively. The minimum one is the actual critical engine speed for oil trapping.

In the results to be presented in this section, $\psi = 0^\circ$ and $\alpha = 90^\circ$. The underlying assumption is that the contact angle of oil is 0° . Oil properties are as follows: $\rho = 800\text{kg/m}^3$, $\sigma = 0.02\text{N/m}$. Engine configurations are as follows: $l = 0.158\text{m}$, $r = 0.044\text{m}$.

Effect of γ and d

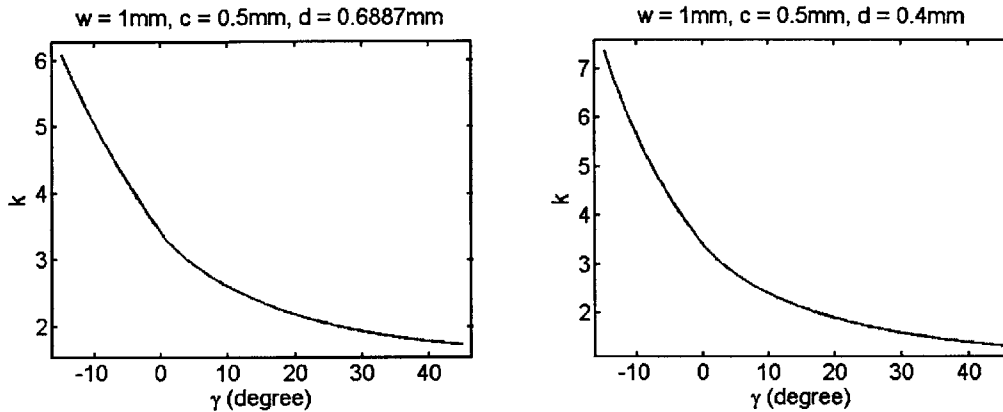


Figure 3.23 Critical k value against tapered hook angle γ . (left: $w = 1\text{mm}$, $c = 0.5\text{mm}$, $d = 0.6887\text{mm}$, see Figure 3.2 (a); right: $w = 1\text{mm}$, $c = 0.5\text{mm}$, $d = 0.4\text{mm}$, see Figure 3.2 (b))

Figure 3.23 shows the critical k value as a function of γ in two typical designs. It indicates that k decreases substantially with the tapered angle. This is consistent with the qualitative analysis in Section 3.2.3.3. Actually, the case when $\gamma = 0^\circ$ cannot be formulated with the equations presented above because $\cot 0^\circ$ tends to infinity. However, following the analysis in Section 3.2.3.1, it can be shown that the critical k value for $\gamma = 0^\circ$ is 3.414, which coincides with Figure 3.23.

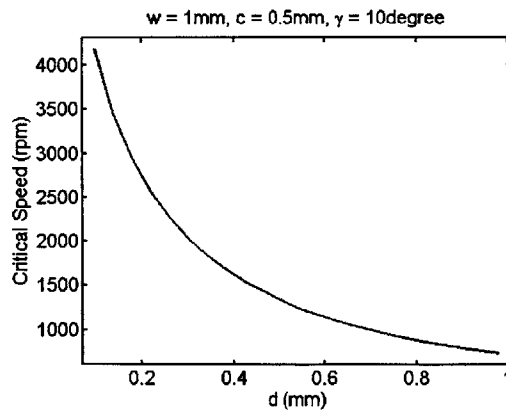


Figure 3.24 Critical speed against height of hook region d . ($w = 1\text{mm}$, $c = 0.5\text{mm}$, $\gamma = 10^\circ$)

The effect of d on the critical engine speed for oil trapping is demonstrated in Figure 3.24. According to Equation (3.24), the correlation is described by:

$$a \leq a_c = k_c^2 \cdot \frac{\sigma}{\rho d^2} \quad (3.52)$$

where k_c denotes the critical k value, a_c denotes the critical body acceleration dependent of the critical trapping speed. Although k_c slightly increases with d when γ is positive, the critical speed still decreases substantially with d . Thus, the power of negative two has an overwhelming effect. Given that a_c scales with the square of the critical engine speed (Equation (1.1)), the critical speed is approximately inverse proportional to d .

Inequality (3.52) actually indicates that a decrease in surface tension and/or an increase in oil density also contribute to decreasing the critical engine speed. However, practically, it is difficult to significantly alter these two oil properties by modifying oil formulations. Thus, they will not be further discussed in this report.

Effect of R , c , and θ

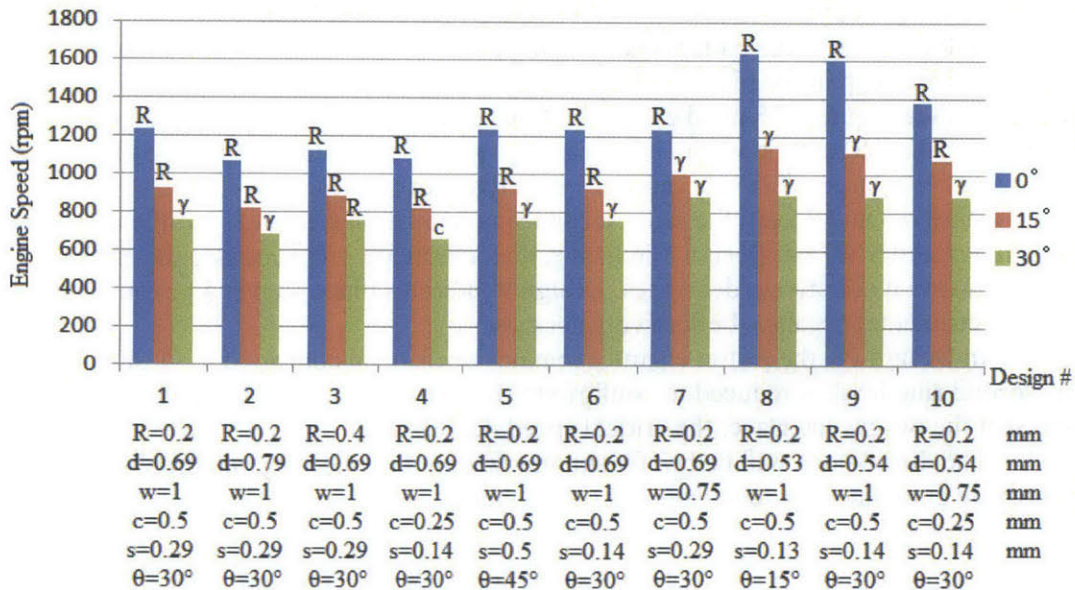


Figure 3.25 Critical engine speed for oil trapping in typical designs

Figure 3.25 shows the critical engine speed for oil trapping in several designs. The dimensions of hooks and chamfers are within the typical range. The letters above the bars signify which parameter ultimately determines the critical speed. The blue bars, red bars, and green bars show the critical speed with 0° , 15° , and 30° tapered angle γ , respectively.

When γ is small, R is usually the determining factor. However, when R is very small, for instance, when it tends to zero, c or γ can be the determining parameter. When γ is large, γ (and d) is usually the determining factor. Design 4 indicates that c can be the determining parameter when c is small. This is because the oil-gas interface intersects with the inner solid boundary at a smaller engine speed. In all the designs studied, θ is not a determining factor.

Since R , c , and θ affects the critical speed by interfering the oil-gas interface, they can only decrease the critical speed, but never increase it. This is desirable. However, R , c , and θ do not alter the general trend that the critical speed decreases with the tapered hook angle γ . An increased R cannot decrease the critical speed as much as an increased γ does. This is evidenced by the fact that the red bar in Design 3 is taller than the green bar in Design 1. Hence, the profile of the inner solid boundary decreases the critical speed only to a limited extent.

A detailed discussion on Figure 3.25 will be presented in the following paragraphs. In order to demonstrate the effects of each geometric parameter, Design 1 will be taken as the reference to be compared with every other design.

Design 2 indicates that an increase in d will decrease the critical speed. This is because d_{eq} is increased. Design 3 indicates that an increase in R can decrease the critical speed when γ is small, but it is not as effective as increasing d . Design 4 indicate that a decrease in c decreases the critical speed by interfering the oil-gas interface. However, when assisted bridging occurs at a high engine speed, a smaller c means a smaller buffer. Thus, it is not for certain whether it is advisable to decrease c . Design 5 indicates that a change in θ does not make a difference as long as D or d_{eq} is not altered. Design 6 indicates that a step in the piston chamfer (that is, the piston chamfer is smaller than the ring hook. See Figure 3.15 middle) does not make any difference, either. Design 7 indicates that a decrease in w , or an increased piston-liner clearance, increases the critical speed when γ is large. This is because d_{eq} effectively decreases.

Design 8 and 9 keep the same second ring hook as in Design 1, but the dimension of piston chamfer varies. Design 8 indicates that a decrease in θ increases the critical speed because d effectively decreases. Design 9 indicates that a step in a piston chamfer is also detrimental because d effectively decreases.

In Design 10, the piston chamfer remains unchanged compared to Design 9, but the second ring hook is reduced to conform to the piston chamfer. Since c is decreased to intersect the oil-gas interface, the critical speed decreases.

The discussions will be briefly summarized in the following paragraphs in order to provide guidelines for reducing the critical speed.

Strategies to Decrease Critical Engine Speed for Oil Trapping

The modeling results indicate that two most effective methods to reduce the critical speed are: 1) to increase tapered hook angle γ ; 2) to increase height of a hook region d (or to increase θ with the same hook).

Two auxiliary methods to further decrease the critical speed are: 1) to increase R . This works only when γ is small; 2) to decrease c . The effects of these two methods are limited. Furthermore, an increased R and/or a decreased c (especially the latter) reduce the oil buffer at high engine speeds. Thus, it is not concluded here whether it is advisable to adopt the auxiliary methods.

In a real automotive engine, γ and d cannot increase indefinitely. Typically, d is smaller than 1mm and θ is smaller than 30° . Thus, the critical speed could be decreased to no less than 570 rpm, which is the critical speed specified by γ and d when $\gamma = 30^\circ$, $d = 1\text{mm}$, $c = 0.5\text{mm}$, and $w = 1\text{mm}$. Considering the inaccuracies of the model, which will be discussed in Section 3.4.1, the actual critical speed may be higher than predicted. Given that the idle speed is typically between 600rpm and 800rpm, it is not for certain

whether the actually critical speed is indeed below the critical speed. Experiments may be needed to verify that.

In order to decrease the critical speed with more confidence, modifications on the geometric configuration can be applied. A few ideas will be presented in Section 3.2.5.

3.2.4.4 Volume of Trapped Oil

Another objective of modeling oil trapping is to obtain the trapping capability. It will indicate how much oil can be accumulated at the entrance of second ring groove, and constitute a boundary condition in the bridging model.

It must be emphasized that the actual quantity of trapped oil can be smaller than the trapping capability. When the oil supplied to the hook region is no more than the trapping capability, all the supplied oil can be trapped. When the oil supply is more than the trapping capability, some oil will escape the hook region. In the latter case, the quantity of oil that stays in the hook region is approximately equal to the trapping capability.

In a two-dimensional analysis, the quantity of oil is measured by the cross sectional area of oil. The quantity of trapped oil can be obtained by integrating the oil-gas interface profile and then reducing the area occupied by solid. Thus, the trapping capability V_{tr} can be written in the form:

$$V_{tr} = V_{int} - V_{sol} \quad (3.53)$$

where V_{int} is associated with the integral of interface profile, and V_{sol} is associated with the shape of solid boundary. It can be shown that:

$$V_{sol} = \begin{cases} -AB + \left(1 - \frac{\pi}{4} + \tan \frac{\gamma}{2} - \frac{\gamma}{2}\right) R^2 + \frac{A^2 \cot \gamma}{2} + \frac{2cs - s^2 \cot \theta}{2} & (\theta \neq 0, \gamma \neq 0) \\ -AB + \left(1 - \frac{\pi}{4} + \tan \frac{\gamma}{2} - \frac{\gamma}{2}\right) R^2 + \frac{A^2 \cot \gamma}{2} & (\theta = 0, \gamma \neq 0) \\ \left(1 - \frac{\pi}{4}\right) R^2 + \frac{2cs - s^2 \cot \theta}{2} & (\theta \neq 0, \gamma = 0) \\ \left(1 - \frac{\pi}{4}\right) R^2 & (\theta = 0, \gamma = 0) \end{cases} \quad (3.54)$$

where:

$$A = d + w \cdot \tan \gamma - \frac{1 + \sin \gamma - \cos \gamma}{\cos \gamma} \cdot R \quad (3.55)$$

$$B = w + d \cdot \cot \gamma \quad (3.56)$$

and:

$$V_{\text{int}} = \begin{cases} -Dx_e + \left(x_e x_s - \frac{x_s^2}{2}\right) \cot \gamma - \int_0^{x_e} \int_0^x \frac{F}{\sqrt{1-F^2}} dx' dx - \int_{x_s}^{x_e} \int_{x_s}^x \frac{F}{\sqrt{1-F^2}} dx' dx & (\gamma > \psi, \gamma \neq 0) \\ -Dx_s + \frac{x_s^2}{2} \cot \gamma - \int_0^{x_s} \int_0^x \frac{F}{\sqrt{1-F^2}} dx' dx & (\gamma \leq \psi, \gamma \neq 0) \\ cd - \int_0^{x_s} \int_0^x \frac{F}{\sqrt{1-F^2}} dx' dx & (\psi \geq \gamma = 0) \end{cases} \quad (3.57)$$

3.2.5 More Potential Approaches to Decrease Critical Trapping Speed

As explained in Section 3.2.4.3, by optimizing the parameters of the traditional design, the critical speed may not be reliably reduced to below the idle speed. A few more ideas aiming at substantially decreasing the critical speed will be presented in this section.

3.2.5.1 A Larger Cut on Top of Piston Third Land

The dimensions of a second ring hook are restricted by the size of the second ring. However, a hook region consists of both a hook and a piston chamfer. Thus, by introducing a larger cut on the top of piston third land, the height of a hook region (d) can be effectively increased. Figure 3.26 illustrates this idea. The increased d will decrease the critical trapping speed.

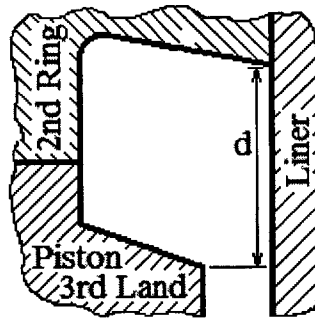


Figure 3.26 A larger cut on top of piston third land

One drawback of this design is the increased difficulties in manufacturing and increased cost.

3.2.5.2 Double Cuts on Top of Piston Third Land

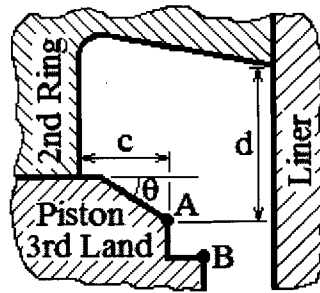


Figure 3.27 Double cuts on top of piston third land

As discussed in Section 3.2.4.3, a smaller c can decrease the critical speed. The concern is that the buffer for the upcoming oil is reduced, which possibly increases the risk of assisted bridging at a high engine speed. Therefore, a desirable situation is that c can be decreased without reducing the size of oil buffer. Figure 3.27 demonstrates one possible solution. The space above the edge A is regarded as the hook region. The depth (c) of this hook region is small. There is an additional cut on the piston land between edge A and B. The additional cut allows a wide buffer for upcoming oil at a high engine speed. One uncertainty in this geometry is that the lower contact line of trapped oil may be pinned at edge B instead of edge A. However, if this occurs, the effective hook height d is increased. Thus, the critical trapping speed can also be decreased.

In terms of manufacturing, this design is similar to that shown in Section 3.2.5.1. Thus, they bear the common disadvantages. However, the ideas behind these two designs are different.

3.2.5.3 Rounded Edge on Piston Chamfer

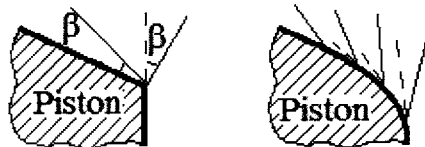


Figure 3.28 Effect of rounded edge. (Left: contact line pinned at a sharp edge; right: contact line moves smoothly through a rounded edge.)

An important mechanism behind oil trapping is that the contact line can be pinned at the outer edge of a piston chamfer. As illustrated in Figure 3.9, it results from the sharp edge. In contrast, if the edge is rounded, the limiting angle would vary gradually and the contact line can advance smoothly. Thus, the contact line cannot be pinned and more oil can be drained instead of being trapped.

From a dynamic perspective, a rounded edge allows a thicker oil film in the vicinity of a chamfer edge. This is evidenced by the simulations demonstrated in Figure 3.29. Lubrication theory implies that a thicker oil film give rise to larger volume flux. Thus, more oil can be drained through this wider oil passage.

CA: 158.4

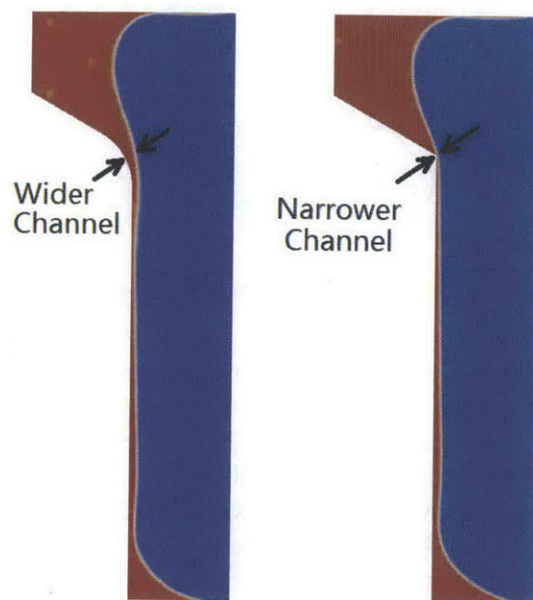


Figure 3.29 Oil passage in the vicinity of outer edge of piston chamfer

Thus, a fillet at the edge of piston chamfer would be beneficial from both static and dynamic perspectives.

3.2.6 Closure

In this Section, the phenomenon of oil trapping in a second ring hook and a chamfer on piston third land has been introduced. By tracing the surface profile of trapped oil, the reason why oil trapping occurs at low engine speeds has been explained, and a theoretical model predicting the critical trapping speed and trapping capability has been developed. By optimizing the geometric design of a hook and a chamfer, the critical engine speed for oil trapping can be decreased.

Apart from providing design guidelines, in this work, a practical objective of modeling oil trapping is to obtain an input for the SS bridging model. The SS bridging model will be introduced in Section 3.3.

3.3 Self-Sustained (SS) Bridging

Oil trapping is a prerequisite of SS bridging. However, SS bridging does not necessarily occur when oil is trapped. It is not straightforward to tell whether SS bridging occurs at low engine speeds or high engine speeds (but still below the critical speed for trapping). As will be shown, less oil is needed for SS bridging at a higher speed. However, the quantity of trapped oil is also smaller. At a lower speed, more oil is needed

for SS bridging but more oil is trapped. Thus, a quantitative evaluation is required to determine the speed range in which SS bridging occurs.

3.3.1 Modeling Method

The modeling method is similar to that for trapping. The oil-gas interface profile is determined from a quasi-static equilibrium between surface tension and body force. However, the maximum upward body acceleration is to be used. While the maximum downward body acceleration does not occur at BDC for typical engine configurations, the maximum upward body acceleration always occurs at TDC. In order to distinguish from the downward acceleration, the maximum upward acceleration is denoted with g in the remaining of this report. At a same engine speed, g is larger than a . The condition that a physically valid interface profile exists requires a constraint on oil pressure. Within the constraint, oil pressure field at a certain engine speed can be solved from a constraining condition on one edge of the interface. Then, the oil-gas interface profile can be obtained and compared to that of trapped oil.

3.3.1.1 Formulation

Some geometric parameters additional to those defined in Figure 3.17 are illustrated in Figure 3.30. Here, x_t is the location of lower contact line, which is unknown. The receding contact angle is denoted with χ and the advancing contact angle is denoted with ϕ . It should be noted that ϕ can be greater than the static contact angle, which is assumed zero. It can vary with the advancing velocity of the contact line. However, for simplicity, it will be assumed constant.

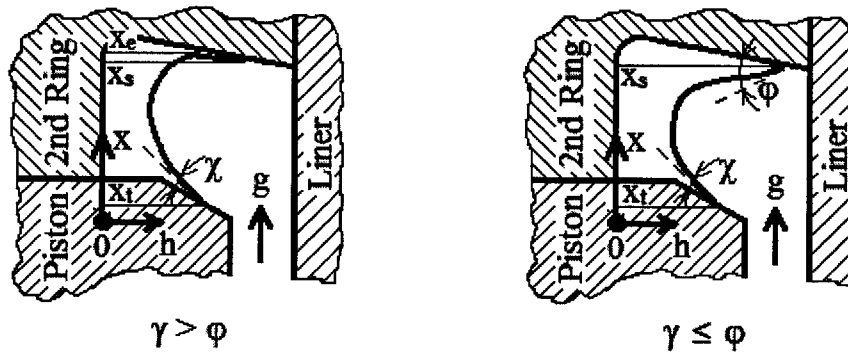


Figure 3.30 Geometric parameters in the model for SS bridging

The equation for the oil-gas interface profile is given by the pressure balance:

$$\sigma \cdot \frac{-h_{xx}}{(1 + h_x^2)^{2/3}} = p_t + \rho g(x - x_t) \quad (3.58)$$

Integrating (3.58) with the boundary condition:

$$h_x(x = x_t) = -\cot(\chi + \theta) \quad (3.59)$$

we get:

$$\frac{-h_x}{(1 + h_x^2)^{1/2}} = \frac{\rho g}{2\sigma}(x - x_t)^2 + \frac{p_t}{\sigma}(x - x_t) + \cos(\chi + \theta) \quad (3.60)$$

For simplicity, a few dimensionless variables are introduced:

$$\varepsilon = \sqrt{\frac{\rho g}{2\sigma}}(x - x_t) \quad (3.61)$$

$$\eta_t = \sqrt{\frac{\rho g}{2\sigma}}x_t \quad (3.62)$$

$$\zeta = p_0 \cdot \sqrt{\frac{2}{\rho g \sigma}} \quad (3.63)$$

$$\bar{k} = d \sqrt{\frac{\rho g}{2\sigma}} \quad (3.64)$$

Then, Equation (3.60) becomes:

$$\frac{-h_x}{(1 + h_x^2)^{1/2}} = F(\varepsilon) = \varepsilon^2 + \zeta\varepsilon + \cos(\chi + \theta) \quad (3.65)$$

When $\gamma > \varphi$, x_e and x_s (as defined in Figure 3.30) are specified by:

$$h_x|_{x=x_s} = \cot(\gamma - \varphi) \quad (3.66)$$

$$h_x|_{x=x_e} = +\infty \quad (3.67)$$

Plugging them into (3.65), we get:

$$\varepsilon_s = \sqrt{\frac{\rho g}{2\sigma}}(x_s - x_t) = \frac{1}{2} \left(-\zeta - \sqrt{\zeta^2 - 4[\cos(\chi + \theta) + \cot(\gamma - \varphi)]} \right) \quad (3.68)$$

$$\varepsilon_e = \sqrt{\frac{\rho g}{2\sigma}}(x_e - x_t) = \frac{1}{2} \left(-\zeta - \sqrt{\zeta^2 - 4[\cos(\chi + \theta) + 1]} \right)$$

That the left hand side of (3.65) ranges from -1 to 1 requires:

$$\zeta \leq -2\sqrt{\cos(\chi + \theta) + 1} \quad (3.70)$$

When $\gamma \leq \varphi$, x_s (as defined in Figure 3.30) is specified by:

$$h_x|_{x=x_s} = \cot(\varphi - \gamma) \quad (3.71)$$

That the left hand side of (3.65) ranges from -1 to 1 requires:

$$\zeta \leq -2\sqrt{\cos(\chi + \theta) + \cos(\gamma - \varphi)} \quad (3.72)$$

Equation (3.68) is one solution for Equation (3.71) for all possible ζ values. When $-2\sqrt{\cos(\chi + \theta) + 1} \leq \zeta \leq -2\sqrt{\cos(\chi + \theta) + \cos(\gamma - \varphi)}$, there is another solution for Equation (3.71):

$$\varepsilon_{s,2} = \sqrt{\frac{\rho g}{2\sigma}}(x_{s,2} - x_t) = \frac{1}{2} \left(-\zeta + \sqrt{\zeta^2 - 4[\cos(\chi + \theta) + \cos(\gamma - \varphi)]} \right) \quad (3.73)$$

Both solutions will be considered in the model. Actually, the modeling result shows that no more than one solution gives a valid result at a certain engine speed.

3.3.1.2 Constraining Conditions

The governing equation of oil-gas interface profile is Equation (3.65). It is a first order ODE with one unknown coefficient. Furthermore, x_t needs to be solved as well. Thus, three constraining conditions are required. The choice of constraining conditions leads to two approaches to model SS bridging:

1. Modeling by distance: equate the oil volume to the volume of trapped oil, and then check the location of the upper contact line. If it exceeds the liner, SS bridging occurs; otherwise, SS bridging does not occur;
2. Modeling by volume: fix the upper contact line at the intersection of hook surface and liner, and then check the volume of oil. This is the quantity of oil that is needed for SS bridging. If it is less than the volume of trapped oil, SS bridging occurs; otherwise, SS bridging does not occur.

In both approaches, in order to judge whether SS bridging occurs, the quantity of trapped oil needs to be known. However, as explained in Section 3.2.3.1, it can be involved to determine the actual quantity of trapped oil. For simplicity, the trapping capability will be compared with in the model of SS bridging. As a result, this model only evaluates the risk of SS bridging. A risk of SS bridging does not mean it would necessarily occur. If the oil supply to the hook region is irredundant, SS bridging would by no means occur.

In the following paragraphs, the general cases where $\gamma \neq \theta \neq 0$ will be analyzed. If either γ or θ is zero or if $\gamma = \theta$, the mathematics must be adjusted. However, the general procedures are identical. For coherence, formulations for these cases will not be presented.

Modeling by Distance

In this modeling approach, the constraining conditions for Equation (3.65) are:

$$\begin{cases} h_e + (h_e - h_s) = w - (x_s - d) \cdot \cot \gamma & (\gamma > \varphi) \\ h_s = w - (x_s - d) \cdot \cot \gamma & (\gamma \leq \varphi) \end{cases} \quad (3.74)$$

$$h_t = c - x_t \cdot \cot \theta \quad (3.75)$$

$$V = V_{tr} \quad (3.76)$$

where V is the amount of oil, and V_{tr} is the trapping capability given by Equation (3.53), (3.54), and (3.57).

There are two unknown variables to be solved: x_t (or η_t in dimensionless form) and ζ . First, η_t can be expressed as a function of ζ . After some algebra, Equation (3.74), combined with (3.75), becomes:

$$\eta_t = \frac{G(\zeta) - \tilde{k} \cdot \frac{D}{d}}{\cot \theta - \cot \gamma} \quad (3.77)$$

where:

$$G(\zeta) = \begin{cases} \varepsilon_s \cot \gamma + \int_0^{\varepsilon_s} \frac{F}{\sqrt{1-F^2}} d\varepsilon - 2 \int_0^{\varepsilon_s} \frac{F}{\sqrt{1-F^2}} d\varepsilon & (\gamma > \varphi) \\ \varepsilon_s \cot \gamma - \int_0^{\varepsilon_s} \frac{F}{\sqrt{1-F^2}} d\varepsilon & (\gamma \leq \varphi) \end{cases} \quad (3.78)$$

where F is given by Equation (3.65). Equation (3.77) explains why the formulation needs to be adjusted when $\gamma = \theta$, $\gamma = 0$, or $\theta = 0$.

With Equation (3.77), η_t is eliminated in the formulation. Only ζ , which is a normalized form of p_0 , remains to be solved. It can be solved from Equation (3.76). The following paragraphs will demonstrate how to obtain V in Equation (3.76).

Similar to the trapping model, the oil volume V can be separated into two parts:

$$V = V_{int} - V_{sol} \quad (3.79)$$

V_{sol} can be evaluated with the first equation in (3.54). Since it is a common part for trapping and bridging, it can be neglected. However, if the lower contact line rises to the inner hook surface, V_{sol} is no longer common. This scenario will be discussed in Section 3.3.1.3. For generality, V_{sol} is retained in the formulation.

V_{int} can be obtained by integrating the interface profile h . After some algebra:

$$V_{int} = \begin{cases} -\frac{\tilde{k}D}{2d} \eta_t - \varepsilon_e G - \frac{\eta_t G}{2} + \left(\varepsilon_e \varepsilon_s - \frac{\varepsilon_s^2}{2} \right) \cot \gamma + W & (\gamma > \varphi) \\ -\frac{\tilde{k}D}{2d} \eta_t - \varepsilon_s G - \frac{\eta_t G}{2} + \frac{\varepsilon_s^2}{2} \cot \gamma + W & (\gamma \leq \varphi) \end{cases} \quad (3.80)$$

where

$$W = \begin{cases} - \int_0^{\varepsilon_e} \int_0^{\varepsilon} \frac{F}{\sqrt{1-F^2}} d\varepsilon' d\varepsilon - \int_{\varepsilon_s}^{\varepsilon_e} \int_{\varepsilon_s}^{\varepsilon} \frac{F}{\sqrt{1-F^2}} d\varepsilon' d\varepsilon & (\gamma > \varphi) \\ - \int_0^{\varepsilon_s} \int_0^{\varepsilon} \frac{F}{\sqrt{1-F^2}} d\varepsilon' d\varepsilon & (\gamma \leq \varphi) \end{cases} \quad (3.81)$$

and G is given in Equation (3.78), ε_e is given in Equation (3.69), and ε_s is given in Equation (3.68) or (3.73). They are functions of ζ only. If one plugs (3.77) into (3.80), V_{int} becomes a function of ζ and \tilde{k} only. \tilde{k} , which is a normalized engine speed, is first fixed at a certain value. Then, by combining Equation (3.80), (3.79), and (3.76), an equation for ζ is obtained. This equation is solved numerically with secant method within the range specified by (3.70) or (3.72).

After ζ is solved for, x_s can be calculated with Equation (3.68) or (3.73), (3.61), and (3.62). The location of the upper contact line can then be calculated with the right hand side of Equation (3.74). If it is less than w , there is no risk of SS bridging; otherwise, there exists a risk. The risk of SS bridging is indicated by how much the contact line exceeds the liner. The risk is higher if it exceeds more.

Then, the same steps are repeated with another \tilde{k} value. In this way, the risk of SS bridging at a different engine speed is evaluated.

Modeling by Volume

In this modeling approach, the constraining conditions for Equation (3.65) are:

$$\begin{cases} h_e + (h_e - h_s) = w & (\gamma > \varphi) \\ h_s = w & (\gamma \leq \varphi) \end{cases} \quad (3.82)$$

$$x_s = d \quad (3.83)$$

$$h_t = c - x_t \cdot \cot \theta \quad (3.84)$$

Still, three variables are relevant in this formulation: η_t , ζ , and \tilde{k} . A correlation between them can be obtained from Equation (3.82), (3.83), and (3.84):

$$\tilde{k} = \frac{G(\zeta) + \varepsilon_s (\cot \theta - \cot \gamma)}{q + \cot \theta} \quad (3.85)$$

$$\eta_t = \frac{G(\zeta) - \varepsilon_s (p + \cot \gamma)}{q + \cot \theta} \quad (3.86)$$

where

$$q = \frac{w - c}{d} \quad (3.87)$$

and G is given in Equation (3.78) and ε_e is given in Equation (3.68) or (3.73). Here, \tilde{k} , η_t , and ζ are not coupled as in the first approach.

The objective in this modeling approach is to obtain a correlation between oil volume and engine speed, that is, between V and \tilde{k} . This can be achieved by solving ζ as a function of \tilde{k} from Equation (3.85), and then calculating V from Equation (3.79), (3.80),

and (3.86) with ζ known. However, in order to save computational effort, this strategy was not adopted. Instead, it is treated in the following manner. An array of ζ is taken within the range specified by (3.70) or (3.72). A projection from ζ to \bar{k} is established with Equation (3.85). Similarly, a projection from ζ to V can be established with Equation (3.79), (3.80), and (3.86). By combining these two projections through ζ , a projection from \bar{k} to V can be established. In this way, the oil volume needed for SS bridging is determined at some discrete engine speeds. By taking a sufficient number of ζ values, a satisfactory correlation can be obtained.

Then, V can be compared with the trapping capability. If V is greater, SS bridging can be avoided; otherwise, there exists a risk of SS bridging. The risk is greater if the trapping capability exceeds V more.

Comparison between Two Approaches

If the actual quantity of trapped oil can be somehow determined, the result of the second model (by volume) can be directly compared to without a new computation. However, a brand new computation is required for the first model (by distance) if oil quantity varies. Furthermore, the second model (by volume) is simpler in mathematics. Thus, modeling by volume is deemed advantageous.

However, at some engine speeds, the model by volume does not provide a valid solution. A few possible reasons are: 1) a solution of ζ does not exist; 2) the numerical scheme fails to find the solution; 3) the result is not realistic, for instance, $\eta_t < 0$. Thus, the model by distance is also needed to provide a more complete result for reference.

3.3.1.3 Special Cases

Breaking-Up of Oil-Gas Interface

At a high engine speed (but still below the critical speed for trapping), the oil-gas interface may touch the inner solid boundary before the body acceleration reaches the maximum. This case is considered in the model. With both modeling methods, it is checked whether the oil-gas interface corresponding to the maximum upward body acceleration intersects with the solid boundary. Mathematically, it is checked whether the minimum h is negative. If so, the result needs to be modified as follows.

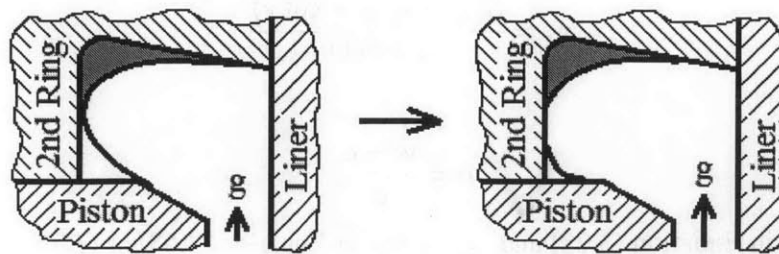


Figure 3.31 Breaking-up of oil-gas interface (Left: at the moment of breaking-up; right: separation at TDC)

In the model by distance, the body acceleration under which the minimum h is zero is calculated. The interface profile under this body acceleration is integrated to obtain the oil volume above the intersection (as illustrated by the shaded region in Figure 3.31). It is assumed that the upper portion and lower portion of oil will separate as body acceleration increases. Only the evolution of the upper portion will be traced. Its interface profile under the maximum body acceleration will be calculated. If the upper contact line exceeds the liner, there is a risk of SS bridging; otherwise, SS bridging is avoided.

In the model by volume, the upper contact line is still pinned at the intersection of hook and liner. However, the constraining conditions change as illustrated in Figure 3.32. This interface profile will be integrated to obtain the amount of oil needed for SS bridging. The volume of the circular oil cluster in the lower corner is assumed negligible. In this case, the model overestimates the risk of SS bridging. From a practical perspective, this is more acceptable than an underestimation.

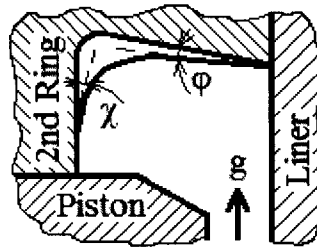


Figure 3.32 Oil-gas interface at TDC after it breaks-up

Step in Piston Chamfer

If $s < c \cdot \tan\theta$, there will be a step in the piston chamfer (See Figure 3.15 middle.). Boundary conditions (3.75) and (3.84) are not valid if the lower contact line steps on the flat step. Thus, when $x_t > s$, the computation will switch to the solution for $\theta = 0$. As a result, the model may fail to provide a solution in a small interval of engine speeds at which such transition occurs.

3.3.2 Results and Discussions

In this section, the results predicted by two modeling approaches will be presented. First, the results of one typical design will be demonstrated as an example. Then, the speed range in which a risk of SS bridging exists predicted by two approaches will be compared. Finally, the speed range in which a risk of SS bridging exists will be compared with the trapping range.

In the results to be presented in this section, $\varphi = 30^\circ$ and $\chi = 0^\circ$. While the latter assumption is probably valid, the former one is not for certain. The effect of the leading contact angle φ will be discussed in Section 3.3.3.

Figure 3.33 shows the modeling result for Design 1 in Figure 3.25. The blue, green, and red curves correspond to the results with $\gamma = 0^\circ, 15^\circ, \text{ and } 30^\circ$, respectively.

The curves do not extend to 0rpm because inequality (3.51) is satisfied at very low speeds.

The left figure shows the results modeled by distance. The solid curves denote the location of the upper contact lines in the direction perpendicular to a liner, and the dashed line denotes the location of the liner (w). When the solid curves lie above the black dashed line, there is a risk of SS bridging. The risk is higher at a certain speed if the solid curve exceeds the dashed line more. The figure indicates that the risk is large when γ is 0° .

The right figure shows the results modeled by volume. The solid curves denote the trapping capability, and the dashed curves denote the bridging requirement. When a solid curve lies above the corresponding dashed curve, there is a risk of SS bridging. If the ratio between the two volumes is taken as an indication of such a risk, the risk is higher when γ is smaller. There is an unsmooth change in each dashed curve. This results from the breaking-up of the oil-gas interface, as explained in Section 3.3.1.3. The trapping capability decreases rapidly with engine speed. The decreasing rate increases with γ because a larger hook angle suppresses oil trapping, as explained in Section 3.2.3.3. The bridging requirement decreases in an approximately piece-wise linear manner. Similar to the argument that a negative hook angle favors trapping (See Section 3.2.3.3), a piston chamfer favors SS bridging. This is why the bridging requirement does not decrease rapidly with engine speed.

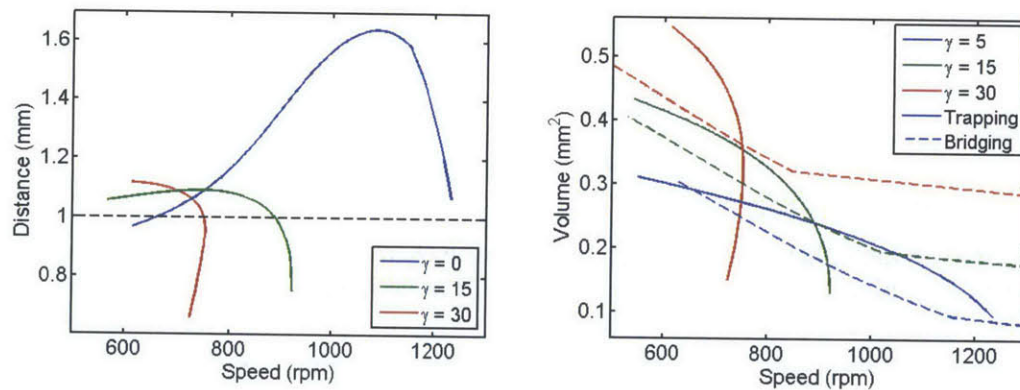


Figure 3.33 Modeling results for Design 1 ($R = 0.2\text{mm}$, $d = 0.69\text{mm}$, $w = 1\text{mm}$, $c = 0.5\text{mm}$, $s = 0.29\text{mm}$, $\theta = 30^\circ$) (Left: modeling by distance; right: modeling by volume)

In the design shown in Figure 3.33, when $\gamma = 0^\circ$, a risk of SS bridging exists in a high speed range; when $\gamma = 15^\circ$ or 30° , the risk exists at almost all engine speeds when oil trapping occurs. It indicates that there is no general rule on the speed range in which SS bridging possibly occurs. It depends on each specific design.

Figure 3.34 shows the speed range in which a risk of SS bridging exists. The bars in light colors demonstrate the results modeled by distance, and in dark colors by volume. Figure 3.34 indicates that the two modeling approaches provide coincident results for all the designs evaluated.

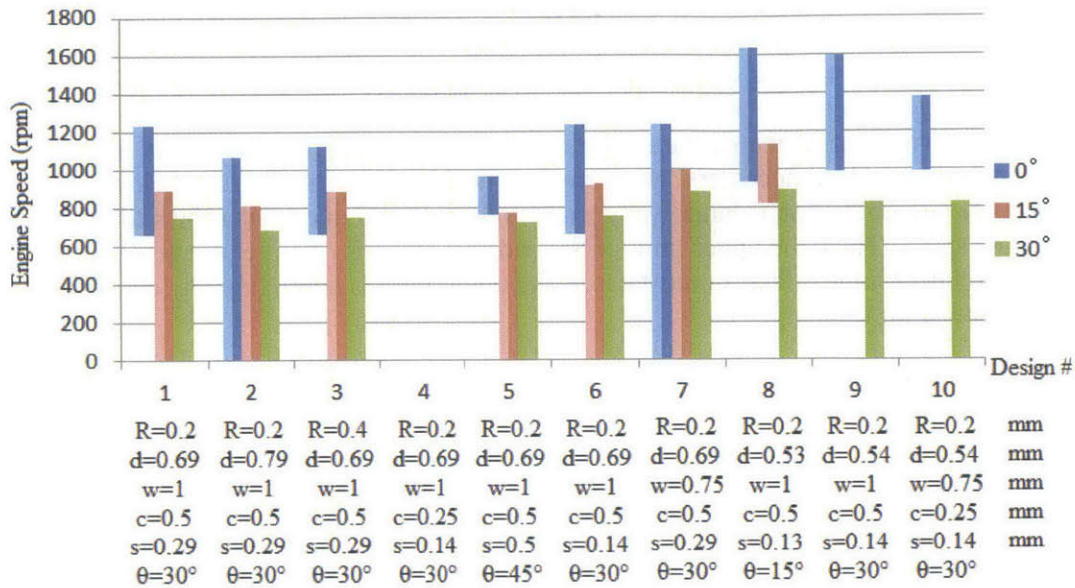


Figure 3.34 Ranges of engine speed in which a risk of SS bridging exists (Light colour: model by distance; dark colour: model by volume)

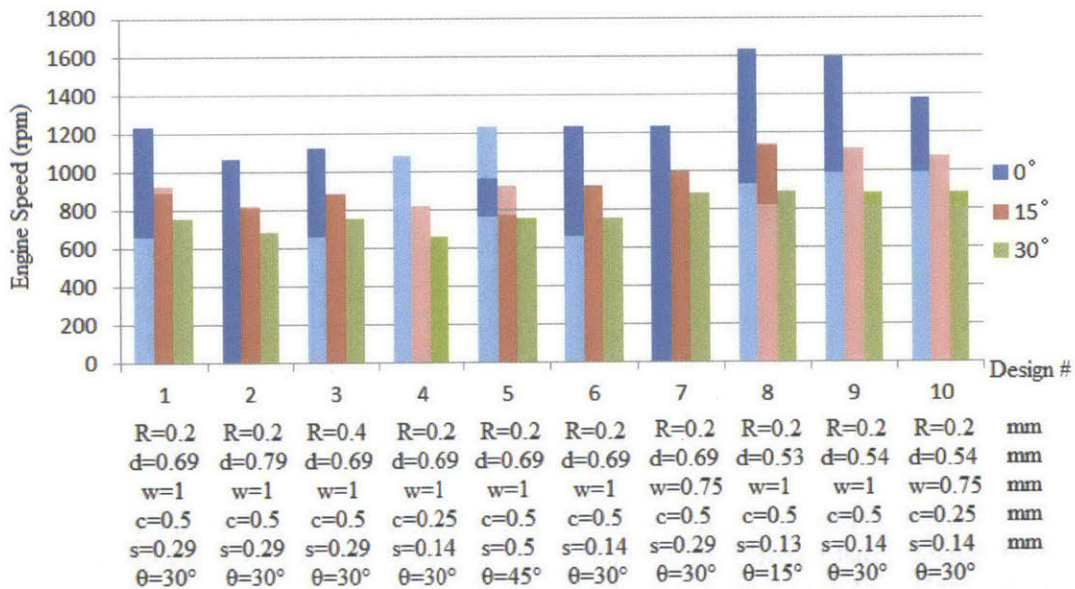


Figure 3.35 Oil trapping and self-sustained bridging modeled by volume (light colour: trapping without self-sustained bridging; dark colour: trapping and self-sustained bridging)

Figure 3.35 combines the results of trapping model and SS bridging model (by volume). The segments filled with light colors indicate oil trapping without SS bridging,

and the segments in dark colors indicate trapping with SS bridging. Since there are cases where oil is trapped without SS bridging occurring, SS bridging is not a necessary result of oil trapping. SS bridging can occur at a low, medium, or high speed range within the trapping range. It depends on the specific geometry design. Unfortunately, no evident correlation with any geometric parameter is observed from Figure 3.35. Thus, a case-by-case analysis is indeed necessary. Since an automotive engine hardly runs below 600rpm except for engine start and shutdown, designers do not need to consider the situations at very low speed. Thus, the upper limit of SS bridging range is of more practical interest, while the lower limit is less. In most cases, the upper limit is approximately equal to the critical speed for trapping.

3.3.3 Sensitivity Analysis

The effect of two contact angles on modeling results will be discussed in this section.

Figure 3.36 shows how the quantity of oil needed for SS bridging varies with the advancing contact angle ϕ . It is sensitive to ϕ . The curve shifts upwards as ϕ increases. The intersection of a solid curve and the dashed curve, which denotes the trapping capability, signifies the upper limit of SS bridging range. It decreases with ϕ , but does not vary as significantly as the solid curves shift. This is because the slope of the dashed line is large in the vicinity of the intersections.

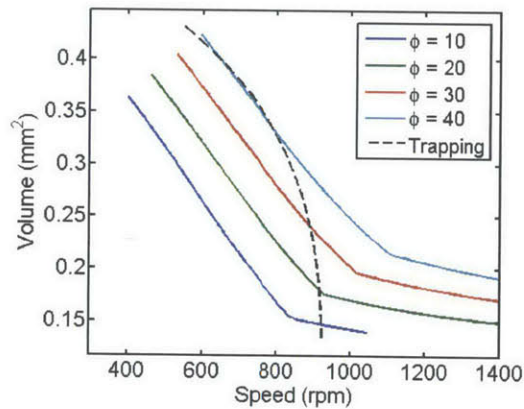


Figure 3.36 Sensitivity of oil volume that is needed for SS bridging to advancing contact angle ϕ

It is not surprising that the upper limit of SS bridging range decreases with ϕ . A smaller ϕ means that the oil is more inclined to spread to the liner. Thus, SS bridging is more probable, and the SS bridging range will be wider. When ϕ is larger, oil is less likely to spread and SS bridging is less probable at a same engine speed. Thus, the upper limit will decrease.

Figure 3.37 shows how the quantity of oil needed for SS bridging varies with the receding contact angle χ . It is not sensitive to χ . Thus, the uncertainties in the SS bridging model mainly originate from the advancing contact angle.

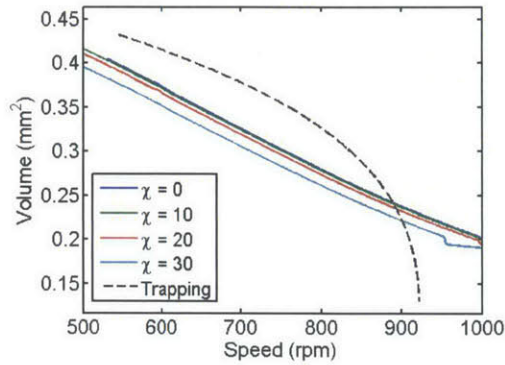


Figure 3.37 Sensitivity of oil volume that is needed for SS bridging to receding contact angle χ

Figure 3.38 demonstrates how the SS bridging range varies with the advancing contact angle ϕ when $10^\circ < \phi < 40^\circ$. Design 1 and Design 4 in Figure 3.35 are taken as examples. The abscissa is the advancing contact angle ϕ , and the ordinate the engine speed. The shaded regime indicates the speed range in which a risk of SS bridging exists. The speed range shrinks substantially with ϕ . An increase of 10° in ϕ can decrease the upper limit by as many as 100rpm. Given that the upper limit lies in the same range as a typical idle speed, a 100rpm difference can significantly alter engine performance.

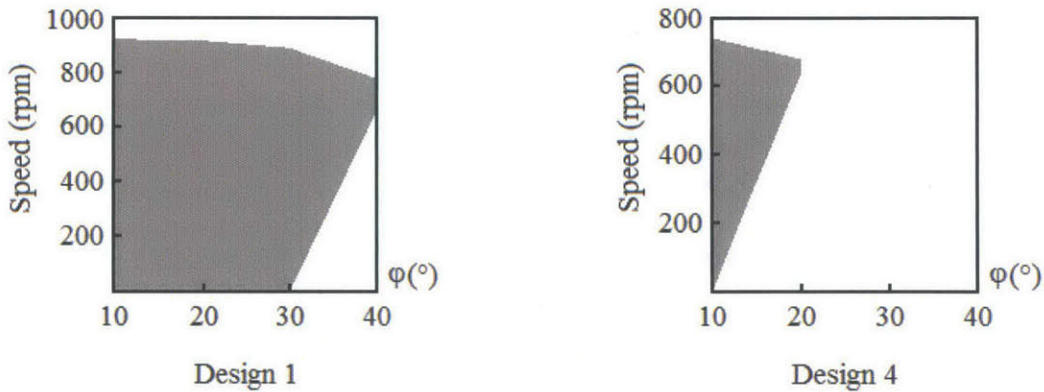


Figure 3.38 Sensitivity of critical speed to advancing contact angle ϕ ($\gamma = 15^\circ$)

The sensitivity analysis indicates that the advancing contact angle ϕ significantly alters the modeling results. An increase in ϕ can prevent SS bridging. Thus, if the surface texture of the hook surface can be modified, or if a surface coating can be introduced to increase contact angle ϕ , SS bridging can be effectively suppressed. Although a modification on the solid surface is accompanied by an increase in ψ and χ , they do not have significant effects. A primary concern with this method is the difficulties in manufacturing and an increased cost.

3.3.4 Strategies for Elimination of SS Bridging

SS bridging can be avoided in engine operations if the upper limit of SS bridging range is less than the idle speed. It can be achieved by two approaches:

1. To allow SS bridging at middle or low engine speeds. That is, the upper limit of SS bridging range is less than the critical speed for trapping. In this case, trapping can occur at certain speeds above the idle speed, but SS bridging cannot.
2. To completely avoid oil trapping, which is the prerequisite of SS bridging. This can be achieved by decreasing the critical speed for trapping to below the idle speed.

To allow SS bridging at middle or low speeds

The feasibility of this strategy has been indicated in Figure 3.35 by Design 4, 5, 9 ($\gamma = 15^\circ$), and 10 ($\gamma = 15^\circ$). SS bridging can even be entirely avoided in the trapping range. However, as explained in Section 3.3.3, the SS bridging range is dependent of the choice of the leading contact angle ϕ . For instance, in Figure 3.36, a risk of SS bridging exists all through the trapping range if $\phi = 10^\circ$. However, it hardly exists if $\phi = 40^\circ$. Thus, there exists remarkable uncertainty in the modeling results.

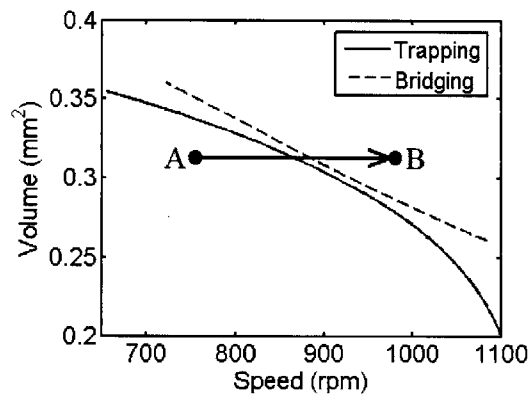


Figure 3.39 Oil trapping and SS bridging in a transient condition

Furthermore, even if the upper limit of SS bridging range is below the idle speed, SS bridging can still occur in a transient condition. An example is illustrated in Figure 3.39. It shows the modeling result of Design 9 with $\gamma = 15^\circ$ in Figure 3.35. The critical trapping speed is 1117rpm and SS bridging does not occur all through the trapping range. Suppose an engine initially operates at the condition A. The engine speed is roughly 750rpm and the quantity of trapped oil is approximately 0.31mm^2 per width. It is below the trapping capability and SS bridging requirement. Thus, all oil can be trapped but SS bridging does not occur. When the engine suddenly accelerates to roughly 990rpm, the quantity of trapped oil will not vary immediately. Thus, the engine condition moves horizontally to point B. The quantity of trapped oil exceeds both the trapping capability and bridging requirement. If the body force is downward at this moment, some oil can be drained to the piston third land. This is desirable. However, if the body force is upward,

severe bridging will occur, which is undesirable. Thus, if oil trapping is not entirely eliminated in engine operations, SS bridging may still occur in a transient condition, and the behavior in a single cylinder can be unpredictable. This is considered as the primary disadvantage of the first strategy, which is to allow SS bridging at middle or low speeds.

However, it is still advisable to make the upper limit of SS bridging range lower than the critical speed for trapping. In this case, one uncertainty in the model can be eliminated. As explained in Section 3.2.2, the definition of trapping in this model is somehow artificial. Above the critical engine speed for trapping, oil may still be stored in the second ring hook in the form of residual oil. It can still possibly support SS bridging when the engine speed is slightly above the critical trapping speed. This is possible if the upper limit of SS bridging range is equal to the critical speed for trapping, but very unlikely if SS bridging occurs in a middle or low speed range. This is because the trapping capability decreases rapidly above the critical trapping speed, but the SS bridging requirement decreases almost linearly. Thus, if the latter is larger than the former at the critical trapping speed, it is very unlikely that the latter will exceed the former at any greater speed. However, if the latter is smaller at the critical trapping speed, the extended curve for trapping capability can still lie above the SS bridging curve in a small range of engine speeds. In order to prevent the latter case, it is desirable if the upper limit of SS bridging range is below the critical trapping speed.

To Avoid Oil Trapping at Any Engine Speed above the Idle Speed

Since the trapping capability is insensitive to contact angles, this strategy contains less uncertainty. Moreover, with this strategy, SS bridging can be eliminated even at a transient condition. Furthermore, oil supply to the second ring groove also possibly decreases if oil trapping is entirely avoided. These points make this strategy advantageous over the first one.

However, as mentioned in Section 3.2.4.3, it may be difficult to decrease the critical trapping speed to below the idle speed. Engine tests are necessary to verify whether oil trapping occurs at the idle speed. If so, auxiliary methods are necessary to further decrease the critical trapping speed. Examples are the methods discussed in Section 3.2.5.

3.4 Comments on the Theoretical Models

3.4.1 Limitations of the Theoretical Models

Both the trapping model and the SS bridging models are based on quasi-static analyses. Inertial forces and viscous forces in the oil are neglected. Since the velocity of trapped oil is not large, these two forces are not expected to significantly alter the force balance. However, the oil-interface needs time to adjust to the time-variant body acceleration. The evolution of the interface actually lags the variation of body acceleration. An underlying assumption behind the quasi-static analysis is that the oil-gas interface can reach a new static state in a very short time. At a low engine speed when the oil-gas interface is not close to the inner solid surface, Rayleigh time (the time scale of surface tension versus inertial force) can be taken as a characteristic time of trapped oil. It

is roughly 14° crank angles at 800rpm. Since the body acceleration varies continuously, it is not for certain whether this duration can be safely neglected. As a result of the neglected reaction time, the model is expected to underestimate the critical trapping speed.

In the models, the gas pressure is assumed uniform. Hence, the model is applicable only to low-load cases. In a high load case, the non-uniform pressure distribution in gas must be considered.

The models require dynamic contact angles as inputs. Given that the surface energy of oil and gas is small, it is not unreasonable to assume a zero static contact angle and zero receding contact angles (ψ and χ). However, it is not straightforward to pre-determine the advancing contact angle (ϕ). It may be time-variant. Unfortunately, the modeling result is sensitive to ϕ . The effect of this uncertainty can be minimized if the second strategy in Section 3.3.4 is adopted and the first strategy is only auxiliary.

In real engine operations, the temperature in the vicinity of a second ring hook can be as high as 200°C . Practically, the oil-gas surface tension (σ) may not be measured at such a high temperature. Furthermore, σ varies with chemical composition of oil and gas, which varies in engine operations. In the results presented in this report, σ is taken as 0.02N/m , which is considered a satisfactory estimation based on data at low temperatures. But anyway, the lack of data in surface tension at high temperatures introduces uncertainties to the model.

The SS bridging model considers SS bridging only. The bridging oil comes entirely from trapped oil. Simulations imply that the model is still applicable when the trapped oil connects with the oil film on the piston land through a narrow neck. However, when there is a remarkable quantity of oil drained from hook to piston land, or supplied from piston land to hook, the constraining conditions in the model is no longer valid and the model is not applicable. Furthermore, that there is no risk of SS bridging does not mean that there is no risk of bridging. Assisted bridging may still occur if oil on the piston land rises sufficiently rapidly. However, assisted bridging is not considered in this model.

In practice, the dynamics of the second ring will change the geometry of the hook region. The moving boundary and the clearance between second ring and its groove will affect the accuracy of this model.

If the amount of oil that is actually supplied to the hook region is known, the model is capable to determine whether SS bridging occurs. However, the actual oil supply requires a more involved modeling on several components. In this work, the model is employed to evaluate only the risk of SS bridging. Therefore, apart from the optimization of geometric design, a fundamental method to eliminate SS bridging is to reduce the oil supply to the hook region.

If it is supposed that the oil in the hook region mostly comes from the OCR gap, a circumferential variation illustrated in Figure 3.40 can be expected. Right above the OCR gap, oil on the liner is scraped by the second ring and oil directly enters the second ring hook. Oil supply is ample in this region and not all oil can be trapped. Some oil will be drained to the piston third land and SS bridging can be maintained in this region. As the oil spreads in the second ring hook along the circumferential direction, the quantity of oil decreases. In the middle of the OCR gap and the second ring gap, all oil can be trapped and no oil will be drained. However, SS bridging can still be maintained by the trapped

oil. In the vicinity of the second ring gap, oil is flushed by blow-by and little oil can stay in this region. As a result, all the oil can be trapped but SS bridging does not occur. Such a circumferential variation implies that SS bridging is most probable above the OCR gap, and least probable in the vicinity of the second ring gap. However, in order to analyze such circumferential variation, the distribution of oil quantity must be known. Then, the model presented in this report can be directly applied to locate the boundaries of these three regions. However, circumferential oil flow is beyond the scope of this work.

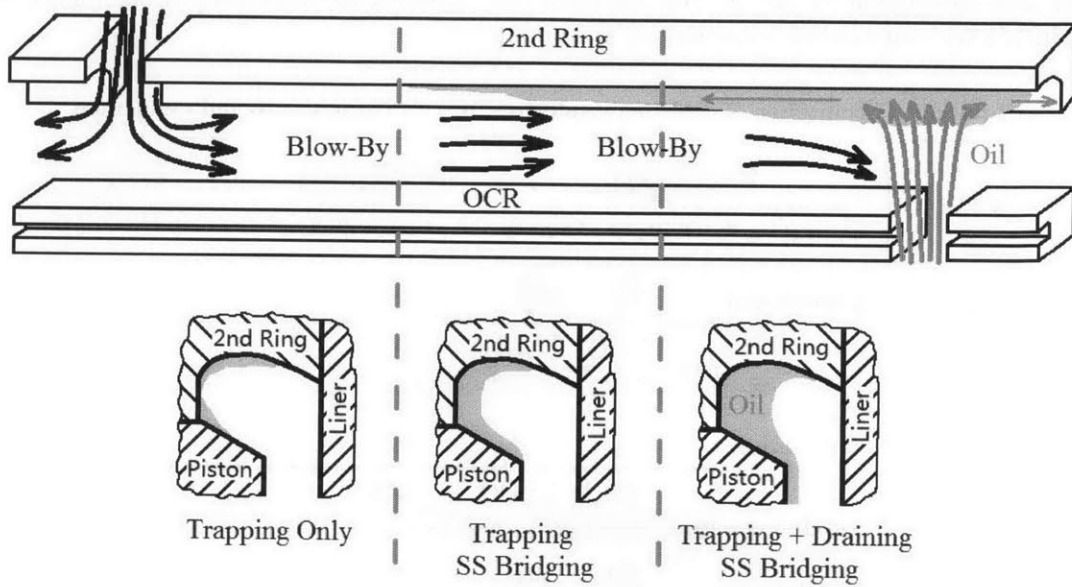


Figure 3.40 Circumferential distribution of oil in second ring hook and piston chamfer

3.4.2 Comparison with Experiments and Simulations

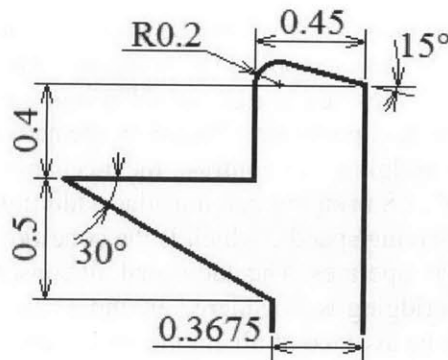





Figure 3.41 Dimensions of the test engine

Figure 3.41 shows the dimensions of the hook region in the experiments described in Section 3.1.2. It falls in the rightmost category in Figure 3.15, which is not explicitly analyzed in this report. The videos taken in the experiments imply that oil is trapped in the mode illustrated in Figure 3.16 right. This is because the gap is large and the hook is narrow (w is small). Following the same method presented in this report, this trapping mode can be modeled. Details are not presented here. It can be shown that the upper limit of SS bridging range is 1736rpm (with a 30° advancing contact angle ϕ).

A comparison between modeling results and existing experiments and simulations are demonstrated in Table 3.1. The modeling results with a 30° advancing contact angle ϕ coincide with all existing experiments and simulations.

Table 3.1 Comparison of modeling results ($\phi = 30^\circ$) with experiments and simulations

Geometry	 Trapping without SS bridging	 SS bridging	 No trapping
Figure 3.41	Experiment 800 1500	Modeling 800 1500	Experiment 2500 3500 Modeling 2500 3500
Figure 3.2 (a)	Simulation 800	Modeling 800 1500	Simulation 1500 2500 3600 4500 Modeling 1500 2500 3600 4500
Figure 3.2 (b)	Simulation 800	Modeling 800 1500	Simulation 1500 2500 3600 4500 Modeling 1500 2500 3600 4500

3.5 Summary

It has been found that lubricating oil can be trapped in the second ring hook at low engine speeds. The trapped oil may support TDC bridging without any additional oil supply from piston third land. This newly-discovered bridging mechanism explains the low speed bridging observed in experiments. Based on the nature of this mechanism, it is named “self-sustained (SS) bridging”. In contrast, the mechanism reported in [2], [4], [6] is named “assisted bridging”. SS bridging can introduce additional oil to a liner at a typical idle speed and city driving speeds, which is the condition in which a normal automotive engine frequently operates. The additional oil constitutes a potential source of oil consumption. Thus, SS bridging is considered an undesirable phenomenon. The ideal case is that SS bridging can be avoided at all engine speeds above the idle speed. The preferred strategy for elimination of SS bridging is to avoid oil trapping. That is, to decrease the critical trapping speed to below the idle speed. It is also desirable if SS bridging occurs in a mid-low speed range.

Oil trapping, which is the prerequisite of SS bridging, is caused by the balance between surface tension and body force. Based on this, a quasi-static model of trapping has been developed. The modeling results provide guidelines for engine designers to decrease the critical trapping speed. In a typical configuration, the critical speed for oil trapping is primarily determined by the height of the hook region (d) and the tapered angle of the hook (γ). A large rounded radius in the hook (R) and a small hook depth (c) provides auxiliary contributions. However, it is not simple to decrease the critical trapping speed to below the idle speed by merely modifying the geometric parameters in a typical configuration. Additional design modifications may be needed depending on the outcomes of engine tests.

SS bridging has been modeled in a similar method as that for oil trapping. Since it is not possible to qualitatively tell whether SS bridging occurs at high speeds (but still below the critical trapping speed) or low speeds, a quantitative analysis on each design is needed. It is desirable if SS bridging occurs in a mid-low speed range.

The models are focused on eliminating oil trapping and SS bridging by way of optimizing the geometry of a second ring hook and a piston chamfer. However, a more essential approach is to restrict oil supply to a hook region. This may involve the design of a piston skirt and an OCR, which is beyond the scope of this work. It must be emphasized that the model only evaluates the risk of SS bridging at a certain engine speed. When oil supply is well controlled, the model can to some extent exaggerate the possibility of SS bridging.

Despite the limitations of the model, the modeling results coincide with existing experiments and simulations. Thus, based on the primary physics behind oil trapping and SS bridging, the model can provide helpful guidelines on the design of second ring hook and piston third land.

4 Reverse Bridging

4.1 Introduction

4.1.1 The Concept of Reverse Bridging

During an upstroke, an OCR can scrape some oil from a liner. It has been observed in both experiments and simulations that a fraction of such scraped oil can flow back to the liner after TDC. Possibly, this phenomenon can be equally detrimental as TDC bridging because additional oil is supplied to the liner near TDC. The additional oil may reach the top part of a piston-ring pack because of the difference in ring-liner conformability near TDC, as explained in Section 1.2. Based on the fact that oil from the liner reverses to the liner after being scraped, this phenomenon is named “reverse bridging”.

Reverse bridging can also occur after BDC to the oil scraped by the lower flank of a ring. However, as explained in Section 1.2, there is no remarkable difference in ring-liner conformability at two consecutive BDC's. Thus, BDC reverse bridging is not expected to substantially increase oil consumption. The focus of this work will be reverse bridging at TDC.

In Section 4.1.2 and Section 4.1.3, experimental and computational results will be presented in order to demonstrate that reverse bridging can indeed occur in real engine operations.

4.1.2 Observations in Experiments

In this section, experimental results will be presented to demonstrate that reverse bridging can indeed occur in real engine operations.

Figure 4.1 shows a few pictures taken in a high speed 2D LIF experiment at 1500 rpm conducted by Zanghi [10]. Picture (a) shows the oil distribution at TDC. The vertical bright strikes connecting the lower flank of the second ring and the upper flank of the OCR indicate that bridging is occurring. Horizontal bright strikes can be observed right above the OCR. It implies that bridging oil is scraped by the OCR, and that the scraped oil has accumulated on the upper flank of the OCR. Picture (b) to (e) show the oil distribution slightly after TDC. The horizontal bright strikes gradually become darker, indicating that oil residing on the upper OCR flank decreases. The lower ends of the vertical bright strikes gradually disconnect with the upper OCR flank. In Picture (e), almost all vertical bright strikes have disconnected with the OCR. This implies that some scraped oil follows the liner after TDC.

The scraped oil flows upwards relative to the piston only after TDC. The timing implies that it is not associated with the body acceleration. Otherwise, such upward flow should have already been occurring at TDC. Thus, it is deemed that the upward flow occurs on the liner, but not the piston third land.

The experiment indicates that reverse bridging can indeed occur in real engine operations. However, while it was commonly observed at 800rpm and 1500rpm, it was

hardly observed at higher engine speeds. Thus, reverse bridging is more pronounced at low engine speeds.

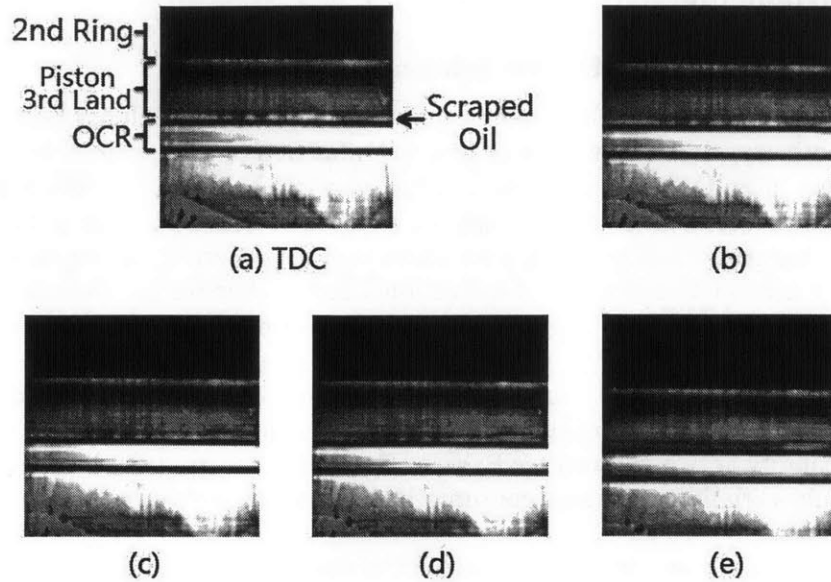


Figure 4.1 Reverse bridging observed in experiments at 1500rpm, 600mbar intake pressure. (Courtesy of E. Zanghi)

4.1.3 Observations in Simulations

In this section, simulations in a radial cross section, which was described in Chapter 2, will be reviewed. Because the purpose is to study reverse bridging, the simulation results around TDC will be focused on here.

Figure 4.2 shows the simulation results at 800rpm. In this simulation, the piston-liner clearance is 0.4mm. The simulation presented in Figure 2.5 is not used here because bridging oil fails to reach the OCR cannot be scraped by OCR in that simulation. In Figure 4.2, at -13° crank angle, bridging has already occurred. Bridging oil approaches the upper flank of the OCR, and reaches there at roughly -12° . After being scraped by the OCR, oil accumulates in the corner bounded by the liner and the upper OCR flank (See -9° crank angle.). It continues to accumulate until TDC (See 1° crank angle.), when the liner starts to move upwards relative to the piston. Then, some of the accumulated oil will follow the liner. At 8° crank angle, a thin oil film has formed on the liner. At 11° crank angle, the oil film has disconnected with the oil on the upper OCR flank. At 18° crank angle, the reverse bridging oil almost reaches the lower flank of the second ring.



Figure 4.2 Reverse bridging in simulation, 800rpm, 0.4mm piston-liner clearance, 80 μ m initial film

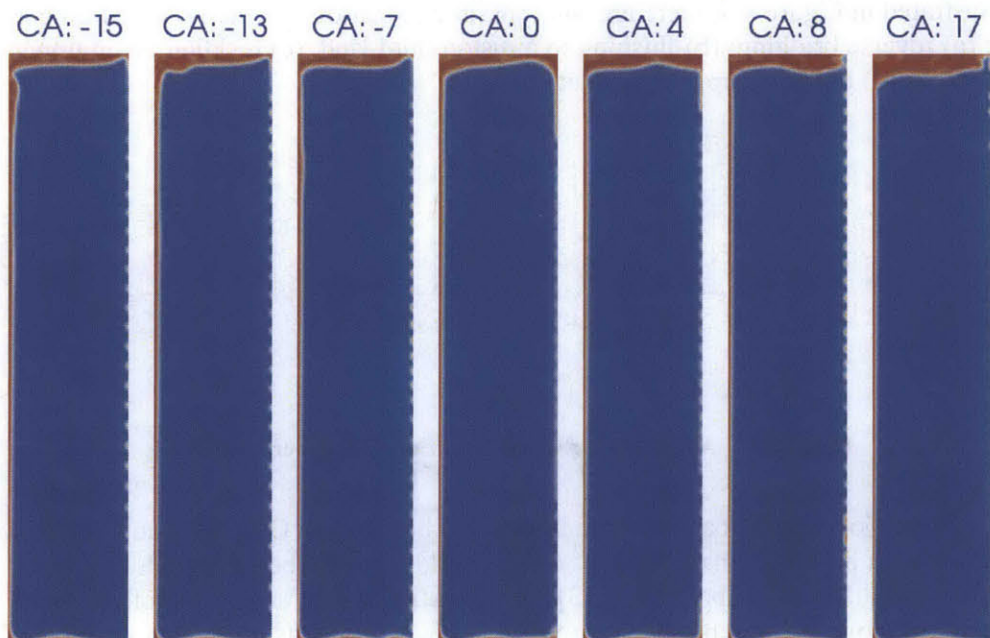


Figure 4.3 Reverse bridging in simulation, 4500rpm, 0.5mm piston-liner clearance, 30 μ m initial film

Figure 4.3 demonstrates how reverse bridging occurs at 4500rpm. It is the same simulation as was shown in Figure 2.8. The process resembles that demonstrated in Figure 4.2. At -15° , bridging has occurred. At -13° , bridging oil is scraped by the OCR. After that, oil accumulates in the bottom right corner until TDC. After TDC, a fraction of scraped oil follows the liner and breaks-up with the residual oil on the upper OCR flank.

The simulations indicate that reverse bridging can indeed occur in engine operations. They demonstrate that the upward oil flow observed in experiments, as described in Section 4.1.2, indeed occurs on a liner, but not a piston third land.

4.1.4 Fraction of Reverse Bridging

If there is no reverse bridging, all the oil scraped by an OCR in an upstroke would stay on the upper OCR flank. However, if there is reverse bridging, a fraction of scraped oil would return to the liner and become a potential source of oil consumption. Thus, it is of particular interest what a fraction of oil reverses to the liner. A small fraction is desirable because it means less oil reverses to the liner and becomes a potential source of oil consumption.

The fraction of reverse bridging, which will be denoted with γ in this report, is defined as the ratio between the quantity of reverse bridging oil and the quantity of scraped oil. That is:

$$\gamma = \frac{V_{\text{reverse bridging}}}{V_{\text{scraped}}} \quad (4.1)$$

In order to obtain γ , it must be identified where the scraped oil can possibly flow. As illustrated in Figure 4.4, there are four possible scenarios in which scraped oil ends up with: (a) reverse bridging; (b) flushing to a piston third land; (c) residing on an upper OCR flank; (d) breaking-up into droplets.

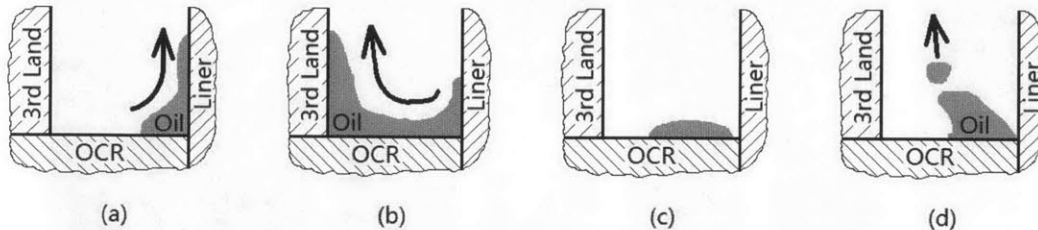


Figure 4.4 Alternative traces of oil scraped by upper OCR flank

A previous model based on the interaction between an OCR land and a liner with a certain finish predicted that $1500\mu\text{m}^2$ of oil would typically be scraped during an upstroke when there is no bridging. [13] This quantity will be taken as a reference all through this work. As will be shown in Section 4.3, simulations imply that scraped oil will not flush to the piston land or break-up into droplets when $1500\mu\text{m}^2$ of oil is scraped in an upstroke. It either resides on an upper OCR flank or reverses to the liner. This

outcome was justified by a scaling analysis as will be presented in Section 4.4. Thus, the fraction of reverse bridging defined in Equation (4.1) practically becomes:

$$\gamma = \frac{V_{\text{reverse bridging}}}{V_{\text{reverse bridging}} + V_{\text{residual}}} \quad (4.2)$$

where V_{residual} is the quantity of oil that resides on the upper OCR flank after TDC. Since a small γ is desirable, it is a preferred situation if more oil resides on an upper OCR flank.

4.1.5 Structure of This Chapter

The objective of this computational work is to physically understand reverse bridging and found out how γ varies with different variables. Particularly, this work is focused on the effect of engine speed, scraping timing, and geometric design of an upper OCR flank. In order to study the effect of scraping timing and OCR design, a total of four sets of simulations were conducted. Two types of scraping timing and two different OCR designs were attempted. Within each set, five engine speeds (800, 1500, 2500, 3600, and 4500rpm) were simulated in order to study the effects of engine speed.

In Section 4.2, the background information on the simulations will be introduced.

Then, in Section 4.3, simulation results will be presented. Within each set of simulations, only the simulations at 800rpm and 4500rpm will be described to demonstrate the differences between a low speed case and a high speed case. Then, the fraction of reverse bridging predicted by simulations at all attempted speeds will be plotted.

In Section 4.4, a scaling analysis will be presented to justify some outcomes in the simulations. The analysis will figure out where oil scraped by an upper OCR flank possibly flows.

Section 4.5 will briefly summarize this chapter.

4.2 Simulation Setup

4.2.1 Sources of Scraped Oil

In the experiments and simulations described in Section 4.1, scraped oil originates from bridging oil. However, in real engine operations, scraped oil may also come from a thin oil film on a liner. Both scenarios will be studied in this work.

In order to study the scraping of bridging oil, an oil film of uniform thickness is to be scraped from 10° crank angle BTDC to TDC in computational simulations. For simplicity, this scenario will be called “TDC scraping” in the remaining of this report.

In order to study the scraping of an oil film on a liner, a thin film with a uniform thickness is to be scraped from BDC to TDC. This scenario will be called “uniform scraping” in the remaining of this report.

The thickness of the oil film is determined by the expected quantity of scraped oil. Because of numerical errors, in the simulations, the quantity of scraped oil at TDC is usually slightly less than expected. The deficiency is typically below 4%. It is deemed that the deficiencies are within a tolerable range.

4.2.1.1 A Challenge in Simulating Uniform Scraping

If $1500\mu\text{m}^2$ of oil is to be scraped, the oil thickness on a liner is roughly 20nm. If the size of meshes near the liner is decreased to this order, the computations will take a considerable amount of time. The reason is as follows.

In order that the simulation results physically make sense, the Courant number:

$$Co = \frac{U \cdot \Delta t}{\Delta x} \quad (4.3)$$

must be less than 1. Here, U is the velocity in a computational cell, Δx is the dimension of a cell, and Δt is the time step of a computation. Thus, if some cells are extremely fine, the time step must significantly decrease. In this case, the computation will consume an increased amount of time.

In order to save computational efforts, the cells next to the liner are set to be $0.5\mu\text{m}$ wide. In these cells, the oil fraction as defined in Equation (1.5) is preset according to the expected quantity of scraped oil. An obvious drawback of this setting is that the flow field and oil interface close to the liner cannot be traced. However, the majority of the accumulated oil can be satisfactorily traced with a remarkably reduced computing effort.

4.2.2 Computational Domain

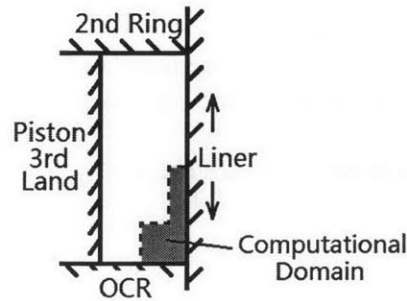


Figure 4.5 Computational domain of simulations of reverse bridging

In order to save computational efforts, the computational domain is shrunk to the vicinity of the corner bounded by a liner and an upper OCR flank. It is shown in Figure 4.5. The boundaries labeled with dashed lines are set to be free inlet or outlet. An oil inlet is preset on the top right corner of this boundary. The velocity of oil at the inlet is the same as the liner. In order to ensure that oil accumulated on the OCR does not exceed the dashed boundaries, the dimensions of the computational domain were adjusted to the quantity of scraped oil. One obvious drawback of a shrunk computational domain is that the cavity flow of gas cannot be fully simulated. However, it is assumed that the flow pattern of gas will not significantly affect the oil flow.

4.2.3 Variables to be Studied

Given the pattern (including timing and distribution) of scraping, the fraction of reverse bridging γ is dependent of the following variables:

1. Engine speed;
2. Quantity of scraped oil;
3. Oil properties including density, viscosity and surface tension;
4. Gas properties including density and viscosity;
5. Body acceleration, which depends on crank radius and connecting rod length;
6. Geometry of OCR. Typically, it involves the tapered chamfer angle ϕ of an upper OCR flank as shown in Figure 4.6.

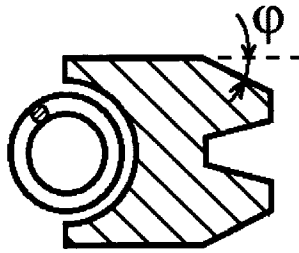


Figure 4.6 Tapered angle ϕ of upper OCR flank (Not to scale)

Similar to Chapter 2, the effect of gas flow is assumed negligible in this work. Furthermore, this work focuses on the design of piston-ring pack and the effects of crank radius and connecting rod length will not be studied. If one applies dimensional analysis, three variables can be omitted in an experimental or computational study. Here, the oil properties are selected as the repeating variables. Then, the variables to be studied in this work are the effects of engine speed N , quantity of scraped oil V_{scraped} , and tapered angle of upper OCR flank ϕ .

4.3 Simulation Results

In order to study the effects of a tapered angle on an upper OCR flank, two types of designs were studied in the simulations: one with a non-tapered upper OCR flank ($\phi = 0$), and one with $\phi = 18^\circ$. The latter one is the same as the OCR tested in the high speed 2D LIF experiments [10].

First, a simulation of uniform scraping with a non-tapered OCR at 800rpm will be introduced as an example in Section 4.3.1. The observations will first be described and the physics behind will then be explained in detail. Then, simulations in other conditions will be described compared to the example.

In Section 4.3.2, simulation results of uniform scraping with a non-tapered OCR flank will be shown. In Section 4.3.3, TDC scraping with a non-tapered OCR flank will be discussed to demonstrate the effect of scraping timing. The simulations with an 18° tapered OCR will be described in Section 4.3.4 and 4.3.5. In all these sections,

simulations results at 800rpm and 4500rpm will be presented to demonstrate the oil flow pattern at a low engine speed and a high engine speed, respectively. Then, the fraction of reverse bridging extracted from simulations will be shown.

In all the simulations to be described, red color signifies oil, and blue color signifies gas. The expected scraping quantities are all $1500\mu\text{m}^2$

4.3.1 An Example: Uniform Scraping by Non-Tapered OCR at 800rpm

4.3.1.1 Observations in Simulations

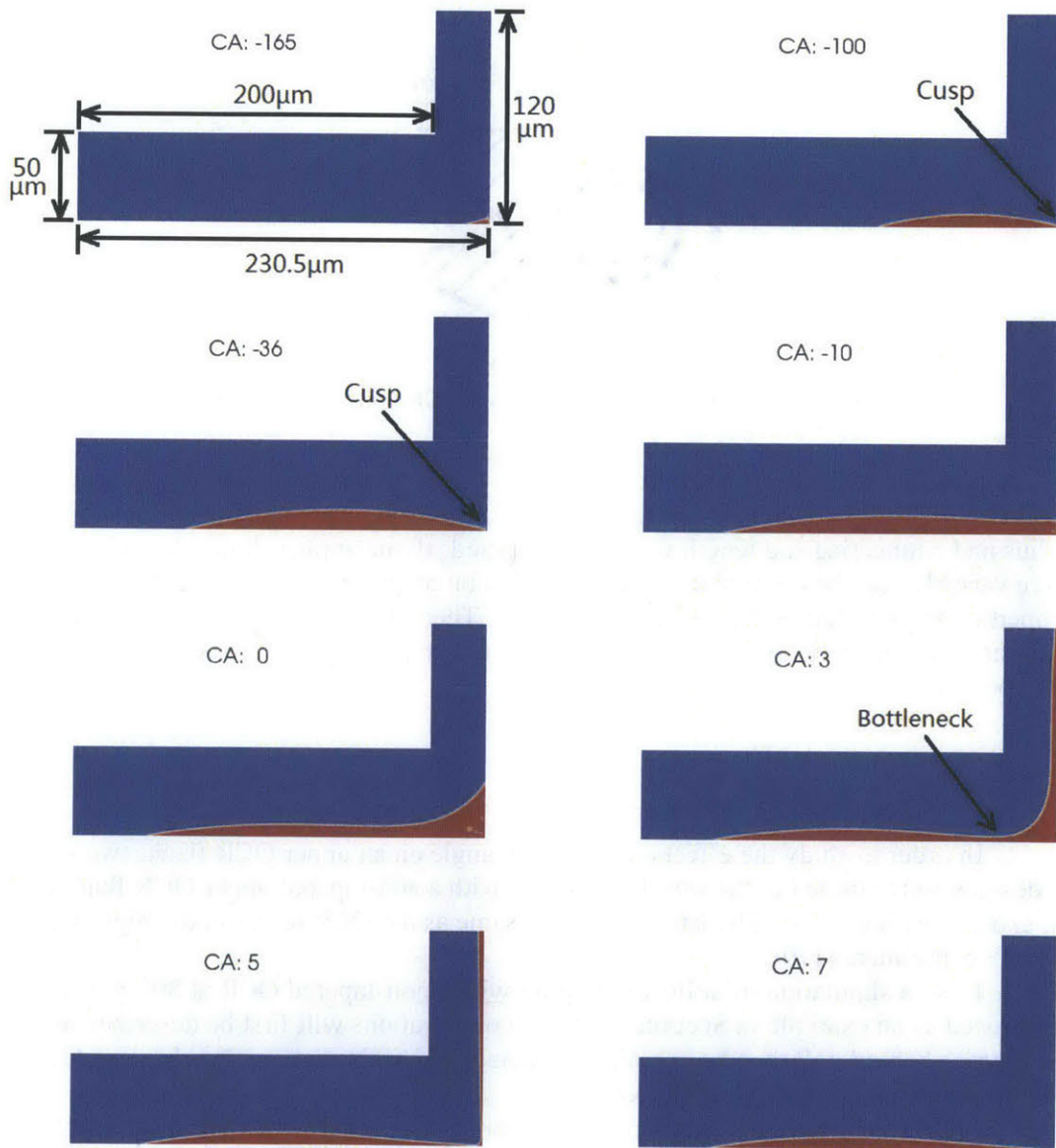


Figure 4.7 Uniform scraping and reverse bridging, non-tapered OCR, 800rpm, $V_{\text{scraped}} \approx 1500 \mu\text{m}^2$

Figure 4.7 shows how the oil that is uniformly scraped by a non-tapered OCR evolves at 800rpm. The expected scraping quantity is $1500\mu\text{m}^2$.

At -165° crank angle, scraped oil has been accumulating in the corner bounded by the upper OCR flank and the liner.

However, starting from roughly -150° , oil can no longer accumulate in the vicinity of the corner. As can be observed in the snapshots of -100° and -36° , oil cannot wet the liner although there is an invisibly thin oil layer on it. The oil-gas interface almost originates from the corner. This actually results from a tiny cusp in the oil-gas interface, which will be explained in Section 4.3.1.2. As being scraped, the oil spreads along the upper OCR flank in the form of a puddle.

At roughly -10° crank angle, the cusp near the corner gradually disappears. The scraped oil tends to wet the liner. As a result, at 0° crank angle, a circular oil-gas interface profile appears near the liner.

After TDC, scraped oil is separated into two parts, one follows the liner, and one stays on the upper OCR flank. At 3° crank angle, a bottleneck of oil tends to form on the upper OCR flank. At 5° crank angle, the bottleneck has already formed, and the two parts of oil has been separated by the bottleneck. At 7° crank angle, reverse bridging oil has been dragged away, and the residual oil has been left on the upper OCR flank.

After this primary reverse bridging process, the residual oil will slowly move towards the liner because of gas flow. The contact line near the liner will touch the liner, and some oil near the contact line will be dragged away by the liner. This occurs all through a down-stroke. However, the quantity of oil that is dragged away by such secondary reverse bridging process is very small. The secondary process is actually evidenced by the decrease in the integration of oil fraction (See Equation (1.5)), but not observed in most of the simulation videos. Since there is no difference in ring-liner conformability in the middle and bottom part of a stroke (See Section 1.2), a reverse bridging away from TDC may not be as detrimental as a reverse bridging near TDC. Thus, the fraction of reverse bridging during the primary process is of more practical significance.

4.3.1.2 Discussions

Cusp in Oil-Gas Interface

In this section, it will be explained that a tiny cusp actually forms in the vicinity of the corner formed by an upper OCR flank and a liner. The cusp is too tiny to be observed in Figure 4.7. Thus, it appears that the oil-gas interface almost originates from the corner.

In order to capture the oil flow in the immediate vicinity of the corner, another simulation in a tiny region near the corner was conducted. The results are shown in Figure 4.8. Figure 4.8 (a) shows the oil distribution near the corner. Because of the decreased computational domain, the thin oil film on the liner is observable. A cusp forms in the oil-gas interface where the oil film on the liner is dragged into the accumulated oil.

If such a cusp does not exist, oil would tend to wet to the liner as shown by the grey region in Figure 4.9. However, the existence of this cusp effectively pushes oil away

from the liner. From a larger scale, the oil-gas interface resembles the dashed black curve in Figure 4.9.

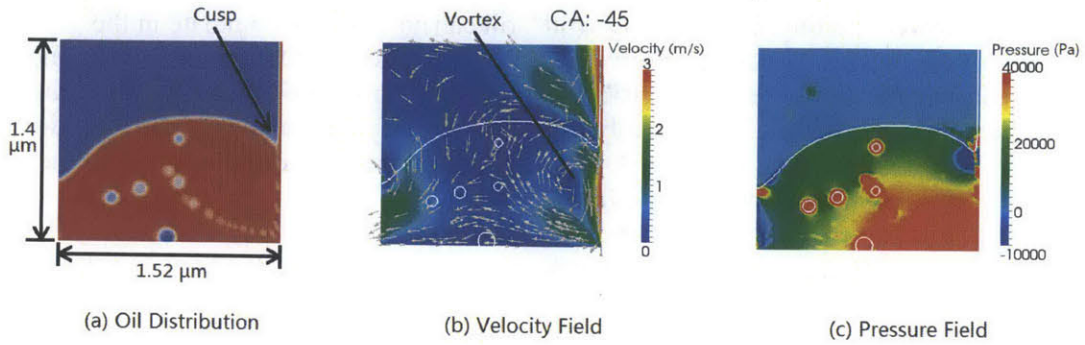


Figure 4.8 Cusp in oil-gas interface near the corner bounded by upper OCR flank and liner

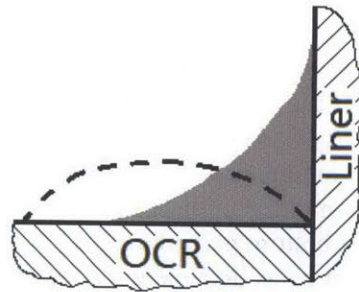


Figure 4.9 Effect of cusp (Grey: oil without cusp; dashed black curve: oil surface with cusp)

The cusp is primarily caused by the downward shear stress due to the injecting oil film. [14], [15] As illustrated in Figure 4.10, the viscous shear stress τ is balanced by the Laplace pressure due to surface tension [14], [15], that is:

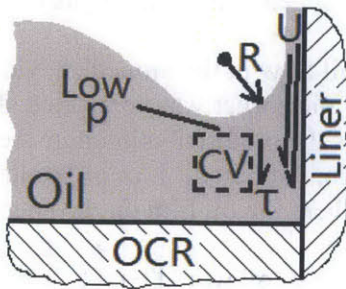


Figure 4.10 Force balance on the control volume below cusp

$$\frac{\sigma}{R} \sim \mu \frac{U}{H} \quad (4.4)$$

where σ is surface tension, μ is oil viscosity, R is radius of the cusp, H is thickness of oil layer on liner, and U is instantaneous velocity of the liner. The left hand side is a rough scaling of Laplace pressure, and the right hand side is a rough scaling of viscous stress. Equation (4.4) gives:

$$R \sim \frac{\sigma H}{\mu U} \quad (4.5)$$

which indicates that the radius decreases with liner speed. That is, the cusp is sharper when the velocity of the liner is greater. This explains why no cusp is observed near BDC when the liner velocity is still small. It only starts to appear when the velocity of liner becomes larger in the middle of a stroke. As the liner velocity becomes small near TDC, the cusp disappears again. As a result, the oil-gas interface tends to recover to the quasi-static profile illustrated by the grey region in Figure 4.9. Although it cannot reach the equilibrium state because of the limited time, such an interface recovery process distributes an increased fraction of oil near the liner.

Figure 4.8 (a) also indicates that gas is entrained through the cusp.

Figure 4.8 (b) shows the velocity field near the corner. The injected oil layer will not spread immediately after it enters the oil accumulated on the upper OCR flank. Instead, it will flow straight to the corner and deflect there. A vortex, which is clockwise in Figure 4.8 (b), is formed in the oil so that the oil-gas interface does not follow the streamlines of the injecting oil.

Figure 4.8 (c) shows the pressure field near the corner. Pressure in the majority of gas is assumed to be 0. The oil layer on the liner will drag the gas right next to the oil-gas interface. The dragged gas bears a velocity and will impact on the surface of accumulated oil. Thus, the gas pressure in the cusp is large. However, according to [14], [15], the cusp mainly results from viscous effect of oil, and the large gas pressure has only a secondary effect.

Up to this point, it has been explained how the cusp is generated, and how it is relevant to the interface recovery.

Spreading of Outer Contact Line

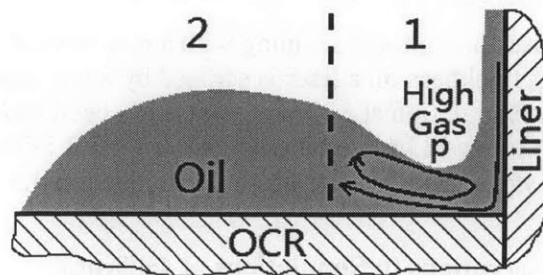


Figure 4.11 Two regions of oil as oil accumulates

The accumulated oil can be divided into two regions as shown in Figure 4.11.

Region 1 is in the vicinity of the cusp in oil-gas interface. There is considerable viscous dissipation in this region.

Region 2 is located away from the liner. In this region, the high pressure near the singularity, which is the corner formed by the upper OCR flank and the liner, almost dies out. Thus, oil spreading is primarily driven by surface tension. Since oil velocity is very small and gas pressure is fairly uniform in this region, the profile of oil-gas interface can be estimated by a quasi-static analysis as demonstrated in Chapter 2 and 3. Such an analysis can predict how far the outer contact line reaches.

In order to apply such an analysis, a matching between the two regions is necessary. However, a quantitative model on region 1 is still missing. It is a suggested topic for future research. Furthermore, oil needs time to reach a static equilibrium. Thus, a quasi-static analysis may not be valid at a high engine speed.

Oil Separation after TDC

As shown in Figure 4.7, after TDC, the liner will drag some scraped oil. The scraped oil can be divided into two parts:

1. Oil near the liner can be affected by the viscous force due to the liner motion. Because of the low pressure in the corner, there exists a pressure force in the accumulated oil. Thus, some oil that is relatively far away from the liner can be driven towards the liner, and then be dragged away by the liner;
2. Oil far away from the liner can neither be dragged by the viscous force, nor be pushed by the pressure force. Surface tension will balance the upward body force. Thus, this part of oil will stay on the upper OCR flank.

Obviously, if more oil flows into the first part, the fraction of reverse bridging will be larger. The fraction between these two parts depends on the interface recovery process. If the oil-gas interface recovers to a larger extent, more oil will be distributed near the liner at TDC. Thus, more oil will be dragged away by the liner and the fraction of reverse bridging will be larger.

Thus, the fraction of reverse bridging mainly depends on the recovery of oil-gas interface.

4.3.2 Uniform Scraping by Non-Tapered OCR

This section focuses on uniform scraping with a non-tapered OCR flank. That is, a thin oil film of uniform thickness on a liner is scraped by a non-tapered OCR flank all through an upstroke. The simulation at 800rpm has already been shown in Section 4.3.1. Simulation result at 4500rpm will be described in Section 4.3.2.1. The fraction of reverse bridging extracted from simulations will be presented in Section 4.3.2.2.

4.3.2.1 Observations in Simulations at 4500rpm

Figure 4.13 shows the simulation result at 4500rpm with a non-tapered OCR. Qualitatively, the process resembles that at 800rpm. However, there are evident

quantitative differences. At -165° crank angle, the cusp has already formed. Compared to the snapshot at the same crank angle in Figure 4.7, it indicates that the cusp forms at an earlier crank angle at high speed. This results from the higher liner speed.

As the scraped oil spreads, the oil-gas interface is less symmetric compared to the low speed case. This is associated with the cusp, which has a more pronounced effect when the liner moves faster. Furthermore, the gas flow with an increased velocity has a secondary effect.

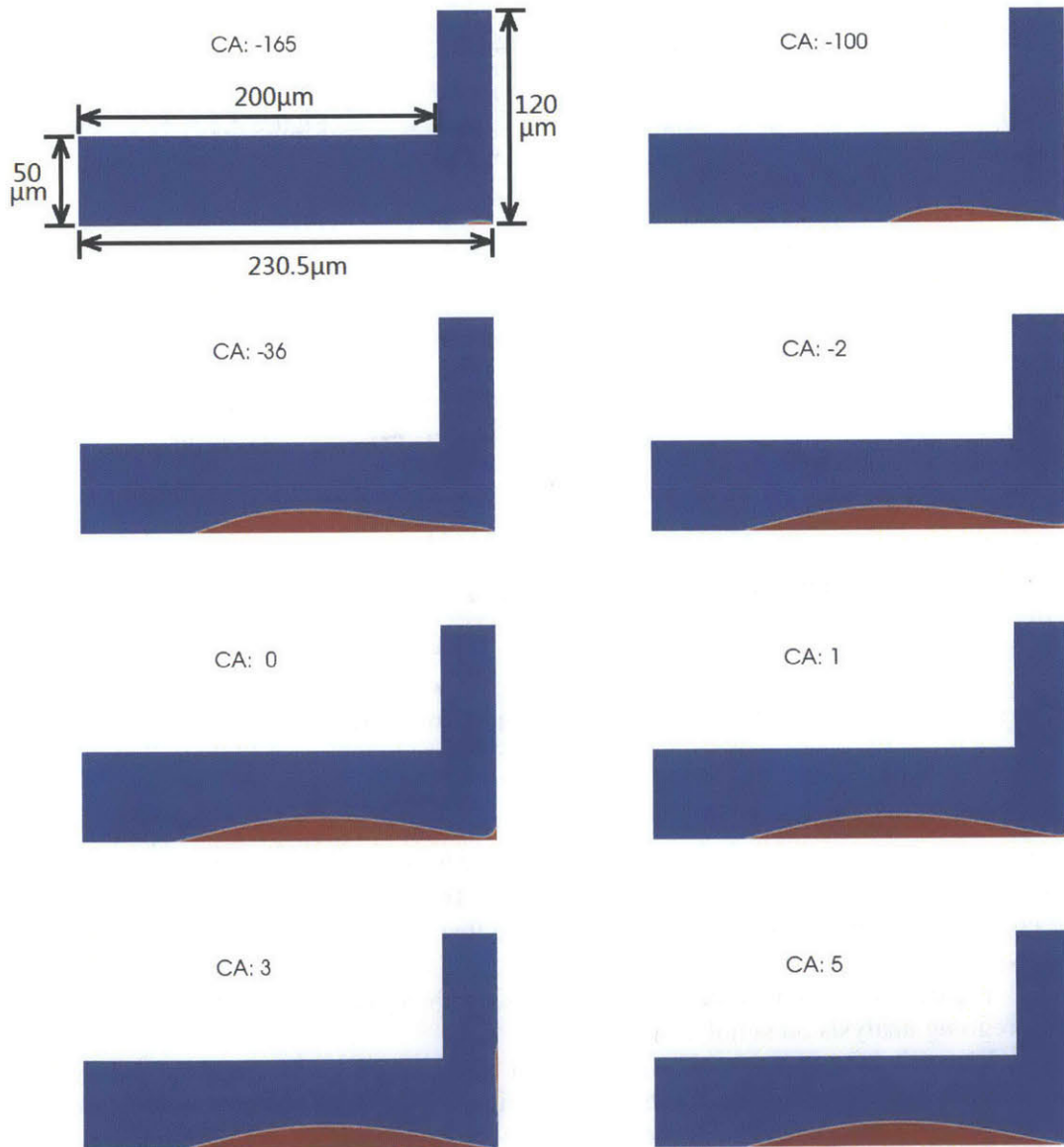


Figure 4.12 Uniform scraping and reverse bridging, non-tapered OCR, 4500rpm, $V_{\text{scraped}} \approx 1500 \mu\text{m}^2$

At 4500rpm, the interface recovery does not initiate until roughly -2° crank angle. This is because the liner velocity becomes sufficiently small at a later crank angle. Thus, the oil interface recovers within less crank angles. Furthermore, at a higher engine speed, the time duration of one crank angle is shorter. Thus, the time allowed for interface recovery is substantially shorter at a higher engine speed. Resultantly, less oil will be distributed in the vicinity of the liner, and less oil reverse bridges. This is true according to the last four snapshots in Figure 4.13. Because the quantity of reverse bridging oil decreases, they are dragged away within a shorter time.

4.3.2.2 Fraction of Reverse Bridging

Simulations were conducted with $V_{\text{scraped}} \approx 500, 1000, 1500, 3000, 4500, 6000, 10000 \mu\text{m}^2$. All the simulation results resemble Figure 4.7 and Figure 4.12. Thus, the variation of fraction of reverse bridging can be explained in a similar manner. They all depend on the oil-gas interface recovery process.

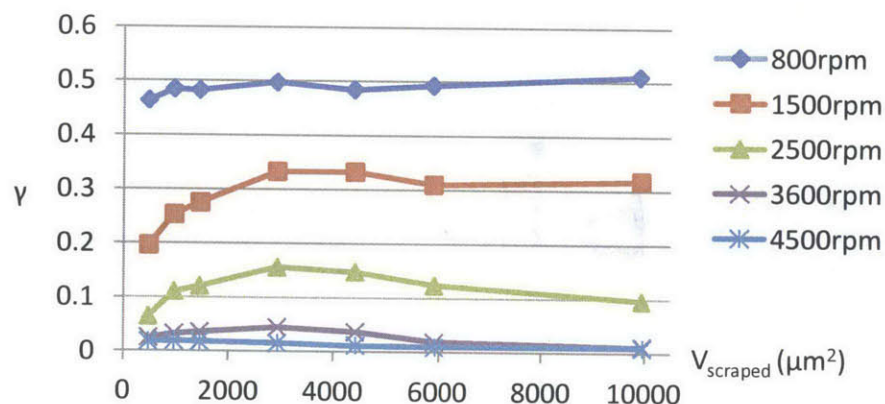


Figure 4.13 Fraction of reverse bridging γ against quantity of scraped oil, uniform scraping, non-tapered OCR flank

Figure 4.13 shows how the fraction of reverse bridging γ varies with quantity of scraped oil. No general trend has been found. At each speed, γ varies in a relatively small range. The range of variation can be comparable to the range of numerical errors. Thus, for engineering applications, it can be considered that γ is approximately a constant in V_{scraped} .

Figure 4.13 also indicates that γ decreases with engines speed. This coincides with the foregoing analysis on simulation results.

Figure 4.14 shows how γ , averaged over V_{scraped} , varies with engine speed N . As can be observed, γ decreases with engine speed in an exponential manner. It indicates that reverse bridging is much more pronounced at lower engine speeds, which coincides with experimental results. Above 3500rpm, γ is almost zero, which means only a little oil will reverse to the liner. Thus, reverse bridging is not an outstanding issue at high engine speeds.

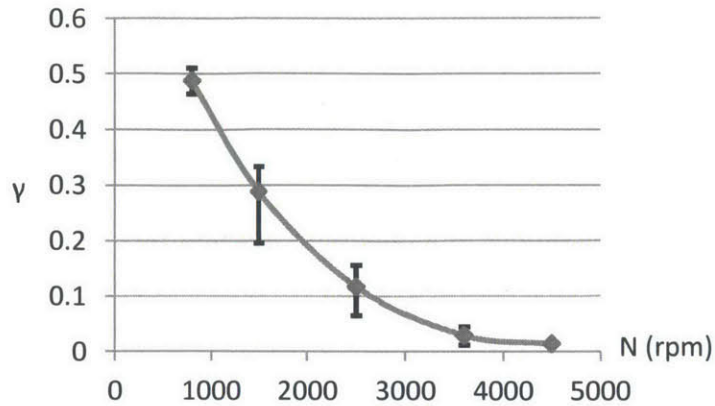


Figure 4.14 Fraction of reverse bridging γ against engine speed N , uniform scraping, non-tapered OCR flank

4.3.3 Scraping of Bridging Oil by Non-Tapered OCR

This section focuses on TDC scraping with a non-tapered OCR flank. That is, oil on a liner with a uniform thickness is scraped from -10° crank angle to TDC.

In Section 4.3.3.1 and 4.3.3.2, simulation results at 800rpm and 4500rpm will be described, respectively. In each simulation, roughly $1500\mu\text{m}^2$ of oil is scraped. In Section 4.3.3.3, the fraction of reverse bridging will be shown.

4.3.3.1 Observations in Simulations at 800rpm

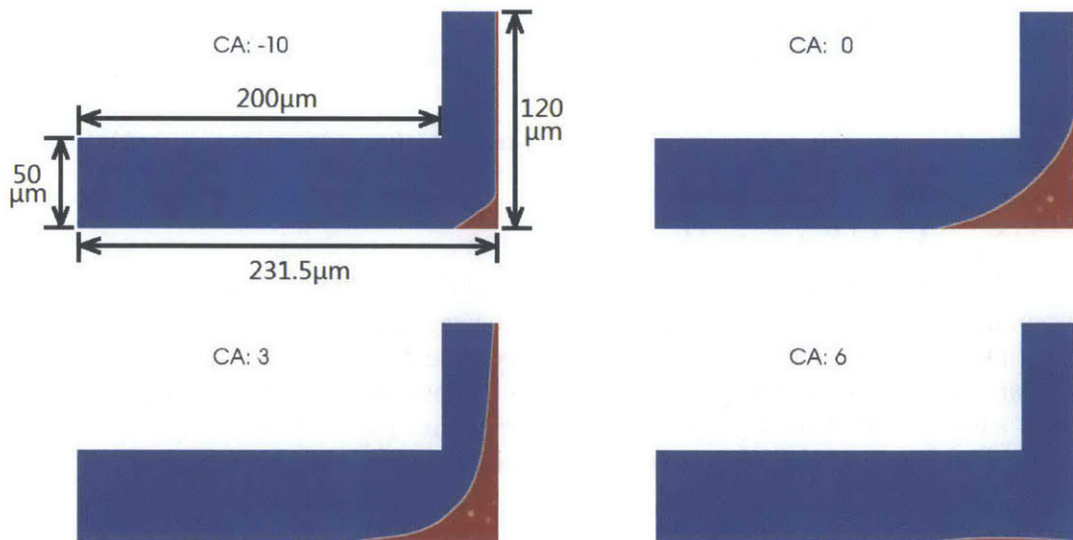


Figure 4.15 TDC scraping and reverse bridging, non-tapered OCR, 800rpm, $V_{\text{scraped}} \approx 1500 \mu\text{m}^2$

Figure 4.15 shows the simulation results at 800rpm. Because the liner velocity is small near TDC, cusp does not form near the corner.

The scraped oil does not have sufficient time to spread along the OCR flank. Thus, compared to uniform scraping all through an up-stroke, more oil is distributed near the liner at TDC. Thus, a larger fraction of reverse bridging is expected.

4.3.3.2 Observations in Simulations at 4500rpm

Figure 4.16 shows the simulation results at 4500rpm. Before -5° crank angle, a cusp can be observed because of the higher liner speed. The cusp pushes more oil away from the liner. (See Figure 4.9.) However, at a higher engine speed, less time is allowed for oil spreading. Thus, it is not obvious how γ would vary with engine speed. Computational results need to be referred to.

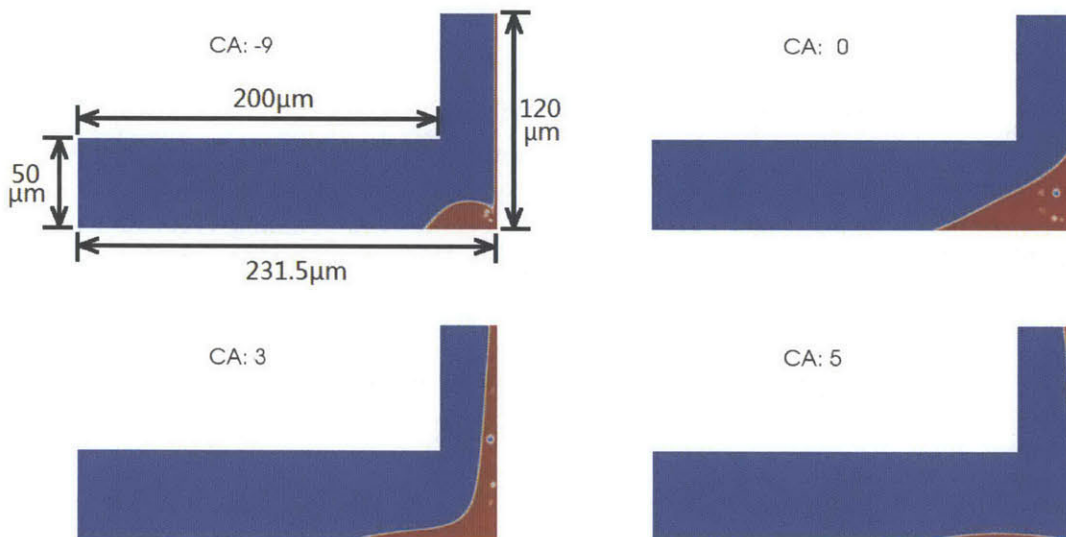


Figure 4.16 scraping and reverse bridging, non-tapered OCR, 4500rpm, $V_{\text{scraped}} \approx 1500 \mu\text{m}^2$

4.3.3.3 Fraction of Reverse Bridging

Figure 4.17 plots the fraction of reverse bridging for TDC scraping. Approximately $1500 \mu\text{m}^2$ of oil is scraped in these simulations. For TDC bridging, γ of also tends to decrease with engine speed. However, the decreasing rate is much slower. Compared to uniform scraping, γ of bridging oil is substantially greater at each engine speed, which results from the lack of time for spreading. The fraction is larger than 0.8 even at high speeds. Thus, reverse bridging of bridging oil is a practical issue at all engine speeds. This further explains why TDC bridging is an undesirable phenomenon.

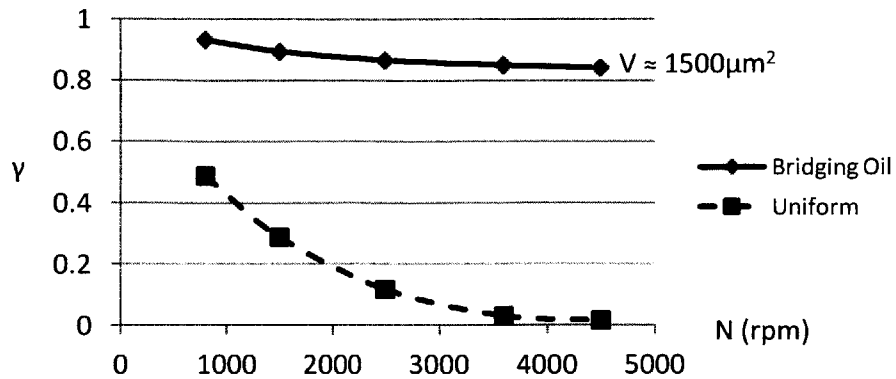


Figure 4.17 Fraction of reverse bridging γ against engine speed N , TDC scraping, non-tapered OCR flank

4.3.4 Uniform Scraping by Tapered OCR

In this section, the effects of a tapered upper OCR flank will be studied. In the simulations, oil is uniformly scraped all over an upstroke by an 18° tapered OCR.

Simulation results at 800rpm and 4500rpm will be demonstrated in Section 4.3.4.1 and 4.3.4.2, respectively. A comparison between them will demonstrate the effect of engine speed. Then, the fraction of reverse bridging will be shown and briefly discussed in Section 4.3.4.3.

4.3.4.1 Observations in Simulations at 800rpm

Figure 4.19 demonstrates the simulation results at 800rpm. The complete process appears similar to scraping by a non-tapered OCR, as shown in Figure 4.7.

An essential difference between a non-tapered OCR flank and a tapered one is that the component of body force that is parallel to the OCR flank will affect oil spreading. As shown in Figure 4.18, a downward body force resists oil spreading, but an upward body force favors body spreading. However, the simulations indicate that the difference in spreading distances on a tapered and non-tapered OCR flank is not obvious.

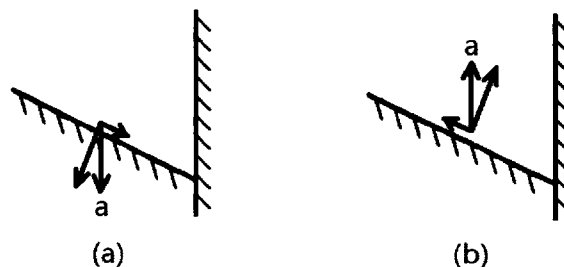


Figure 4.18 Components of body force. (a): downward body force; (b) upward body force

An obvious cusp is not observed until roughly -130° crank angle, which is later than that with a non-tapered OCR. Furthermore, the cusp starts to disappear at roughly -17° crank angle, which is earlier. This indicates that a tapered angle suppresses cusp formation. A direct consequence is that oil owns more time to recover its interface before TDC.

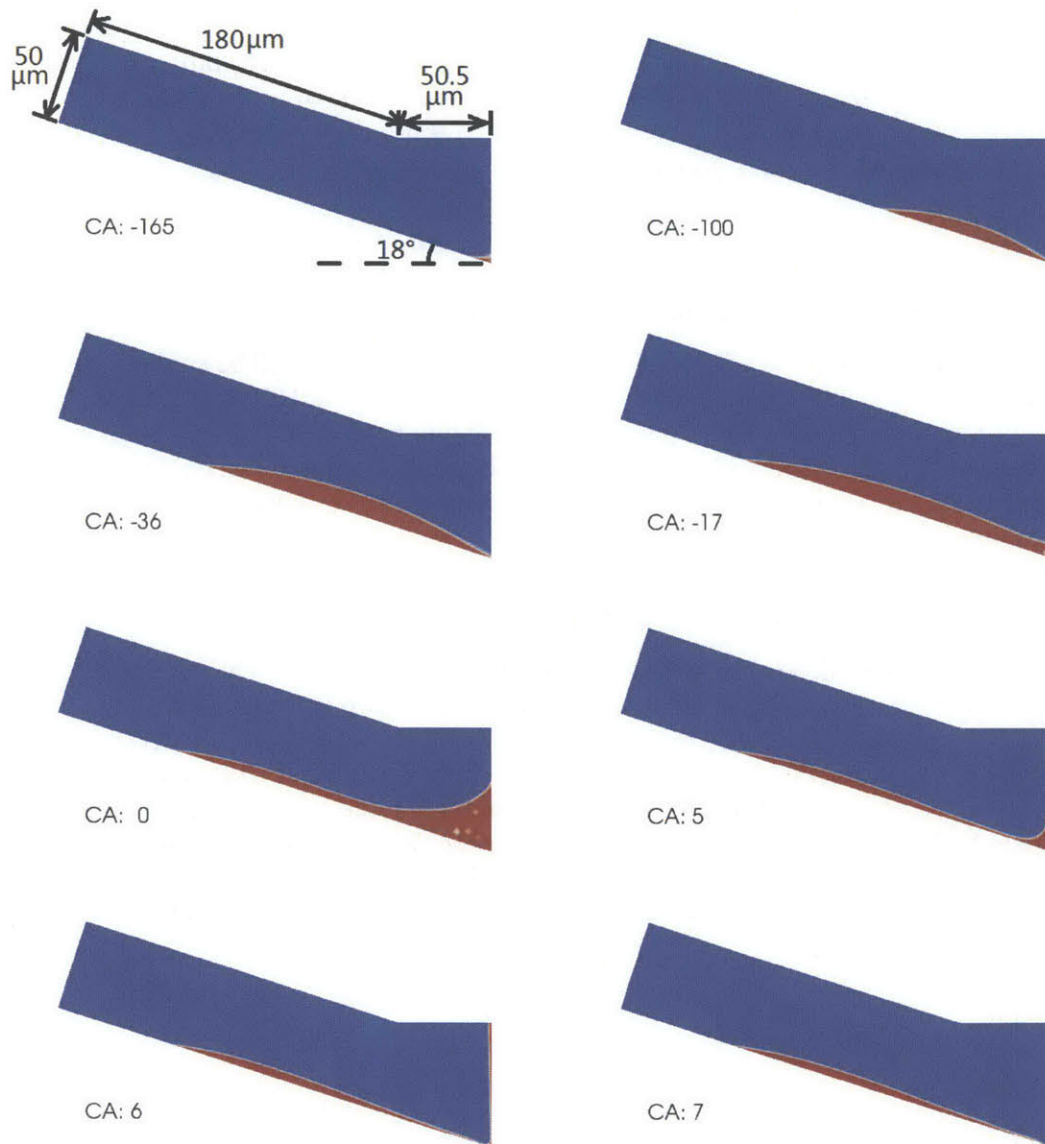


Figure 4.19 Uniform scraping and reverse bridging, 18° tapered OCR, 800rpm, $V_{\text{scraped}} \approx 1500 \mu\text{m}^2$

As shown in the snapshot at 0° crank angle in Figure 4.19, as the oil-gas interface recovers, the sharper angle tends to enclose more oil near the liner. Both the tapered angle and the longer recovery time determine that a larger fraction of oil reverses to the liner.

The reason why a tapered angle suppresses cusp formation will be briefly explained in this paragraph. According to Moffatt's theory [16], the pressure in the vicinity of the corner increases when the wedge becomes sharper. The increased pressure contributes to balancing the downward viscous force and push the oil-gas interface outwards. Thus, a cusp is less likely to form.

4.3.4.2 Observations in Simulations at 4500rpm

Figure 4.20 shows the simulation results at 4500rpm. Again, the cusp occurs earlier and disappears later compared to low speed cases. But compared to a non-tapered OCR, the cusp occurs later and disappears earlier with a tapered OCR at a same engine speed.

Before the body force changes direction, it is obvious that the oil spreads slower than on a non-tapered OCR. It indicates that, at a higher engine speed when body acceleration is larger, the resisting effect of the downward body force becomes more outstanding. After the body acceleration switches direction, the distance that oil spreads is still shorter than that on a non-tapered flank.

As can be observed in the snapshot at 0° crank angle, the majority of oil is distributed away from the corner. This probably results from the large upper body force. It may also results from the great oil pressure in the corner [16], which drives oil away from the corner. Furthermore, less time is allowed for the recovery process at a higher engine speed. Thus, when the oil-gas interface recovers, despite the sharp corner, only a little oil can be entrained in the corner. Resultantly, it is possible that the fraction of reverse bridging decreases with a tapered angle at high engine speeds.

A comparison between the simulations at a low speed and a high speed indicates that, with a tapered chamfer on an OCR flank, the fraction of reverse bridging depends on two competing mechanism: 1) the wedge near the corner tends to enclose more oil as oil-gas interface recovers; 2) more oil is distributed away from the liner because of upward body force and/or larger pressure in the corner. At low engine speeds, the first mechanism, which favors reverse bridging, dominates. At high engine speeds, it is not simple to pre-determine which one is dominant. Simulation results have to be referred to.

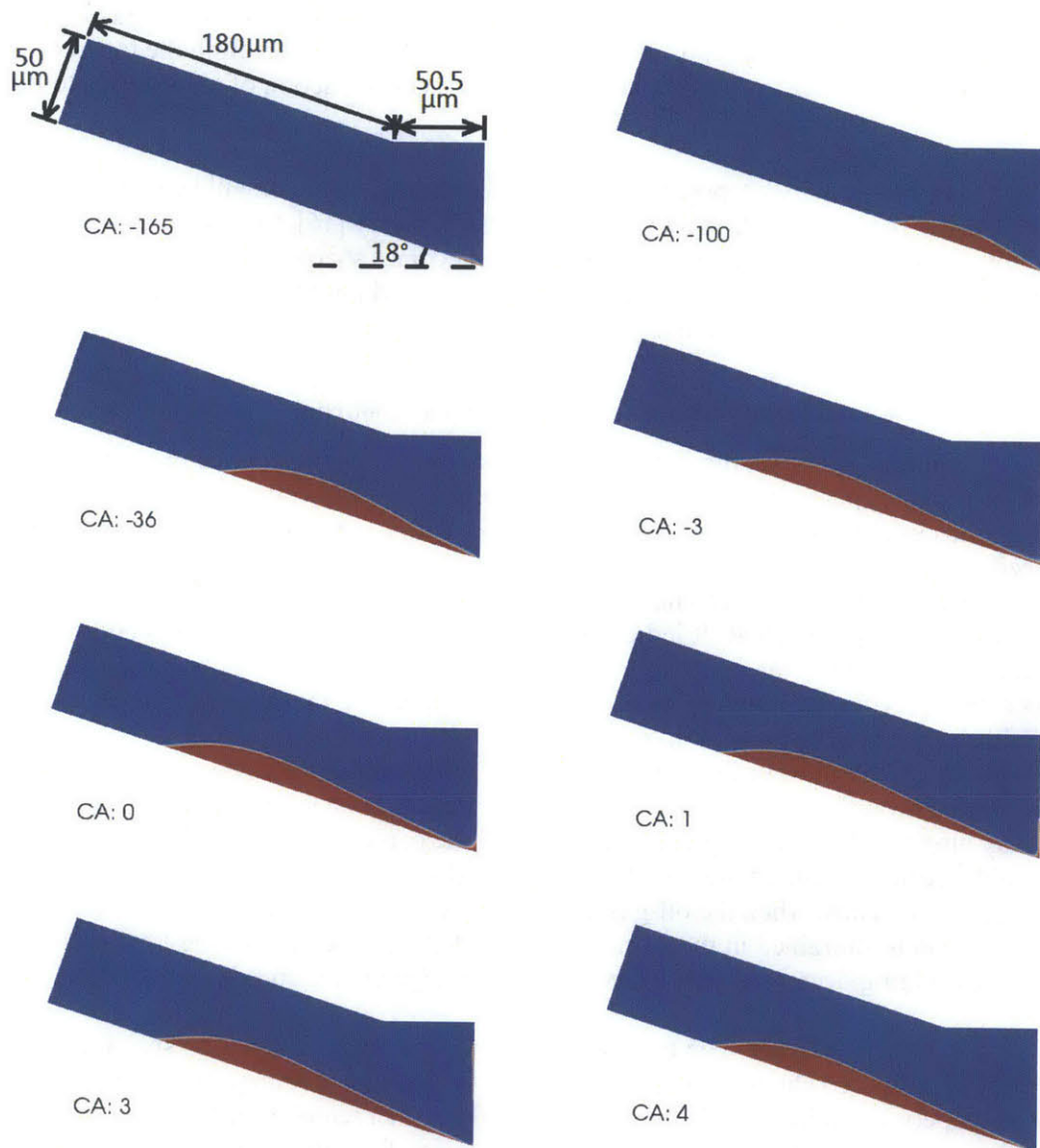


Figure 4.20 Uniform scraping and reverse bridging, 18° tapered OCR, 4500rpm, $V_{\text{scraped}} \approx 1500 \mu\text{m}^2$

4.3.4.3 Fraction of Reverse Bridging

Figure 4.21 shows how γ varies with engine speed with an 18° tapered OCR. Two sets of simulations were conducted, one with $V_{\text{scraped}} \approx 1500 \mu\text{m}^2$, and the other $3000 \mu\text{m}^2$. The averaged γ with a non-tapered angle is also plotted for comparison. As expected, γ is increased by the tapered angle at low engine speeds. This is the case below roughly 1800rpm. Between roughly 1800rpm and 3500rpm, γ is decreased, indicating that the

overwhelming factor switches to the biased oil distribution. Above 3500rpm, γ is practically 0 and it is not very meaningful to compare the variation of results.

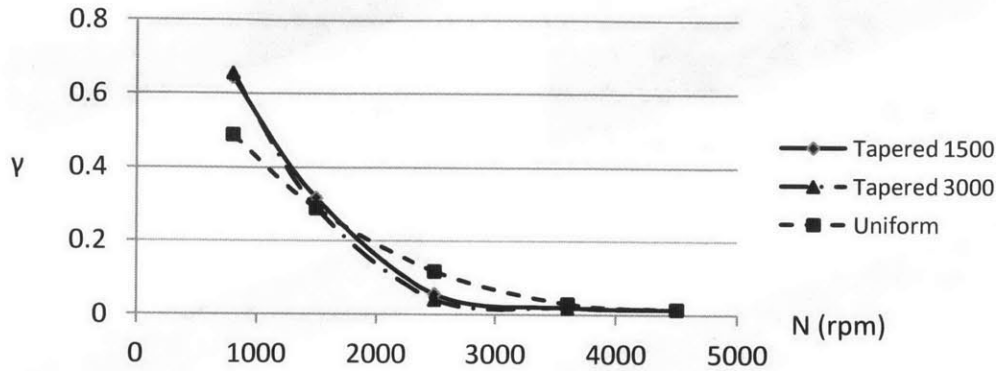


Figure 4.21 Fraction of reverse bridging γ against engine speed N , uniform scraping, 18° tapered OCR flank

Since a high fraction of reverse bridging is undesirable, a tapered angle in OCR flank is detrimental at low engine speeds, but beneficial at middle speeds. However, since the fraction of reverse bridging decreases with engine speed in all designs, its occurrence at low speeds is of more practical concern. Furthermore, automotive engines for civil use frequently operate at city driving speeds, which are typically below 2000rpm. Hence, in terms of reverse bridging, a tapered angle is considered detrimental in general.

4.3.5 Scraping of Bridging Oil by Tapered OCR

In this section, the scenario in which an 18° tapered OCR scrapes oil before TDC is to be studied. All simulations started at -10° crank angle and the upper OCR flank scrapes a uniform oil film on the liner. The results are to be compared with TDC scraping by a non-tapered OCR in order to reveal the effect of a tapered angle.

In Section 4.3.5.1 and 4.3.5.2, simulations results at 800rpm and 4500rpm will be presented, respectively. In Section 4.3.5.3, the fraction of reverse bridging predicted from simulation results will be shown and discussed.

4.3.5.1 Observations in Simulations at 800rpm

Figure 4.22 shows the simulation results at 800rpm. No cusp forms at this low engine speed. Since the oil does not have sufficient time to spread out, most oil is accumulated in the vicinity of the corner. Thus, the effect that a wedge encloses more oil is more outstanding. Thus, compared to a non-tapered OCR, the fraction of reverse bridging is expected to be larger.

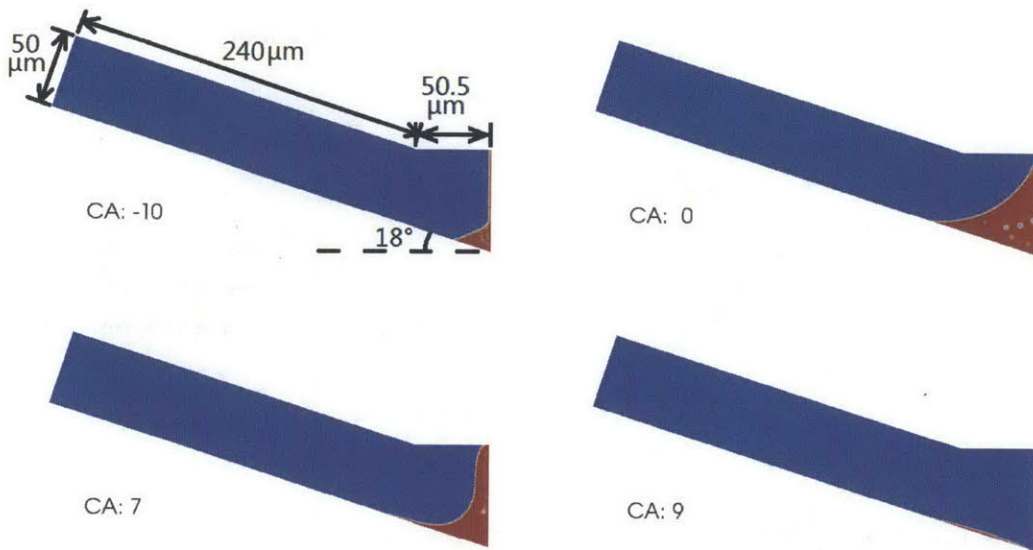


Figure 4.22 TDC scraping and reverse bridging, 18° tapered OCR, 800rpm, $V_{scraped} \approx 1500 \mu\text{m}^2$

4.3.5.2 Observations in Simulations at 4500rpm

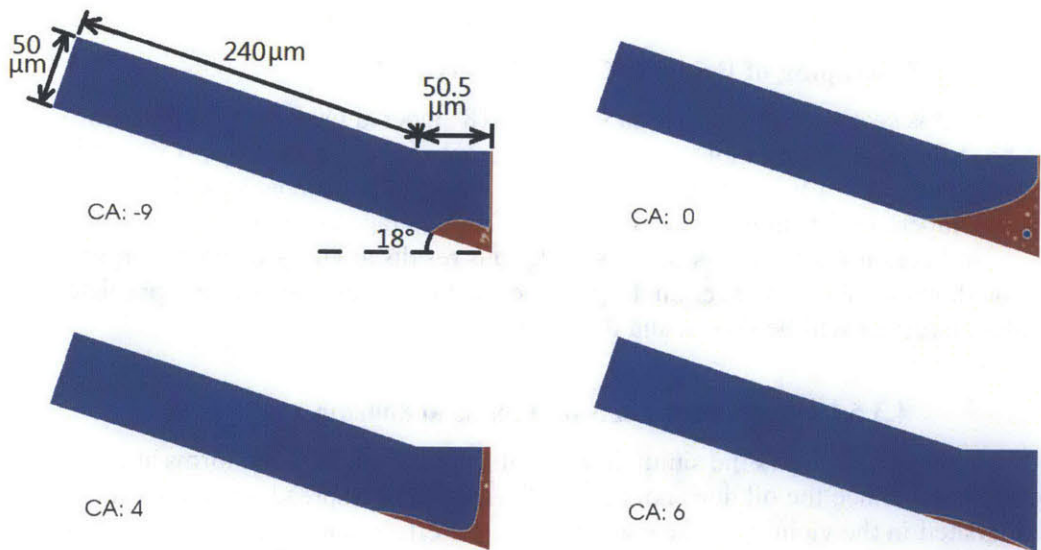


Figure 4.23 TDC scraping and reverse bridging, 18° tapered OCR, 4500rpm, $V_{scraped} \approx 1500 \mu\text{m}^2$

Figure 4.23 shows the simulation results at 4500rpm. A cusp can be observed because of larger velocity of the liner. The cusp contributes to push the oil outwards.

Moreover, compared to a low speed case, the larger body acceleration also contributes to oil spreading. Thus, the outer contact line of oil reaches farther compared to the low speed case, though it owns less time to spread. However, compared to a non-tapered OCR, oil is mostly accumulated near the liner. Thus, the enclosure effect of the wedge should still be more outstanding than the spreading effect. A larger fraction of reverse bridging is expected.

4.3.5.3 Fraction of Reverse Bridging

Figure 4.24 shows how the fraction of reverse bridging γ varies with engine speed with an 18° tapered OCR scraping oil before TDC. As expected, γ decreases with engine speed, and increases with the tapered angle. At all engine speeds, γ is greater than 0.85, which indicates that reverse bridging of bridging oil is a practical issue at all engine speeds.

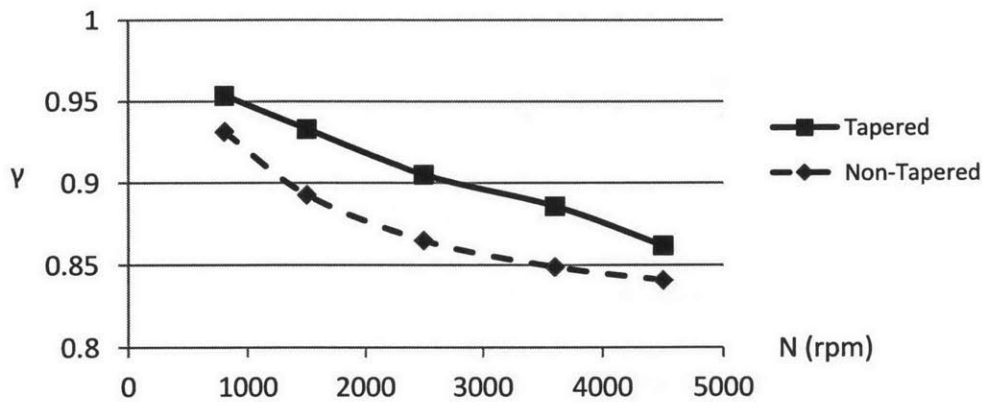


Figure 4.24 Fraction of reverse bridging γ against engine speed N , TDC scraping, 18° tapered OCR flank

4.4 Alternative Traces of Scraped Oil

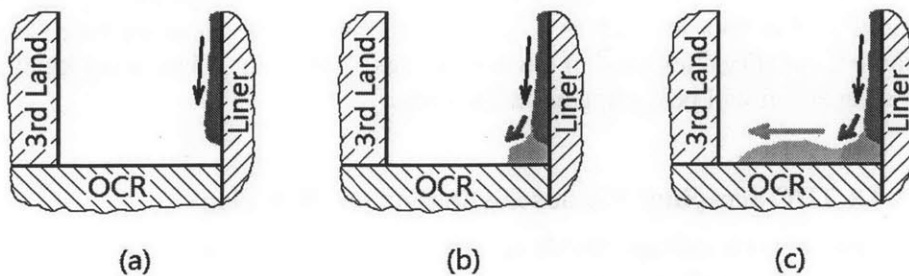


Figure 4.25 Possible flow patterns of scraped oil

In all the simulations, oil does not flush to the piston or break-up into droplets. A justification from a perspective of energy will be presented in this Section.

As demonstrated in Figure 4.8, despite the existence of accumulated oil, scraped oil will still flow through the corner bounded by a liner and an upper OCR flank. As illustrated in Figure 4.25 (a) and (b), the oil will lose a fraction of its kinetic energy in the corner because of viscous dissipation. If the oil retains sufficient kinetic energy after exiting the corner, it can flow along the upper OCR flank. (See Figure 4.25 (c).) Viscous dissipation will consume kinetic energy in this process, too. The oil is able to reach the piston land only if it bears sufficient kinetic energy to overcome the viscous dissipation during these two stages of viscous dissipation.

4.4.1 Uniform Scraping: Viscous Dissipation in Corner

In the corner, the viscous dissipation is dependent of Reynolds number [16]:

$$Re = \frac{Uh}{\nu} \quad (4.6)$$

where U is the velocity of the liner (in a reference frame moving with a piston), h is thickness of oil film scraped by an OCR, and ν is kinematic viscosity of oil. If $Re \ll 1$, inertial force is much smaller than viscous force in the corner. Thus, almost all kinetic energy will be dissipated in the corner. On the other hand, if $Re \gg 1$, hardly any kinetic energy is dissipated in the corner. Thus, $Re \sim 1$ can be taken as a critical condition.

In a case when oil is uniformly scraped during an upstroke, U can be taken as the average velocity of the liner. That is:

$$U \sim 2SN \quad (4.7)$$

where S is stroke, N is engine speed. The critical condition $Re \sim 1$ gives that:

$$V_{scraped,c} \sim hS \sim \frac{\nu}{2N} \quad (4.8)$$

where $V_{scraped,c}$ is the critical quantity of scraped oil. It is evaluated in the volume per unit length in the circumferential direction. Equation (4.8) indicates that $V_{scraped,c}$ decreases with engine speed. If the quantity of scraped oil in one single upstroke is much less than this critical value, most kinetic energy will be dissipated in the corner. If the quantity of scraped oil is much greater than the critical value, most kinetic energy is retained by the scraped oil.

If $\nu = 3.125 \times 10^{-6} \text{ m}^2/\text{s}$, which is the value used in the simulations, $V_{scraped,c}$ is roughly $1 \times 10^5 \mu\text{m}^2$ at 800rpm, and $2 \times 10^4 \mu\text{m}^2$ at 4500rpm. Both values are much larger than the largest quantity attempted in the simulations, $10000 \mu\text{m}^2$. Thus, most kinetic energy of scraped oil will be dissipated in the corner.

4.4.2 TDC Scraping: Viscous Dissipation on OCR Flank

Equation (4.8) is also applicable to TDC bridging. However, due to the decreased scraping time, N effectively increases. If scraping occurs from 10° crank angle BTDC, N should effectively increase for 18 times. In this case, $V_{scraped,c}$ at a high engine speed is

less than $1500\mu\text{m}^2$, which is the quantity attempted in simulations of TDC scraping. Thus, the energy budget on an OCR flank needs to be analyzed.

For simplicity, only a non-tapered OCR flank will be analyzed. In an extreme case when little kinetic energy is dissipated in the corner, the spreading distance can be estimated with:

$$s \sim U \cdot \frac{h^2}{\nu} \quad (4.9)$$

where s is spreading distance, h is thickness of oil film scraped by the OCR, and ν is kinematic viscosity of oil. By replacing s with the piston-liner clearance d , a critical quantity of scraped oil can be obtained:

$$V_{\text{scraped},c} \sim hD \sim D \sqrt{\frac{d\nu}{U}} \quad (4.10)$$

where $V_{\text{scraped},c}$ is the critical quantity of scraped oil, and D is the distance that a piston travels during scraping. If $\nu = 3.125 \times 10^{-6} \text{ m}^2/\text{s}$, $d = 0.5\text{mm}$, and scraping occurs from -10° crank angle, $V_{\text{scraped},c}$ is roughly $4 \times 10^4 \mu\text{m}^2$ at 800rpm, and $2 \times 10^4 \mu\text{m}^2$ at 4500rpm. Both values are much greater than $1500\mu\text{m}^2$. Actually, the critical quantity should be even larger because viscous dissipation in the corner has been neglected. Thus, even if oil bears a remarkable amount of kinetic energy after exiting the corner, most kinetic energy will be dissipated on the OCR flank.

4.4.3 Profile of Oil-Gas Interface

Given that most kinetic energy of scraped oil is dissipated, the velocity of accumulated oil is small. Thus, the spreading process is primarily governed by the balance between surface tension and body force. The profile of an oil-gas interface can be analyzed by equating hydrostatic pressure to Laplace pressure, which is exactly the same method as was presented in Chapter 2 and 3. For coherence, details are not presented here. It can be shown that the horizontal span of accumulated oil will not exceed 0.5mm. Thus, the contact line on a non-tapered upper OCR flank cannot spread to the piston land.

The maximum quantity of oil that can reside on an upper OCR flank under an upward body force can also be estimated with the method presented in Chapter 2 and 3. By applying zero contact angles, it can be shown that:

$$V_{\text{max}} \sim 5.13 \frac{\sigma}{\rho a} \quad (4.11)$$

where V_{max} is the maximum quantity of oil that can reside, σ is surface tension, ρ is oil density, and a is the maximum upward body acceleration. If the actual quantity of oil that resides on an OCR flank exceeds the maximum value, oil can break-up into droplets. Otherwise, droplet will not be generated. At 800rpm, V_{max} is roughly $3 \times 10^5 \mu\text{m}^2$; at 4500rpm, V_{max} is roughly $1 \times 10^4 \mu\text{m}^2$. Both values are no less than $10000\mu\text{m}^2$. Thus, it is reasonable that the oil-gas interface will not break-up into droplets.

Up to this point, it has been justified that scraped oil does not reach the piston land or break-up into droplets in the simulations.

4.5 Summary

In this section, the phenomenon of reverse bridging has been studied. Because it potentially increases oil consumption, it is desirable to avoid it in engine operations.

Both simulations and scaling analysis have indicated that oil scraped by an upper OCR flank during an upstroke will either reverse to a liner or reside on the OCR flank, given that the quantity of scraped oil is within a typical range. Thus, the fraction of reverse bridging typically depends on the ratio between these two parts of oil. A small fraction of reverse bridging is desirable.

Simulations indicate that the fraction of reverse bridging decreases with engine speed. This coincides with the observations in experiments. It has been found that the fraction of reverse bridging primarily depends on the recovery of oil-gas interface near TDC. At a low engine speed, oil owns more time to recover to a quasi-static state, and therefore the fraction of reverse bridging is larger.

When the scraped oil comes from the oil film on a liner and is scraped all through an up-stroke, the fraction of reverse bridging is practically 0 at above 3500rpm. Thus, reverse bridging is an issue only in a middle and low speed range.

When the scraped oil comes from bridging oil before TDC, the fraction of reverse bridging is close to 1 at all engine speeds. This is because scraped oil does not own sufficient time to spread away from the liner. This constitutes another reason why bridging is an undesirable phenomenon.

Generally speaking, a tapered chamfer on an upper OCR flank favors reverse bridging. The wedge near the corner formed by an OCR chamfer and a liner encloses more oil near TDC and more oil will be dragged by the liner.

In this work, all simulations started with a dry upper OCR flank. This is not the case in real engine operations. The residual oil in previous revolutions will wet the upper OCR flank. The manner in which scraped oil merges with residual oil is a suggested topic for future research. The variation of fraction of reverse bridging in subsequent revolutions and its asymptotic value can be of particular interest for engine designers.

Furthermore, the clearance between an upper OCR land and a liner may significantly affect the oil flow in the vicinity of the corner. The physics behind the oil flow may substantially alter when the thickness of oil film is much larger than the thickness of scraped oil. This is also a suggested topic for future research.

5 Conclusion

In this work, oil transport from a piston land to a liner in internal combustion engines has been studied. Such an oil transport supplies additional oil to a liner, which means that an OCR partially loses control of oil thickness on the liner. If it occurs near TDC, the additional oil supplied to the liner can become a potential source of oil consumption. One evidence has been presented in [4]. In order to seek for approaches to avoiding such oil transport, a physical understanding of the mechanisms is of significant interest. Three mechanisms have been studied in this work: assisted bridging, self-sustained bridging, and reverse bridging.

Chapter 2 of this report was focused on assisted bridging in a rectangular cavity near a piston third land. It results from axial oil flow under the body force field. Compared to previous studies [2], [6], [7], surface tension was explicitly incorporated into this study, which facilitated an understanding on a few more phenomena during the oil re-distribution process. It was found that the effects of surface tension are more pronounced at lower engine speeds. However, it does not alter the general trend that assisted bridging is more probable at a higher engine speed and with a smaller oil viscosity. Unfortunately, a quantitative correlation incorporating surface tension is still missing. It has been explained that the challenge lies in the modeling of the initialization of a thin film flow. This is a suggested topic for future research.

In Chapter 3, a newly-discovered oil transport mechanism, self-sustained bridging, was introduced. It refers to a phenomenon that oil trapped in a Napier ring hook bridges to a liner. A prerequisite of self-sustained bridging is oil trapping in a Napier ring hook. Both self-sustained bridging and oil trapping potentially increase oil consumption. It has been shown that oil trapping primarily results from surface tension, which is a factor that was commonly neglected in previous studies [2], [4], [7], [11]. An effective approach to eliminating self-sustained bridging is to avoid oil trapping, and one approach to avoiding oil trapping is to optimize the geometric design of a second ring hook and a piston chamfer. Design guidelines have been provided based on the results of a theoretical model. Within a traditional design, two effective methods are 1) to enlarge the height of a hook and a chamfer; 2) to increase the tapered angle of a Napier ring hook. The study on oil trapping and self-sustained bridging enriches the understanding on TDC bridging and possibly addresses the rising concern on oil consumption at low engine speeds. However, the source of trapped oil and circumferential variation remains to be studied in the future.

In Chapter 4, reverse bridging was studied. It refers to a process that oil scraped by an upper OCR flank during an upstroke returns to a liner after TDC. It can be detrimental for the same reason as that for TDC bridging. Simulations indicate that reverse bridging has more detrimental effects at lower engine speeds. If one considers mere reverse bridging, a tapered chamfer on an upper OCR flank is generally harmful. The study on reverse bridging potentially contributes to a better understanding on oil consumption at low engine speeds. However, the occurrence of reverse bridging in successive engine revolutions remains to be studied in future research.

An enriched understanding on oil transport from a piston land to a liner has been obtained in this work. It provides with more fundamental information for engine designers. Furthermore, this work potentially contributes to providing better boundary conditions for friction models and ring models. Examples of friction models can be found

in [17]–[19], in which an oil film on a liner scraped by piston rings is analyzed. An example of ring model can be found in [20], in which the oil transport in the vicinity of an OCR is analyzed.

Besides the future work suggested in each major chapter, oil leakage through a clearance between a ring flank and a ring groove remains to be studied. The clearance between a ring land and a liner also needs to be considered. When the effects of these clearances are incorporated, an extension of this work can possibly be combined with ring models, for instance, [20]. Furthermore, this two-dimensional study remains to be extended to a three-dimensional study in order to incorporate the effects of ring gaps and blow-by gas flows.

Appendix

Appendix 1: Numerical Scheme for Equation (2.49)

Not all values of η_m give a physically valid solution for β_e . It is only meaningful to solve Equation (2.51) in the range of η_m where a valid β_e exists. This section explains how this range is found.

Denote

$$I_1 = \int_0^{\beta_e} \frac{G}{\sqrt{1-G^2}} d\beta \quad (\text{A.1})$$

Then:

$$\frac{dI_1}{d\beta_e} = \frac{G}{\sqrt{1-G^2}} \Big|_{\beta_e} = h_y(y = y_e) < 0 \quad (\text{A.2})$$

That is, I_1 decreases with β_e . Note that:

$$\frac{h_y}{(1+h_y^2)^{\frac{1}{2}}} \in (-1,1) \quad (\text{A.3})$$

Thus:

$$G(\beta) = -\beta^2 + \frac{1}{\sqrt{4\eta_m + 1}} > -1 \quad (\text{A.4})$$

for all β . Hence:

$$\beta_e < \beta_{\max} = \sqrt{1 + \frac{1}{\sqrt{4\eta_m + 1}}} \quad (\text{A.5})$$

Since I_1 decreases with β_e , if Equation (2.49) has a solution, there must be:

$$I_2(\eta_m) = \alpha\sqrt{\eta_m} + \int_0^{\beta_{\max}} \frac{G}{\sqrt{1-G^2}} d\beta < 0 \quad (\text{A.6})$$

where η_m is positive. It can be shown that:

$$I_2(\eta_m = 0) \rightarrow +\infty \quad (\text{A.7})$$

$$I_2(\eta_m \rightarrow +\infty) \rightarrow +\infty \quad (\text{A.8})$$

Thus, the figure of I_2 is expected to resemble Figure A.1 (a), which is evidenced by the numerical result shown in Figure A.1 (b) and (c). If there exists a range of positive η in which (A.6) is satisfied, the minimum value of I_2 ($\eta > 0$) must be negative. This is first checked in the numerical scheme. If it is true, the boundary values, η_{\min} and η_{\max} (See Figure A.1 (a)), are solved for. Then, Equation (2.51) is solved in $[\eta_{\min}, \eta_{\max}]$ only. If the

minimum of I_2 is positive, Equation (2.51) does not have a solution, which is always the case at the first few time steps.

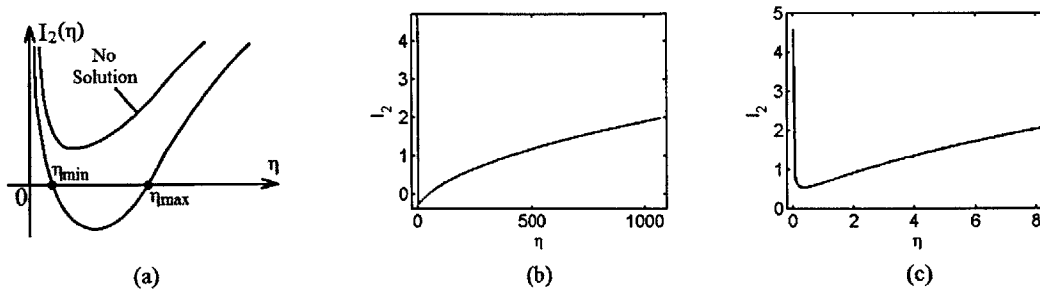


Figure A.1 Figure of $I_2(\eta)$. (a): schematic diagram; (b) & (c): examples of computed results

References

- [1] K. Holmberg, P. Andersson, and A. Erdemir, "Global energy consumption due to friction in passenger cars," *Tribol. Int.*, vol. 47, no. 0, pp. 221–234, Mar. 2012.
- [2] B. Thirouard and T. Tian, "Oil transport in the piston ring pack (Part I): identification and characterization of the main oil transport routes and mechanisms," SAE International, Warrendale, PA, 2003-01-1952, May 2003.
- [3] B. Thirouard and T. Tian, "Oil transport in the piston ring pack (Part II): zone analysis and macro oil transport model," SAE International, Warrendale, PA, 2003-01-1953, May 2003.
- [4] S. Przesmitzki, A. Vokac, and T. Tian, "An experimental study of oil transport between the piston ring pack and cylinder liner," SAE International, Warrendale, PA, 2005-01-3823, Oct. 2005.
- [5] A. Vokac and T. Tian, "An experimental study of oil transport on the piston third land and the effects of piston and ring designs," SAE International, Warrendale, PA, 2004-01-1934, Jun. 2004.
- [6] Y. Wang, "Air flow effects in the piston ring pack and their implications on oil transport," Thesis, Massachusetts Institute of Technology, 2012.
- [7] B. P. Thirouard, "Characterization and modeling of the fundamental aspects of oil transport in the piston ring pack of internal combustion engines," Thesis, Massachusetts Institute of Technology, 2001.
- [8] E. B. Senzer, "Oil transport inside the oil control ring groove and its interaction with surrounding areas in internal combustion engines," Thesis, Massachusetts Institute of Technology, 2012.
- [9] S. Przesmitzki and T. Tian, "Oil transport inside the power cylinder during transient load changes," SAE International, Warrendale, PA, 2007-01-1054, Apr. 2007.
- [10] Eric James Zanghi, "Analysis of Oil Flow Mechanisms in Internal Combustion Engines via High Speed Laser Induced Fluorescence (LIF) Spectroscopy," Thesis, Massachusetts Institute of Technology, Cambridge, MA, 2014.
- [11] A. Vokac, "An experimental study of the oil evolution in critical piston ring pack regions and the effects of piston and ring designs in an internal combustion engine utilizing two-dimensional laser induced fluorescence and the impact on maritime economics," Thesis, Massachusetts Institute of Technology, 2004.
- [12] S. McGrogan, "Modeling and simulation of oil transport for studying piston deposit formation in IC engines," Thesis, Massachusetts Institute of Technology, 2007.
- [13] T. Tian, "Oil Transport and Oil Consumption, Connecting Different Scales," presented at the Lubrication in Internal Combustion Engines Consortium, Sloan Automotive Laboratory, Cambridge, MA, 09-Mar-2011.
- [14] É. Lorenceau, D. Quéré, and J. Eggers, "Air entrainment by a viscous jet plunging into a bath," *Phys. Rev. Lett.*, vol. 93, no. 25, 2004.
- [15] J. Eggers, "Air entrainment through free-surface cusps," *Phys. Rev. Lett.*, vol. 86, no. 19, pp. 4290–4293, 2001.
- [16] H. K. Moffatt, "Viscous and resistive eddies near sharp corner," *J. Fluid Mech.*, vol. 18, no. 1, pp. 1–18, 1964.

- [17] Y. Liu, "Developing an approach utilizing local deterministic analysis to predict the cycle friction of the piston ring-pack in internal combustion engines," Thesis, Massachusetts Institute of Technology, 2013.
- [18] H. Chen, "Modeling the lubrication of the piston ring pack in internal combustion engines using the deterministic method," Thesis, Massachusetts Institute of Technology, 2011.
- [19] T. Tian, "Modeling the performance of the piston ring-pack in internal combustion engines," Thesis, Massachusetts Institute of Technology, 1997.
- [20] C. Baelden, "A Multi-Scale Model for Piston Ring Dynamics, Lubrication and Oil Transport in Internal Combustion Engines," Massachusetts Institute of Technology, Cambridge, MA, 2014.